DE GRUYTER

Vladimir M. Fomin

SELF-ROLLED MICRO- AND NANOARCHITECTURES

TOPOLOGICAL AND GEOMETRICAL EFFECTS

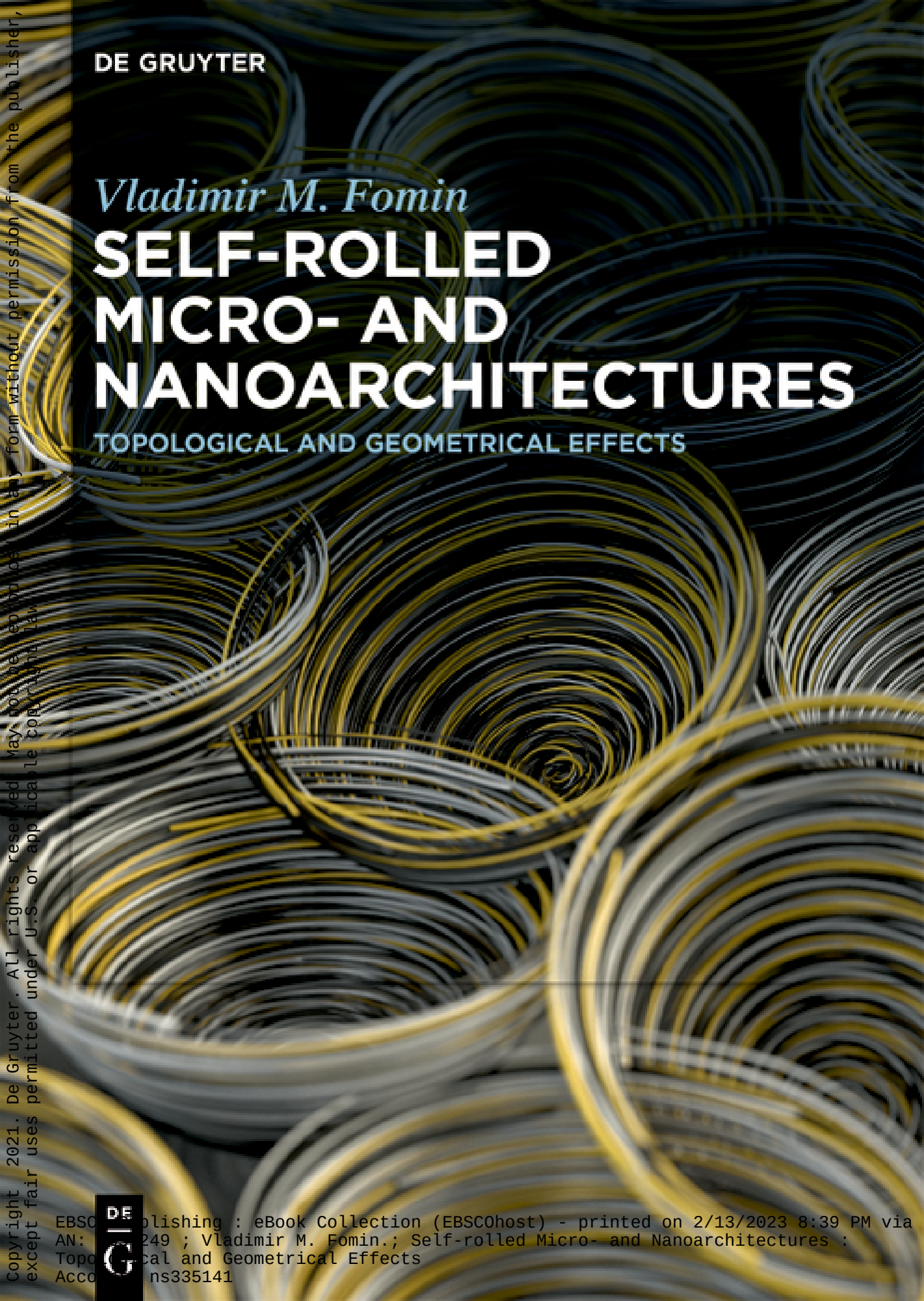

Vladimir M. Fomin

Self-rolled Micro- and Nanoarchitectures

Also of interest

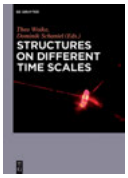

Structures on Different Time Scales
Woike, Schaniel, 2018
ISBN 978-3-11-044209-0, e-ISBN 978-3-11-043392-0

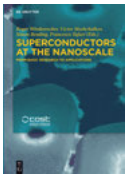

Superconductors at the Nanoscale.
From Basic Research to Applications
Wördenweber, Moshchalkov, Bending, Tafuri (Eds.), 2017
ISBN 978-3-11-045620-2, e-ISBN 978-3-11-045680-6

Nanoscience and Nanotechnology.
Advances and Developments in Nano-sized Materials
Van de Voorde (Ed.), 2018
ISBN 978-3-11-054720-7, e-ISBN 978-3-11-054722-1

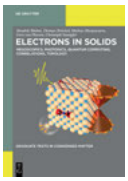

Electrons in Solids.
Mesoscopics, Photonics, Quantum Computing, Correlations, Topology
Bluhm, Brückel, Morgenstern, von Plessen, Stampfer, 2019
ISBN 978-3-11-043831-4, e-ISBN 978-3-11-043832-1

Vladimir M. Fomin

Self-rolled Micro- and Nanoarchitectures

Topological and Geometrical Effects

DE GRUYTER

Author
Prof. Dr. Vladimir M. Fomin
Leibniz Institute for Solid State
and Materials Research (IFW)
Institute for Integrative
Nanosciences (IIN)
Helmholtzstr. 20
01069 Dresden
v.fomin@ifw-dresden.de

ISBN 978-3-11-057410-4
e-ISBN (PDF) 978-3-11-057557-6
e-ISBN (EPUB) 978-3-11-057423-4

Library of Congress Control Number: 2020943487

Bibliographic information published by the Deutsche Nationalbibliothek
The Deutsche Nationalbibliothek lists this publication in the Deutsche Nationalbibliografie; detailed bibliographic data are available on the Internet at http://dnb.dnb.de.

Coverabbiildung: e_zebolov/iStock/Getty Images
Typesetting: Integra Software Services Pvt. Ltd.
Printing and binding: CPI books GmbH, Leck

www.degruyter.com

To Evguenia

Preface

They will be rolled up like a cloth, even like a robe, and they will be changed . . .
Hebrews 1:12 (https://bible.knowing-jesus.com/Hebrews/1/12)

Advances of high-tech nanostructure fabrication techniques have allowed for generating geometrically and topologically nontrivial manifolds at the nanoscale with man-made space metrics, which determine electronic, optical, magnetic and transport properties of such objects and novel potentialities of nanodevices due to their unique topology. Analysis of topologically nontrivial manifolds at the nanoscale is of immense importance for semiconductor, superconductor and graphene physics as well as for electronics, magnetism, optics, optoelectronics, thermoelectrics and quantum computing [Fomin18a, Fomin18b].

This book provides an in-depth representation of the advanced theoretical and numerical models developed to analyze key topological and geometrical effects, which underlie engineering of transport, superconducting and optical properties of state-of-the-art self-rolled micro- and nanoarchitectures. Within a holistic approach, the effects of rolling up are analyzed theoretically for superconductor (Chapter 2), semiconductor (Chapter 3) and magnetized micro- and nanoarchitectures (Chapter 4), catalytic tubular micromotors (Chapter 5) and optical microcavities (Chapter 6). It is intended for basic research in nanosciences and nanotechnologies, development of strategies for industrial applications of self-rolled micro- and nanoarchitectures as well as for advanced education of interdisciplinary specialists, PhD students and students.

I am deeply grateful to Oliver G. Schmidt, in close motivating collaboration with whom I have been performing investigations in the multifaceted field of physics of self-rolled micro- and nanoarchitectures at the Institute for Integrative Nanosciences – Leibniz Institute for Solid State and Materials Research Dresden over more than a decade. I thank my colleagues and friends for fruitful collaborations: Adithya N. Ananth, Alexander A. Balandin, Stefan Baunack, Mária Bendová, Carlos C. Bof Bufon, Stefan Böttner, Vladimir Ciobanu, Alexandr I. Cocemasov, Rosa Córdoba, José María De Teresa, Mihail Enachi, Thomas Gemming, Sandeep Gorantla, Daniel Grimm, Isabel Guillamón, Jörg B. Götte, Maria Guix, Martina Hentschel, Markus Hippler, Calina I. Isacova, Suwit Kiravittaya, Matthew R. Jorgensen, Dmitrii D. Karnaushenko, Islam S. M. Khalil, Anke Klingner, Evgenii A. Levchenko, Guodong Li, Shilong Li, Gungun Lin, Libo Ma, Veronika Magdanz, Dominique Mailly, Denys Makarov, Anastassios Mavrokefalos, Mariana Medina-Sánchez, Sarthak Misra, Denis L. Nika, Gian Paolio Papari, Evgeny A. Posenitskiy, Vitalie Postolache, Armando Rastelli, Roman O. Rezaev, Mark H. Rümmeli, Samuel Sanchez, Shivkant Singh, Elliot J. Smith, Ekaterina I. Smirnova, Lluís Soler, Hermann Suderow, Ion Tiginyanu, Marlitt Viehrig, Roger Wördenweber, Yin Yin, Milad Yarali, Uli Zeitler and Feng Zhu.

I am extremely grateful to many colleagues for insightful discussions: Artur S. Ascherov, Alexey Bezryadin, Vladimir A. Bolaños Quiñones, Igor A. Bogush, Danilo

https://doi.org/10.1515/9783110575576-202

Bürger, Peter Cendula, Christoph Deneke, Fei Ding, Oleksandr A. Dobrovolskiy, Renat R. Dusaev, Rudolf P. Huebener, Fariborz Kargar, Daniil D. Karnaushenko, Feodor V. Kusmartsev, José Lorenzana, Sören Lösch, Karthikeyan Manga Loganathan, Michael Melzer, Yongfeng Mei, Dimitri Roditchev, José G. Rodrigo Rodriguez, Ivan A. Sadovskyy, Valerij A. Shklovskij, Anatolie S. Sidorenko, Alexander A. Solovev, Francesco Tafuri, Arturo Tagliacozzo, Dominic J. Thurmer, Reinhard Tidecks, Sreeramulu Valligatla, Jeroen van den Brink, Sebastián Vieira, Valerii M. Vinokour, Jiawei Wang, Andrei D. Zaikin and Eli Zeldov. I am thankful to ZIH TU Dresden for providing the supercomputer Taurus for high-throughput numerical calculations.

I would like to thank Vivien Schubert, Senior Editor, Kristin Berber-Nerlinger, Acquisitions Editor, and David Jüngst, Project Manager, for a vigorous support of the publication of the book.

With profound gratitude I keep the memory of my parents and Professor Evghenii P. Pokatilov, who nurtured my aspiration for scientific research. Cordial thanks are due to my wife and children for their understanding, patience and support in the course of my work on this book.

Dresden — Vladimir M. Fomin

Contents

1 Introduction

Topology is the branch of mathematics dealing with the properties of objects that are preserved under continuous deformations, while geometry is concerned with shape, size and relative position of objects in space [Eschrig11]. A topological analysis reveals universal properties of an object, which are detached from geometrical magnitudes like length, volume or radius of curvature but are preserved upon continuous deformations, such as stretching, crumpling and bending (not tearing or gluing). These properties lead to topological invariants, shared, for instance, by a circle and a triangle in two dimensions (2D) or a doughnut and a coffee cup in three dimensions (3D). Physicists were not considering the topology of the real world until relatively recently, as long as the topological features were detached from the classical attributes of a typical measurement (i.e., object's length or size). Yet, solving the puzzling mysteries of the quantum Hall effect changed this forever. In the 1980s, explaining the plateaus of the Hall resistance in an external magnetic field [Klitzing80] revealed, for the first time, that topology could be a background for development of cardinally new physical effects and novel materials and devices based thereon. This new degree of freedom had never been exploited before, not even theoretically, but today, we already know that 30% of all crystal matter (upon analysis of their spatial symmetry group) might hide a topological property, waiting for an application [Castelvecchi17].

This all-new concept soon rose above its condensed-matter origin and, nowadays, topological nanophotonics and metamaterials are at the heart of several groundbreaking technologies. Not surprisingly, with all this excitement, the Nobel Prize 2016 was awarded to the discoverers of the topological phase [Nobel16]. Up to now, topological insulators have been identified only in the bulk and in 2D systems and nanostructures of simple geometry, like lithographic quantum dots. This, however, contrasts with photonics, where fabrication of light scatterers one by one allows for creating unprecedented photonic structures, which combine chiral-edge states with the geometrical properties of the surface defined by the scatterers. Translating such concepts to electronic states is an exciting challenge at multiple levels. Not only is it more difficult to fabricate architectures that implement tailoring of topologic order of electronic states due to complex geometric confinement, but also their characterization and modeling require cardinally novel insights. Implementing these novel and robust topology- and geometry-controlled quantum properties to circumvent present limitations is the top priority in today's materials science, microelectronics, spintronics and biomedicine.

The study of topological matter is one of the fascinating main roads of modern physics. Topology-driven concepts, like the geometric phase, the Aharonov–Bohm effect, topologic phases and phase transitions, topological origin of the quantum Hall effect, topological insulators, topological semimetals, topological superconductors

https://doi.org/10.1515/9783110575576-001

and Majorana fermions, have revolutionized condensed matter physics. The realm of topological matter can be conventionally subdivided into two categories. First, nontrivial topology occurs due to a special geometry of structures or fields in real space, for example, quantum rings [Fomin18a], Möbius rings [Fomin12b], metamaterials of interlocked hollow semiconducting tori [Kern17], optical waveguides [Ma16a], multiterminal Josephson junctions [Riwar16], Skyrmions [Romming13] and other topological spin and magnetic textures [Pylypovski15, Streubel16]. Second, topologically protected surface/edge states governed by Dirac physics and/or topologically nontrivial electronic structure in the momentum space underlie quantum Hall effect [Klitzing80, Thouless82], quantum spin Hall effect [König07], quantum anomalous Hall effect [Chang13], topological insulators [Xu14], topological superconductors [Beenakker16], Weyl fermion semimetals [Xu15], topological photonic crystals [Lu16] and topological acoustic metamaterials [Süsstrunk15].

A powerful high-tech method of self-assembly of micro- and nanoarchitectures was designed on the base of the strain-driven roll-up procedure [Prinz00, Schmidt01a]. It paved the way for novel classes of self-rolled[1] metamaterials: single semiconductor and superconductor micro- and nanotubes (or radial crystals) [Krause06, Thurmer08, Thurmer10] and multilayer spiral micro- and nanotubes (or radial superlattices) [Deneke04]. A comprehensive structural study was provided for semiconductor/oxide and semiconductor/organic, as well as for semiconductor/metal hybrid radial superlattices [Deneke09].

The emerging nanostructures lead to the occurrence of novel, counterintuitive materials properties and thereby promise a significant improvement of the figures of merit as compared to the available devices (see, e.g., [Li17, Lösch19]). Micro- and nanorobots are of great significance and highly desirable in various directions of nanomedicine from noninvasive therapy of deep tissues and treating diseases at the cellular level to drug delivery and biosensing. However, precise motion control and functional medical tasks demand onboard electronics for signal analysis, autonomous diagnosis and wireless communication, and integrating such capabilities is a challenging issue [Medina17]. An autonomous microrobotic system is demonstrated by using shapeable polymeric nanomembranes as a platform to integrate two self-rolled microtubular catalytic micromotors. A square coil integrated into the platform enables wireless energy transfer through inductive coupling providing local heating of the catalytic engines and thus enabling an effective directional control of motion [Bandari20]. This approach opens the door to a new generation of micro-/nanoarchitectures with integration of multifunctional components, such as circuits, electronic and optoelectronic devices, actuators, wireless power supply and communication.

1 The term “self-rolled” [Merriam-Webster20] meaning “rolled or coiled upon itself” is used in this book synonymous to “rolled-up” in relation to micro- and nanoarchitectures, which are fabricated by the strain-driven self-assembly.

Self-rolling of planar multilayer nanomembranes into 3D microarchitectures offers a variety of opportunities to accommodate thin-film microelectronic functionalities in smaller and lighter devices possessing improved performance, reduced costs and higher integration density for future micro- and nanoelectronics [Bandari20]. For instance, self-rolled hybrid organic/inorganic heterostructures consisting of metallic nanomembranes and self-assembled layers of colloidal nanoparticles provide efficient building blocks with desired electronic behavior for nanoelectronic devices [Bendova16].

The present monograph provides an overview of the effects driven by complex geometries and nontrivial topologies, which are implemented by the roll-up fabrication of micro- and nanoarchitectures. Insight in the electronic, transport, optical and magnetic features of such man-made topological manifolds at micro- and nanoscale is of immense importance for both fundamental semiconductor, superconductor and graphene physics as well as optics and tomorrow's micro- and nanoelectronics, robotics, thermoelectrics, biomedicine and quantum computing.

2 Vortex matter in self-rolled superconductor micro- and nanostructures

The key pathways in fabrication of complex superconductor 3D nanoarchitectures (e.g., open nanotubes and nanohelices) is based on the advanced 3D roll-up self-organization [Lösch19] and nanowriting techniques using focused electron-beam-induced [Huth18] or focused ion-beam (FIB)-induced deposition [Cordoba19].

Combination of reduced dimensionality with curved geometry of superconductor micro- and nanostructures produced by the advanced roll-up technology is a rich source of novel dynamics. These dynamics are described by two characteristic times: the period of nucleation of vortices at one edge of the structure and the duration of motion of a vortex along the structure. Numerical modeling within the time-dependent Ginzburg–Landau (TDGL) approach shows that the curved geometry governs the dynamics of vortices in the presence of transport currents in open superconductor micro- and nanotubes subject to a magnetic field orthogonal to the axis [Fomin12a] (see Section 2.1). Synergetic effects of shape and dimensions on both equilibrium and dynamical vortex distributions cause drastic changes of vortex patterns, which lead to a nonmonotonic dependence of characteristic times on the magnetic field. Being of the order of several microvolts by magnitude, the voltage induced by the moving vortices in open tubes at the micrometer scale can be detectable by modern equipment. The detection of the open-tube geometry effects on vortex dynamics remains feasible in the presence of pinning centers [Rezaev14]. Open microtubes can serve as tunable superconducting fluxon generators for fluxon-based information technologies.

Numerical modeling of vortex dynamics is performed for finite-thickness open microtubes. An increase of thickness enhances the vortex–vortex interaction, which results in a reduced number of vortices in an equilibrium configuration and causes a new regime of vortex dynamics. At a certain value of the magnetic field, which depends on the geometry of the tube, collective phenomena lead to the bifurcation of vortex trajectories [Rezaev15] (see Section 2.2). Using inhomogeneous transport current in the microtube with multiple electrodes allows for vortex removal from certain regions of a superconductor sample, which is of practical interest, for example, in order to suppress the $1/f$ noise due to the activated hopping of trapped vortices and thus to extend the operation regime of superconductor-based sensors to lower frequencies [Rezaev16].

Strain-driven self-assembly of rolled-up architectures on the nano- and microscale allows for fabrication of Swiss-roll-shaped micro- and nanotubes with superconductor layers (e.g., InGaAs/GaAs/Nb). Those hybrid structures open hitherto unprecedented possibilities for experimental investigation of vortex matter in superconductors with curved geometries. In the self-rolled structures, the quasi-two-dimensionality of the

https://doi.org/10.1515/9783110575576-002

superconductor layer is combined with a curvature. A theoretical investigation of the superconducting state in the helical coils at the micro- and nanoscale is performed within the TDGL approach [Fomin17] (see Section 2.4). The pattern and number of vortices in a stationary distribution are determined by their confinement to the ultrathin helical coil and can therefore be efficiently controlled by the spiral stripe width and the spiral pitch distance for both dense and sparse coils. Quasidegeneracy of vortex patterns is manifested in the helical coil when the number of vortices is incommensurable with the total number of half-turns. The obtained results demonstrate perspectives of tailoring both equilibrium and nonequilibrium properties of vortices in curved superconductor micro- and nanoarchitectures.

Rolling up superconductor Nb nanomembranes into open tubes allows for a new, highly correlated vortex dynamics regime. The induced voltage as a function of the magnetic field provides information about the vortex pattern. In particular, an increase of the number of vortex chains in the tube results in a sixfold decrease of the slope of the induced voltage as a linear function of the magnetic field [Rezaev19] (see Section 2.3). The topological transition between the vortex-chain and phase-slip regimes [Rezaev20] opens up new perspectives for the advanced technological applications of self-rolled superconductor nanoarchitectures, such as for high-performance detectors and sensors, energy-storage components, quantum computing and microwave radiation detection.

Another approach, which realizes a 3D printing, is represented, as an example, by He^+-FIB direct writing. It allows for fabrication of the small and high-densely packed nanohelices, with dimensions of 100 nm in diameter and aspect ratio of up to 65. Given their helical 3D geometry, fingerprints of vortex and phase-slip patterns are experimentally identified and supported by numerical simulations based on the TDGL equation [Cordoba19] (see Section 2.4).

2.1 Vortex dynamics in open superconductor microtubes

Hybridization of reduced dimensionality in a superconductor with curved geometry and nontrivial topology has been a rich source of novel physics. For instance, measurements of the magnetoresistance in superconductor cylinders [Little62] and loops [Moshchalkov95] revealed fluxoid quantization and a huge impact of nanostructuring on the normal–superconducting phase boundary. Curvature was found to be the key factor to control the depression of the critical temperature in a thin superconductor cylindrical shell as a function of the angle between the axis of the cylinder and the magnetic field [Tinkham63, Meservey72]. The coexistence of the Meissner state with various vortex patterns in thin superconductor spherical shells [Gladilin08] was shown to drive the phase transition to higher magnetic fields [Tempere09]. The multiple periodicity of magnetoresistance observed in $YBa_2Cu_3O_{6+x}$ (YBCO) nanoscale rings [Carillo10] implied the existence of a concentric vortex structure with nonuniform

vorticity [Zhao03]. In high-temperature superconductor films patterned into a network of nanoloops, interplay in the interaction between thermally excited moving vortices and the oscillating persistent current induced in the nanoloops gave rise to the observed large oscillations of the magnetoresistance [Sochnikov10].

In the present section, inspired by the advancements in fabrication of self-rolled micro- and nanotubes [Schmidt01b] including superconductor layers (e.g., InGaAs/GaAs/Nb) [Thurmer08, Thurmer10], effects of curvature on the dynamics of vortices are investigated in open superconductor tubes, which are placed in a magnetic field perpendicular to the axis [Fomin12a]. Such a configuration is interesting because the *normal* to the surface component of the magnetic field is *strongly* inhomogeneous.

A membrane of Nb is considered, which is self-rolled into an open cylindrical tube of radius R and length L with its axis parallel to the x-axis (Fig. 1.1a). The key characteristics of a superconducting state, coherence length ξ and penetration depth λ for a Nb membrane [eqs. (4.24b) and (4.26b) of [Tinkham96]] are determined by the parameters: $\xi_0 = 38$ nm, $\lambda_L(0) = 39$ nm [Maxfield65] and the mean free electron path [Lemberger07] $l = 10\text{nm}/(1 + 40\text{nm}/d)$, which equals to 5.6 nm for the thickness of membrane $d = 50$ nm. At the relative temperature $T/T_c = 0.95$, the resulting values are $\lambda = 279$ nm and $\xi = 56$ nm. The Ginzburg–Landau parameter is $\kappa = \lambda/\xi = 5$. With the Fermi velocity $v_F = 6 \times 10^5$ m/s [Lemberger07], the diffusion coefficient is $D = lv_F/3 = 11.2 \times 10^{-4}$ m^2/s. A narrow paraxial slit is present throughout the whole cylinder: in other words, an *open* cylinder is considered. The applied uniform magnetic field is parallel to the z-axis: $\mathbf{B} = B\mathbf{e}_z$.

Taking into account a complex boundary of the structures under analysis in this book, we select a phenomenological description of superconductivity in the presence of a magnetic field, provided by the TDGL equation [Schmid66] for the complex-valued function, which is called superconducting order parameter $\psi(\mathbf{r}, t)$ ([Ketterson99], section 21):

$$\frac{\hbar^2}{2m^* D}\frac{\partial \psi}{\partial t} - \frac{\hbar^2}{2m^*}\left(\nabla + \frac{2e}{\hbar} i\mathbf{A}\right)^2 \psi + \alpha\psi + \beta|\psi|^2\psi = 0, \tag{2.1}$$

where m^* is the mass and $-2e$ is the charge of a particle, which carries a superconducting current, $\hbar$ is the reduced Planck's constant, D is the diffusion coefficient, e is the elementary electron charge, ∇ is the nabla operator, $\mathbf{A}$ is the vector potential of the magnetic field and α and β are functions of the temperature T ([Poole95], p. 123):

$$\alpha(T) = \alpha_0\left(\frac{T}{T_c} - 1\right), \ \beta(T) \text{ is a weak function of temperature,} \tag{2.2}$$

where both α_0 and β are positively defined, so that $\alpha(T)$ vanishes at the critical temperature T_c and is negatively determined at $T < T_c$. In this interval of temperatures, the function $\alpha(T)$ is usually expressed in terms of the squared *coherence length* $\xi(T)$:

$$\alpha(T) = -\frac{\hbar^2}{2m^*\xi^2(T)}. \tag{2.3}$$

The *London penetration depth* is defined as [cp. with eq. (9.28b) [Ketterson99]]:

$$\lambda^2 = -\frac{m^*\beta}{4e^2\mu_0\alpha(T)} \equiv \frac{(m^*)^2\beta\xi^2(T)}{2e^2\mu_0\hbar^2}, \tag{2.4}$$

wherefrom the coefficient β in the TDGL equation is represented as

$$\beta = \frac{2e^2\mu_0\hbar^2\lambda^2}{(m^*)^2\xi^2(T)}, \tag{2.5}$$

where μ_0 is the magnetic permeability of free space. For the subsequent numerical treatment, it is convenient to represent the TDGL equation in a dimensionless form [Fomin09]

$$\frac{\partial\psi}{\partial t} = (\nabla - i\mathbf{A})^2\psi + 2\kappa^2\psi\left(1 - |\psi|^2\right). \tag{2.6}$$

The dimensional units for physical quantities involved in the TDGL equation are explicitly indicated in Table 2.1.

Table 2.1: Definition of dimensional units (after [Fomin09, Rezaev14]).

Physical quantity	Unit	Value of the unit
Time	$2\lambda^2/D$	0.14 ns
Length	$\sqrt{2}\lambda$	395 nm
Magnetic field	$\Phi_0/(4\pi\lambda)$	2.12 mT
Magnetic flux	Φ_0	2.0678×10^{-15} Wb [Poole95]
Current density	$\Phi_0 c/(8\sqrt{2}\pi^2\lambda^3)$	8.57×10^9 A/m^2

Because the membrane's thickness d (50 nm) is substantially smaller than the effective penetration depth for the Nb membrane, the 2D approximation is applicable. Its justification has been provided in [Smirnova20]. The magnetic field in the sample is approximated by the applied magnetic field **B**. The effects of the magnetic field renormalization are small for the geometric parameters assumed here [Smirnova20]. According to Fig. 2.1a, the normal to the cylindrical surface component of the magnetic field is strongly inhomogeneous: $B_n(\varphi) = -B\sin(\varphi)$ and an effective magnetic flux is $\Phi = 2RLB$, which can be expressed in units of the magnetic flux quantum $\Phi_0 = h/(2e)$ with the Planck constant $h = 2\pi\hbar$. The vector potential **A** of the magnetic field is taken in the Landau gauge: $\mathbf{A} = A\mathbf{e}_x$, $A = -By$. The boundary conditions at the surfaces of the structure neighboring air

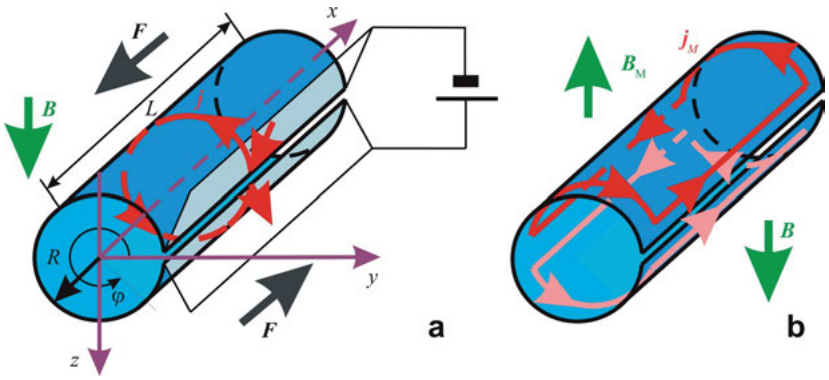

Fig. 2.1: (a) Scheme of the open tube. A transport current is represented with heavy (red) arrows. The electrodes, which are connected to both sides of a slit, are shown semitransparent. The *x*-axis is selected as the polar axis of cylindrical coordinates (ρ, φ, x). The angle φ is counted from the direction of the *y*-axis passing through the middle of the slit. (b) Scheme of Meissner currents in a superconductor tube. Two systems of Meissner currents $\mathbf{j}_M$ develop flowing along the both sides of the cut (represented in red and pink). The magnetic field $\mathbf{B}_M$ induced by Meissner current tends to partly compensate the applied magnetic field **B** (from [Fomin12a]).

$$\left(\nabla - i\mathbf{A}\right)\psi|_{n,\,\text{boundary}} = 0 \tag{2.7a}$$

represent absence of a normal to the surface component of the superconducting current. The modified boundary conditions at the sides of the slit, to which electrodes are attached, establish matching between the transport current density $\mathbf{j}_{tr} = j_{tr}\mathbf{e}_\varphi$ and the normal to the surface component of the superconducting current:

$$\left[\nabla - i\left(\mathbf{A} + \frac{\mathbf{j}_{tr}}{|\psi|^2}\right)\right]\psi|_{n,\,\text{electrtode}} = 0. \tag{2.7b}$$

The calculations are performed within an adaptive finite-difference scheme. It consists of two stages. At the first stage, a stationary distribution of the order parameter is reached in a sample exposed to a given magnetic flux Φ. At the second stage, a transport current $\mathbf{j}_{tr}$ is switched on, and a stationary state of the vortex dynamics is determined [Fomin09].

In equilibrium, fragments of a hexagonal vortex lattice form at the top and bottom areas of the tube, where the magnetic field is normal (at $\varphi = \pi/2, 3\pi/2$) or close to normal to the surface. There are no vortices in the side areas of the tube, where the magnetic field is tangential (at $\varphi = 0,\ \pi$) or close to tangential to the surface. Curvature-induced inhomogeneity of the normal component of the magnetic field

component $B_n(\varphi) = -B\sin(\varphi)$ leads to an inhomogeneous deformation of the hexagonal vortex lattice. An increase of the magnetic flux produces more prominent Meissner currents $\mathbf{j}_M$ as shown in Fig. 2.1b. The existence of supercurrent circulation in a thin-wall cylinder due to a magnetic field component perpendicular to the axis was described in [Tinkham63]. Furthermore, for cylindrical thin-film shells in a tilted magnetic field, a superposition of superconducting vortices and supercurrent circulation was anticipated for large enough magnetic field components normal to the axis [Meservey72]. Our equilibrium patterns of the order parameter clearly reveal a coexistence of superconducting vortices and Meissner currents in tubes. In a superconductor tube of radius $R = 500$ nm (which is of the same order of magnitude as the penetration depth and one order of magnitude larger than the coherence length for the temperature under consideration) at $\Phi/\Phi_0 < 32$, Meissner currents flow in the regions free of vortices. At $\Phi/\Phi_0 = 32$, Meissner currents begin to penetrate the region with vortices. The occurring Magnus force pushes the vortices away from the regions, where the magnetic field is close to tangential. With further increase of the relative magnetic flux ($\Phi/\Phi_0 = 56$ and 60), the sample becomes strongly inhomogeneous: the superconducting state is expelled from the side areas of the tube, while at the top and bottom, the vortices form chains. The number of vortex rows in a chain at $\Phi/\Phi_0 = 56$ decreases from about 3 to 2 with halving the radius from 500 to 250 nm. In tubes, the shape of a vortex configuration is determined by a competition between the triangular vortex lattice and the boundary region on the cylindrical surface, where vortices occur. This boundary region in tubes, as distinct from planar films, is not a geometric boundary, but rather results from an interplay between the magnetic field and the curvature of the cylindrical surface.

Now, we switch on a transport current with density $\mathbf{j}_{tr} = j_{tr}\mathbf{e}_\varphi$, which is imposed through the electrodes attached to both sides of the slit as shown in Fig. 2.1a. Each of the vortices moves under the influence of the Magnus force density [Tinkham96] $\mathbf{F} = \mathbf{j}_{tot} \times \mathbf{B}$ due to the total current $\mathbf{j}_{tot} = \mathbf{j}_{tr} + \mathbf{j}_M + \mathbf{j}_{vortices}$, which includes the transport current $\mathbf{j}_{tr}$, a Meissner current $\mathbf{j}_M$ and a current $\mathbf{j}_{vortices}$ of other vortices (if present).

At low magnetic fields, individual vortices periodically nucleate at edges of the tube (at $x = L$ at around $\varphi = \pi/2$ and $x = 0$ at around $\varphi = 3\pi/2$). Subsequently, they move along the tube under the action of the Magnus force until they denucleate at the opposite edge of the tube (case $\Phi/\Phi_0 = 7.5$ in Fig. 2.2). In higher magnetic fields (cases $\Phi/\Phi_0 = 15.0$ and 22.5 in Fig. 2.2), the equilibrium vortex pattern persists in the presence of a transport current, but is subject to deformations [Fomin12a]. These deformations are more prominent in tubes of larger radius and are visualized by the accumulated vortex trajectories (increments of the local values of the order parameter integrated over time). After a nucleation of a new vortex at one tube edge, its motion governed by the Magnus force leads to a shift of all the other vortices at the sites in a row closest to the slit, toward the opposite edge, until the last vortex of the row denucleates at the latter edge. The accumulated vortex trajectory represents just this passing

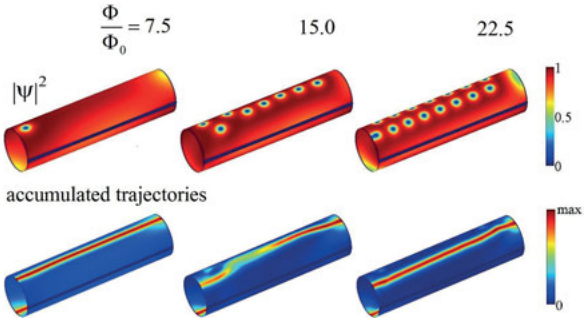

Fig. 2.2: Snapshots of the superconducting order-parameter distribution (first row) and accumulated trajectories (second row) of vortices at $\Phi/\Phi_0 = 7.5,\ 15.0$ and 22.5 in the presence of a transport current with dimensionless density $j_{tr} = 1.65$ (the current density unit is 8.57×10^9 A/m^2) in an open tube of radius $R = 500$ nm and length $L = 3.5$ μm with a slit of width $1/30 \times 2\pi R = 105$ nm (from [Fomin12a]).

of vortices through the sites in the row reminiscent of conduction on a percolating lattice [Kirkpatrick73]. Vortices remote from the slit remain almost immobile, because the transport current is significantly perturbed there by the currents of the vortices, which are closer to the slit.

For a magnetic field, which is lower than a "first critical" value B_{cr}, indicated in Fig. 2.3c, there are no vortices in tubes. At $B \approx B_{cr}$, there appear vortices moving in one and the same direction at the bottom (or top) of a tube. At $B > B_{cr}$, two sets of paths correspond to vortices moving in opposite directions in the top and bottom areas of the tube because they meet opposite transport currents. The opposite directions of the Magnus force at $\varphi = \pi/2$ and $\varphi = 3\pi/2$ are illustrated in Fig. 2.1a. This behavior is peculiar for tubes. With increasing magnetic field beyond a "second critical" value, there are no vortices because of the strong Meissner currents.

In Fig. 2.3a,b, x-coordinates of vortices in tubes with $L = 3.5$ μm, $R = 280$ nm for $\Phi/\Phi_0 = 8.5$ and 11, correspondingly, are shown as a function of time. In the sparse-vortex regime, represented in Fig. 2.3a, the time needed for a vortex to move from one to another edge of the tube Δt_1 is larger than the time between two consecutive vortex nucleation events at one edge of the tube Δt_2. In this regime, a new vortex (at the bottom or at the top part) does not nucleate before an "old" vortex (at the same part) has denucleated, and hence, the time average of the number of vortices at each part of the tube is <1. At a transition magnetic field B_{tr}, indicated in Fig. 2.3c, both characteristic times become equal to each other: $\Delta t_1 = \Delta t_2$. The time average of the number of vortices at each part of the tube is precisely 1. When further increasing the magnetic field $B > B_{tr}$, the multivortex regime occurs, represented in Fig. 2.3b, where $\Delta t_1 < \Delta t_2$. Consequently, a new vortex (in the bottom or top area) nucleates before the previously nucleated (in the same area) vortex has denucleated, and the time average of the number of vortices in each area of the tube is >1. In the interval 200 nm $< R <$ 600 nm,

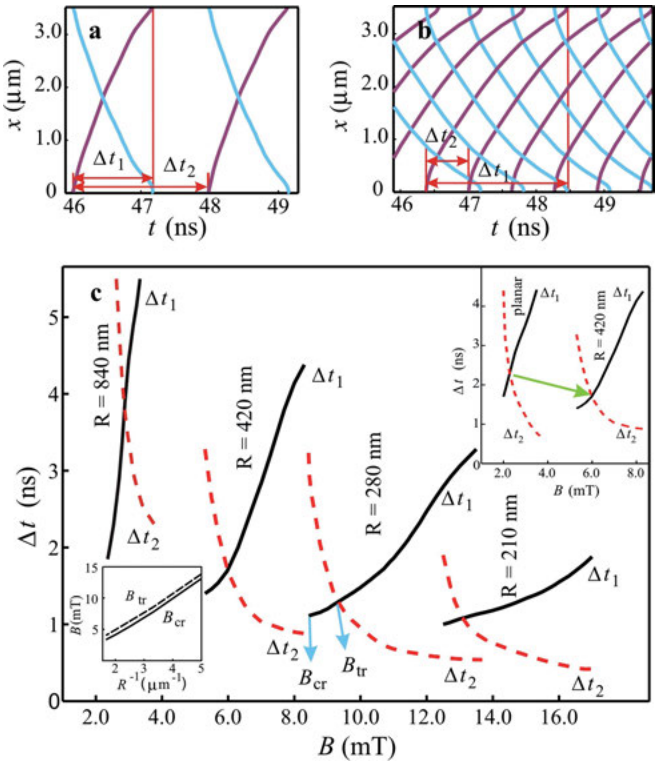

Fig. 2.3: Vortex dynamics at $\Phi/\Phi_0 = 8.5$ (a) and 11 (b) for tubes with $L = 3.5$ μm and $R = 280$ nm. The x-coordinates of the centers of vortex cores are plotted as a function of time. Characteristic times of vortex dynamics Δt_1 (solid lines) and Δt_2 (dashed lines) in tubes with $L = 3.5$ μm and a sequence of radii indicated in the figure (which form a proportion 4:2:1⅓:1; the third term practically coincides with the penetration depth) as a function of the magnetic field (c). Critical magnetic field B_{cr} and transition magnetic field B_{tr} are shown with blue arrows. Upper inset of panel (c): for comparison, are shown characteristic times of vortex dynamics of a planar film with $L_x = 3.5$ μm and $L_y = 2\pi \times 420$ nm ≈ 2.6 μm. A shift of the transition magnetic field by rolling up this film in a tube is shown with a heavy green arrow. Lower inset of panel (c): critical magnetic field B_{cr} and transition magnetic field B_{tr} for tubes with $L = 3.5$ μm as a function of the inverse radius (from [Fomin12a]).

both B_{cr} and B_{tr} increase almost linearly with the inverse radius of the tube (lower inset of Fig. 2.3c).

If the applied magnetic field is parallel to the planar surface of a 3D superconductor sample, the interaction of vortices with the surface leads to the formation of a Bean–Livingston (BL) barrier [Bean64, DeGennes66]. The BL barrier prevents vortices from entering a superconductor, unless the magnetic field is higher than the superheating field, at which the barrier vanishes. In a perpendicular magnetic field, the vortex penetration in a thin type II superconductor strip is significantly delayed due to the presence of a geometric potential barrier [Schuster94, Zeldov94].

The characteristic vortex entry rate by formation of a curved nucleus in the presence of a stationary barrier can be described by an Arrhenius-like law [Burlachkov93]. Such an approach is adequate for a stationary barrier. In the case under consideration, shown later, a barrier significantly changes in time, providing a temporary local depression, which allows for nucleation of a vortex.

The calculated dynamics of the squared modulus of the order parameter $|\psi|^2$ distribution in the tube with $R = 280$ nm is represented in Fig. 2.4 for the applied magnetic field $B = 8.8$ mT, which corresponds to the relative magnetic flux $\Phi/\Phi_0 = 8.5$. In the state shown in Fig. 2.4 for $t = 55.65$ ns, the nucleation of a vortex is impeded by a potential barrier at the edge, which occurs due to the current j_φ. As illustrated in Fig. 2.5, a steady redistribution of superconductor currents leads to a local decrease in the magnitude of the current, especially near the point $\varphi = \pi/2$, accompanied with a widening of the current profile and a developing depression of the superconductor order parameter. It is accompanied with a slight increase in the free energy of the system (calculated here for illustrative purposes). When the total current at the edge j_φ is close to zero, a barrier effectively disappears, and a vortex nucleates at the edge $x = L$ (panels at $t = 55.86$ ns in Figs. 2.4 and 2.5). This is accompanied by a lowering of the free energy of the system. Importantly, simultaneously with a nucleation of a vortex at one edge $x = L$ in the top area of the tube, another vortex nucleates at the other edge $x = 0$ in the bottom area of the tube. This is a clear manifestation of a correlation between the dynamics of vortices in both top and bottom halves of the tube. At this stage, there are two vortices moving in the tube under the influence of the Magnus force: one moving to the left at the top and another one moving to the right at the bottom ($t = 55.93$ ns to $t = 56.91$ ns).

Although the circulations of superconductor currents in both vortices are of the same sense in 3D, they are opposite when plotted on the unrolled 2D cylindrical surface of the tube in Fig. 2.6. As a consequence, the vortices – in the analyzed region of radii and magnetic fields – appear to effectively attract each other like a vortex–antivortex pair in the bulk. This scenario is confirmed by the fact that the free energy is minimal when the vortices moving in the top and bottom halves of the tube are just on one diameter. At the moment $t = 56.28$ ns, when the vortices are at the shortest distance from each other, the free energy reaches its minimum. Further on, under the influence of the Magnus force, the vortices continue their motion over the tube, overcoming the mutual attraction ($t = 56.56$ ns). Accordingly, the free energy starts to rise. At $t \approx 57.00$ ns, the vortex at around $\varphi = \pi/2$ arrives at the edge of the tube $x = 0$, where there is no barrier because the current is vanishingly small, and denucleates, while the other vortex denucleates at around $\varphi = 3\pi/2$ at the edge $x = L$. Denucleation of vortices is accompanied with an increase in the free energy of the system. Finally, at $t = 57.19$ ns, the same picture is restored, which existed at the beginning of the above-considered period.

Interestingly, our numerical data for $\mathrm{Re}\psi$ at $t = 57.19$ ns (Fig. 2.7) imply that the denucleation of vortices in a tube results in a state, in which there is already a

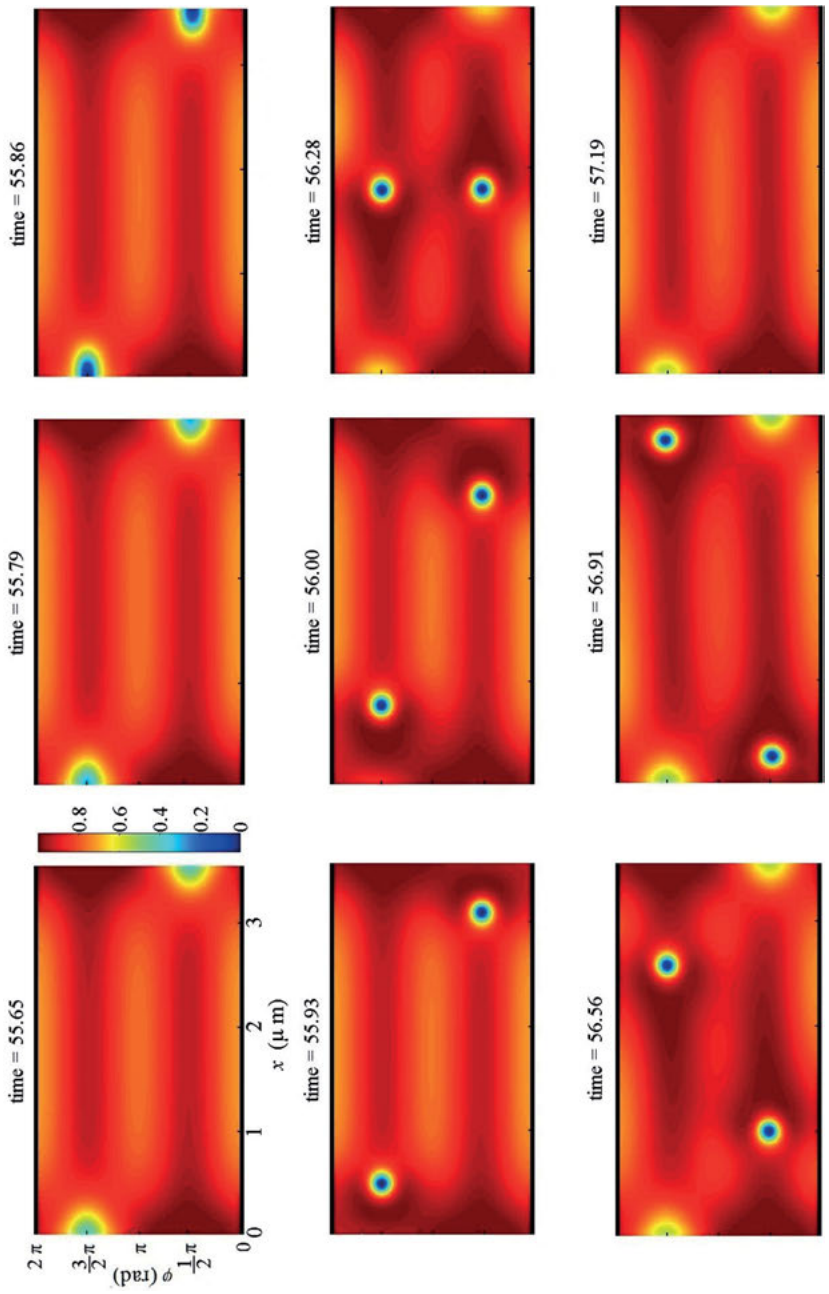

Fig. 2.4: Dynamics of the squared modulus of the order parameter $|\psi|^2$ distribution in the tube with $R = 280$ nm for $\Phi/\Phi_0 = 8.5$. In this and subsequent figures, the time (in ns) is indicated on the panels. The external current is applied through the top and bottom boundaries in the panels. The cut corresponds to the up and down boundaries in the sweep (black lines) (from [Fomin12a]).

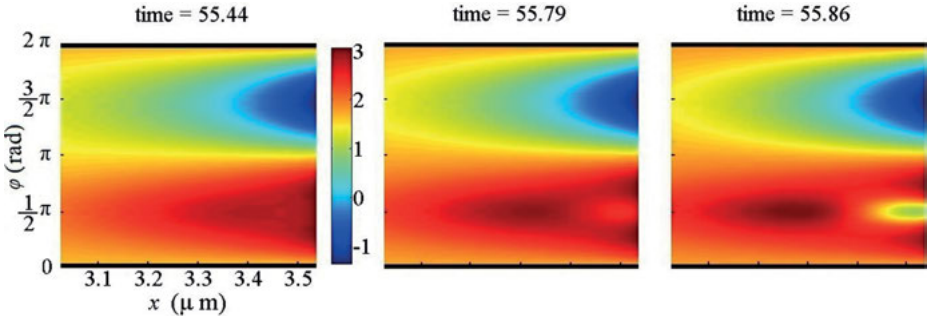

Fig. 2.5: Dynamics of the current density j_φ pattern in the vicinity of the edge $x = L$ at different time just before nucleation of a vortex in the tube with $R = 280$ nm for $\Phi/\Phi_0 = 8.5$ (from [Fomin12a]).

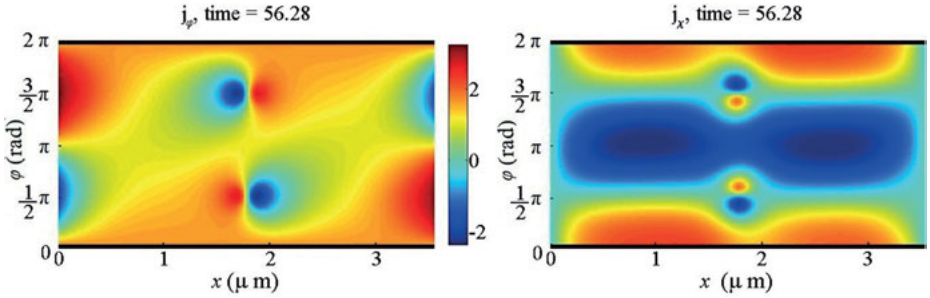

Fig. 2.6: Patterns of the superconducting currents in the tube with $R = 280$ nm for $\Phi/\Phi_0 = 8.5$, when two vortices are at the shortest distance from each other at $t = 56.28$ ns: on the unrolled cylindrical surface, the superconducting currents are circulating in the opposite directions. This makes two vortices on the cylindrical surface attract each other (from [Fomin12a]).

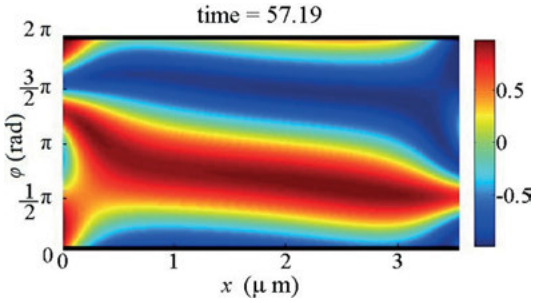

Fig. 2.7: Pattern of the Re ψ in the tube with $R = 280$ nm for $\Phi/\Phi_0 = 8.5$ at $t = 57.19$ ns (from [Fomin12a]).

strong correlation between the values of order parameter at the points of future nucleation of both vortices. Such a correlation is specific for cylindrical geometry and cannot occur in planar superconductor structures. This state "signals" the system to start a new cycle of preparing a pattern of the superconducting current, which allows for vortex nucleation.

Comparison between the characteristic times of vortex dynamics for a planar film [Fomin09] with $L_x = 3.5$ μm and $L_y = 2\pi \times 420$ nm ≈ 2.6 μm and for a tube with radius $R = 420$ nm [upper inset of Fig. 2.3c] reveals a significant (by a factor of 3 in the analyzed case) increase of both critical magnetic field B_{cr} and the transition magnetic field B_{tr} by virtue of rolling up that planar film in a tube. The distinction in vortex dynamics is due to a remarkable difference between superconducting vortex dynamics in a tube and in a planar film. The vortices in the latter repel each other. Two correlated vortices on a cylindrical surface effectively attract each other in the analyzed region of radii and magnetic fields. Hence, their motion under the action of the Magnus force leads to a simultaneous denucleation of both vortices on the opposite edges of the tube as illustrated in Fig. 2.3a.

Consequently, the experimentally achievable superconductor tubes of ~1 μm radius act as a periodic generator of correlated vortex pairs in the tunable frequency range ~0.1 to 10 GHz. The frequency is tuned by changing the magnetic field. Thus, open superconductor nanotubes provide a controllable vortex transmission line for the superconducting-vortex-based platform of quantum computing [Matsuo07].

In summary, characteristic times of nonequilibrium vortex dynamics in an open tube are significantly different as compared to the characteristic times in a planar film under the same magnetic field. This difference is caused not only by a spatial dependence of the magnetic field component normal to the cylindrical surface, but also by correlations between the states of the superconducting order parameter in the opposite areas of the cylindrical surface. Our results demonstrate new perspectives of tailoring nonequilibrium properties of vortices in curved superconductor nanomembranes and of their application as tunable superconducting flux generators for fluxon-based information technologies.

2.2 Branching of the vortex nucleation period in superconductor microtubes due to an inhomogeneous transport current

We suggest to manipulate the branching in such a superconductor structure, where the current density distribution can be controlled locally near the positions of vortex nucleation. A possible implementation of this idea is to fabricate multiple mutually isolated electrodes [Berdiyorov10], through which the transport current is introduced into the structure. A gap between any two neighboring electrodes leads to a transport current discontinuity. In a planar structure in the presence of a homogeneous magnetic field, such discontinuities become points of vortex nucleation or denucleation.

However, in a curved structure, such a geometry can be chosen that in the vicinity of the joints between the electrodes, the component of the magnetic field normal to the surface of the structure vanishes. In this case, discontinuities of electrodes do not act as points of vortex nucleation.

In the present section, we evaluate the effect of a two-component electrode on the vortex dynamics in open Nb tubes and show a possibility to efficiently control their characteristics considering branching of the vortex nucleation period as an example.

We consider a Nb superconductor open tube [Rezaev16] of radius R and length L (Fig. 2.8a) with three paraxial contacts on the edges of the slit. The "red" contact plays the role of an input contact, through which the transport current I_{in} enters. Through the "blue" contact, the current I_{out} leaves the tube. Through the "green" contact, the additional transport current I_{control} enters; it might be positive (in) or negative (out). Its role is to dynamically control the vortex nucleation. At each instant, the sum of all three currents satisfies the condition of continuity:

$$I_{\text{in}} + I_{\text{control}} + I_{\text{out}} = 0. \tag{2.8}$$

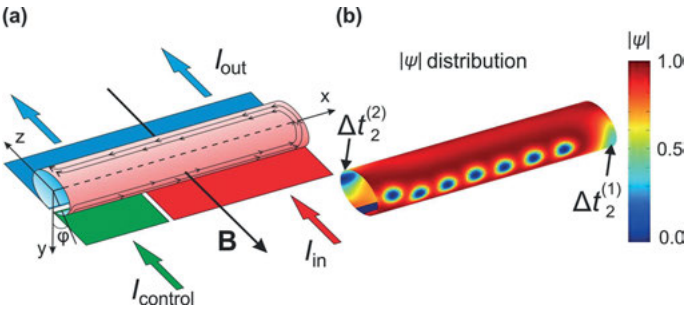

Fig. 2.8: (**a**) Scheme of an open tube. Three mutually isolated electrodes are displayed by the red, blue and green areas. The x-axis is the axis of the cylindrical coordinate frame (ρ, φ, x). The angle φ is counted from the positive direction of the y-axis, which passes through the middle of the slit. $\mathbf{B} = -B\mathbf{e}_z$ is the applied magnetic field. (**b**) An example of the pattern of the modulus of the order parameter $|\psi|$ at the magnetic field $B = 10$ mT for a tube of radius $R = 500$ nm and length $L = 3.5$ μm. Vortices nucleate at the front and back halves of the tube with periods $\Delta t_2^{(1)}$ and $\Delta t_2^{(2)}$, correspondingly, move along the x-axis and denucleate at the edge opposite to the point of nucleation (after [Rezaev16]).

The scheme of control is realized in the following way: the current I_{control} is modified by changing the potential on the *control* ("green") electrode; after that, the potential on the *input* ("red") electrode is adjusted, so that the current I_{in} keeps its constant value. The *out* ("blue") electrode is grounded, so the value I_{out} is determined from the condition of continuity (2.8).

The system is placed in a magnetic field $\mathbf{B} = -B\mathbf{e}_z$ (Fig. 2.8a), which induces Meissner currents circulating in each half-tube [Rezaev16]. The total current, which is a sum of Meissner and transport currents, is shown schematically in Fig. 2.8a by the black lines on the "front" half of the tube. Two of three currents in eq. (2.3) are independent, which allows for different regimes of control over vortex dynamics. In the present work, we keep I_{in} constant and change I_{control}.

The mathematical model is based on the TDGL eq. (2.6) with boundary conditions (2.7a, b). In refs. [Fomin12a] and [Berdiyorov09], this approach was used for studying vortex dynamics in open cylindrical tubes and kinematic vortex–antivortex lines in superconductor stripes, correspondingly. The values of the magnetic field considered in the present section belong to the 10 mT range for the temperature $T = 0.95T_c$. The empirical law, which represents the thermodynamic critical magnetic field as a function of temperature [see eq. (1.2) in [Tinkham96]]:

$$B_c(T) \approx B_c(0)\left[1-(T/T_c)^2\right], \tag{2.9}$$

in view of eqs. (5.18) and (4.62) in ref. [Tinkham96] is applicable for the first (B_{c1}) and second (B_{c2}) critical magnetic fields and thereby provides an estimate of the magnetic field range, where vortices occur at different temperatures. The electric field penetration depth [Ivlev84] is evaluated to be of the order of 10 nm, which is more than two orders of magnitude less than the typical sizes of the structures under consideration. Under these circumstances, the electrostatic potential has a low impact on the period of vortex nucleation.

The normal (with respect to the cylindrical surface) component of the magnetic field, according to Fig. 2.8a, is $B_{\text{n}} = B\sin(\varphi)$. The vector potential is taken in the Landau gauge: $\mathbf{A} = A\mathbf{e}_x,\ A = -By$. Transport currents in eq. (2.8) are obtained from the current densities $\mathbf{j}_{\text{tr}}$ in the boundary conditions of eq. (2.7b) by integrating along the appropriate contacts. The thickness of the superconductor wall, which is necessary to calculate the electron mean free path, constitutes 50 nm [Rezaev16]. The typical tube radius and length under consideration are more than 10 times larger than the thickness. With these parameters, it is safe to neglect the effect of an induced magnetic field and to use a 2D approximation. Our numerical simulations show that the induced magnetic field is as low as 1% of the applied magnetic field. The coherence length (taken at the temperature $0.95T_c$) constitutes $\xi = 56$ nm [Rezaev16]. The numerical scheme is based on the explicit finite-difference time-domain method. We trace how the random initial distribution of the order parameter evolves to a quasistationary state, which manifests vortex dynamics.

Two full-side electrodes generate symmetrical dynamics – both halves of the tube demonstrate the same characteristic times [Rezaev16]. In what follows, the period of vortex nucleation Δt_2 is considered to characterize the vortex dynamics, since it has a more pronounced dependence on the current density, than the duration of the vortex motion through the tube Δt_1. Hereinafter, we use the denotation $\Delta t_2^{(1)}$ for

the half-tube with input and control electrodes (front side in Fig. 2.8a) and $\Delta t_2^{(2)}$ for the half-tube containing the output electrode (back side in Fig. 2.8a). For a tube of radius $R = 400$ nm with two full-side electrodes carrying the current $I = 1.7$ mA at $B = 10$ mT, the nucleation period $\Delta t_2^{(1)} = \Delta t_2^{(2)} = \Delta t_2^{(\mathrm{sym})} = 1.2$ ns (this value is shown in Fig. 2.9 by the black solid line). However, introducing the control electrode of length $L_{\mathrm{control}} = 20\xi$ into the tube of length $L = 60\xi$ (so that the input electrode is of length $L_{\mathrm{in}} = 40\xi$) violates the inversion symmetry of the modulus of order parameter with respect to the geometric center of the tube. A similar mechanism occurs in vortex ratchets with a pinning potential, which lacks central symmetry [Silhanek10].

In Fig. 2.9, the dependence of Δt_2 on the control current demonstrates a different behavior for each half-tube. We perform simulations for two radii of the tube. In Fig. 2.9, the blue line corresponds to $R = 600$ nm and the red one to $R = 400$ nm. An increase of the radius shifts both $\Delta t_2^{(1)}$ and $\Delta t_2^{(2)}$ curves upward. As shown in Fig. 2.9, a difference between vortex nucleation periods $\Delta t_2^{(1)}$ and $\Delta t_2^{(2)}$ by a factor of as large as 3 is achieved. This difference, as follows from our simulation, is determined by the control current. Because of inhomogeneity of the current density distribution over the whole tube, a variation of the control current at one side of the tube leads to a change of the vortex nucleation period at the opposite side. A further decrease of the control current (beyond the values given in Fig. 2.9) leads to a dramatic rise of $\Delta t_2^{(2)}$, which means that vortex nucleation is blocked on one side of the tube and the dynamics occurs completely on another side of the tube.

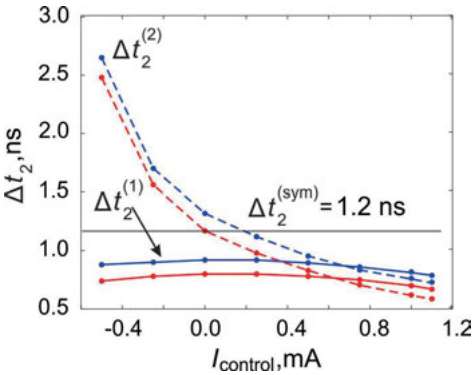

Fig. 2.9: Vortex nucleation period as a function of the control current. The blue line corresponds to the tube of radius $R = 600$ nm and the red line to $R = 400$ nm, the length of both tubes $L = 60\xi = 3{,}360$ nm, the length of the control electrode $L_{\mathrm{control}} = 20\xi = 1{,}120$ nm. The input current is equal to 1.7 mA. $\Delta t_2^{(2)}$, $\Delta t_2^{(1)}$ are periods of vortex nucleation at the opposite sides of a tube. A black solid line represents the case of full-side electrodes, when input and output currents are equal by modulus to 1.7 mA for $R = 400$ nm. In all cases the magnetic field $B = 10$ mT (from ref. [Rezaev16]).

A variation of the control current from negative to positive values shows a crossover between $\Delta t_2^{(2)}$ and $\Delta t_2^{(1)}$ functions. For the radius $R = 600$ nm, the crossover occurs at $I_{\text{control}} = 0.70$ mA, and for $R = 400$ nm, it occurs at $I_{\text{control}} = 0.62$ mA. The dependence of $\Delta t_2^{(2)}$ on I_{control} after passing the crossover point is less expressed than before: $\Delta t_2^{(2)}$ is even reduced as compared to $\Delta t_2^{(1)}$.

From the practical point of view, it is interesting to evaluate the average number of vortices per nanosecond, when the dynamics occurs only at one side of the tube. In the tube with radius $R = 400$ nm, the length of the control electrode $L_{\text{control}} =$ 1,120 nm and $I_{\text{control}} = -0.5$ mA, which is analyzed here as a typical case, the characteristic times $\Delta t_2^{(2)} \to \infty$ and $\Delta t_2^{(1)} \approx 0.7$ ns result in the average number of vortices $n_v \approx$ 1.43 per nanosecond. In a tube with full-side electrodes, $n_v \approx 1.67$ per nanosecond, so that the relative difference in the average number of vortices constitutes ~15% for the same input current. Thus, using inhomogeneous transport current in the tube leads to an effective decrease of the average number of vortices. Such a decrease plays a crucial role in noise and energy dissipation reduction for numerous superconductor applications [Milosevic10, Lee99, Silhanek10]. In fact, the property $\Delta t_2^{(2)} \to \infty$ implies that using multiple electrodes allows for vortex removal from certain regions of a superconductor sample, which is of practical interest, for example, in order to suppress the $1/f$ noise due to the activated hopping of trapped vortices and thus to extend the operation regime of superconductor-based sensors to lower frequencies [Lee99].

Vortex dynamics occur under the Magnus force [**j, B**] and linearly depend on the local current density [Tinkham96]. Geometry of boundaries in mesoscopic superconductors determines the points of nucleation, denucleation and possible location of vortices [Hu11a], and the corresponding current density distribution leads to the nonlinear character of vortex motion as a function of the control current. The branching of the vortex nucleation period shown in Fig. 2.9 is an example of nonlinear dynamics. An interpretation of such a behavior of vortices requires to analyze the supercurrent density. In Fig. 2.10, the key mechanism of the difference between vortex dynamics in the cases with (Fig. 2.10b) and without (Fig. 2.10a) a control electrode is illustrated. Near the points of vortex nucleation for both halves of the tube, the current density components are listed in the rectangles. The black and light gray thin arrows on each panel in Fig. 2.10 point to the same positions on the tube. As clearly shown, the main reason for the difference in vortex dynamics is a change of the supercurrent density component j_s along the azimuthal direction (a corresponding coordinate $s = R\varphi$ is defined through the azimuthal angle φ shown in Fig. 2.8). From comparison of two bottom panels in Fig. 2.10, a decrease of this component at the points of vortex nucleation specified by the black thin arrows on the side of the output electrode ($j_s^a - j_s^b = 2.49 - 2.39 = 0.1$) is higher than the current density increase ($j_s^b - j_s^a = 2.42 - 2.39 = 0.03$) at the points shown by light grey thin arrows on the side of the input electrode. At the same time, the j_x components are similar to each other in both cases.

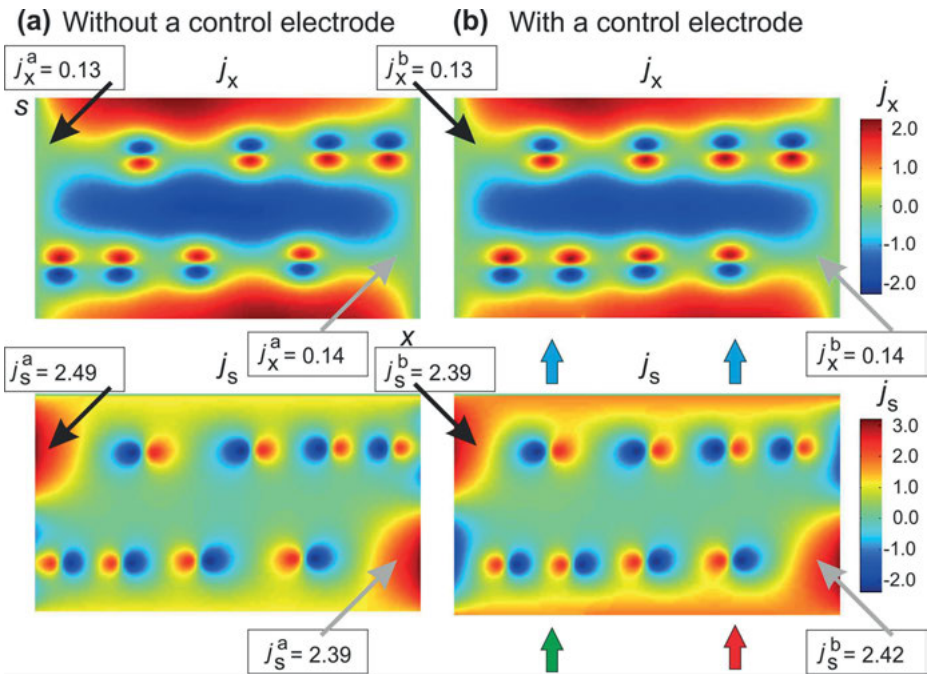

Fig. 2.10: Patterns of the j_x and j_s components of the current density on the surface of a tube in the (x, s) coordinates, where x is defined in Fig. 2.1a and $s = R\varphi$. Radius of the tube is $R = 400$ nm. The magnetic field is $B = 8$mT. (a) Two full-side electrodes are attached: input and output ones with the transport current $I = 1.7$ mA. (b) Input, control and output electrodes of length $L_{in} = 40\xi$, $L_{control} = 20\xi$ and $L_{output} = 60\xi$, correspondingly, are attached. The currents are $I_{in} = 1.7$ mA and $I_{control} = 0.75$ mA. The green, red and blue arrows show the control, input and output currents, correspondingly (after [Rezaev16]).

The vortex nucleation period is a decreasing function of the magnetic field as shown in Fig. 2.11a for two cases, without and with the applied control current 0.5 mA. For higher values of the control current, the difference between $\Delta t_2^{(2)}$ and $\Delta t_2^{(1)}$ is less pronounced, than for lower values of the control current (see, for instance, a crossover point in Fig. 2.9 for a fixed magnetic field).

For a lower magnetic field, the absolute value of the difference between the two periods is larger, than for a higher magnetic field. For example, $|\Delta t_2^{(2)} - \Delta t_2^{(1)}| \approx 0.6$ ns for $B = 8$ mT and $|\Delta t_2^{(2)} - \Delta t_2^{(1)}| \approx 0.3$ ns for $B = 20$ mT for the case without a control current. However, the relative difference $\delta_{21} = |\Delta t_2^{(2)} - \Delta t_2^{(1)}|/\Delta t_2^{(2)} \approx 0.4$ is varying at most by 5% within the considered range of magnetic fields. Since the $\Delta t_2^{(2),(1)}(B)$ curves saturate with the magnetic field growth [Rezaev15], the relative difference δ_{21} keeps almost steady for the whole range of magnetic fields, where vortex dynamics occur. Qualitatively, the functions $\Delta t_2^{(2),(1)}(B)$ have the same shape for the control current $I_{control} = 0.5$ mA (see the blue lines in Fig. 2.11a), for which the relative difference δ_{21} is about 0.1.

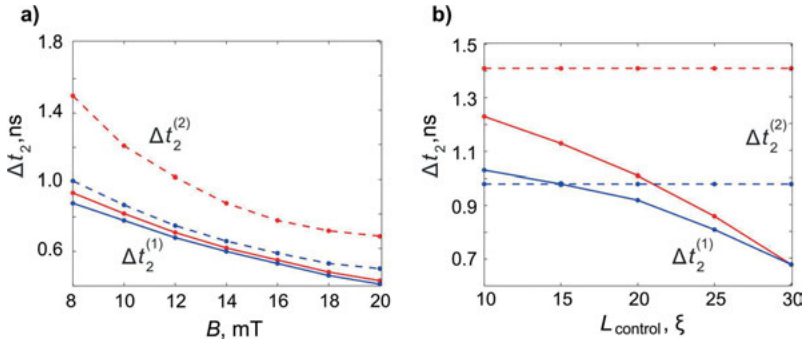

Fig. 2.11: $\Delta t_2^{(2)}$ and ($\Delta t_2^{(1)}$) are denoted by dashed (solid) lines, correspondingly. (a) The vortex nucleation period as a function of the magnetic field for the tube of radius $R = 400$ nm, the input current $I_{in} = 1.7$ mA and the control electrode of length $L_{control} = 20\xi$. (b) The vortex nucleation period as a function of the control electrode length for the tube of radius $R = 400$ nm and the input current $I_{in} = 1.5$ mA at the magnetic field $B = 10$ mT. In both panels, the red lines correspond to the case without a control current and the blue lines are drawn for $I_{control} = 0.5$ mA (after [Rezaev16]).

The relative difference δ_{21} strongly depends on the length of the control electrode, as shown in Fig. 2.11b. For $I_{conrtol} = 0$ mA and the control electrode of length $L_{control} = 10\xi$, the relative difference is $\delta_{21} \approx 0.14$, while for the length $L_{control} = 30\xi$, the relative difference is significantly larger: $\delta_{21} \approx 0.52$. The main reason for this dramatic change is a decrease of $\Delta t_2^{(1)}$ more than twice, while $\Delta t_2^{(2)}$ only slightly depends on $L_{control}$. The decrease of $\Delta t_2^{(1)}$ in Fig. 2.11b results from the change of the length of the input electrode, correlated with the length of the control electrode. In particular, the input current density j_{in} rises in the vicinity of the vortex nucleation point, which leads to an effective reduction of the potential barrier (see Fig. 2.5). The vortex nucleation period $\Delta t_2^{(1)}$ decreases, while the corresponding period $\Delta t_2^{(2)}$ at the opposite side of the tube remains practically unchanged, since the output current density is not affected by changing the length of the input electrode.

Thus, the interplay of a curved geometry with an inhomogeneous transport current determines a specific current density distribution, which destroys the inversion symmetry of the order parameter with respect to the geometric center of the tube and leads to a branching of the vortex nucleation period. In particular, using the appropriate electrode arrangement, the vortex dynamics can be blocked on one side of the tube. The relative change of the vortex nucleation period weakly (by about 5%) depends on the magnetic field in the range, where vortex dynamics occur for the considered control currents. However, it strongly depends on the length of the control electrode (in particular, the relative difference between the characteristic times $\Delta t_2^{(2)}$ and $\Delta t_2^{(1)}$ can be modified by a factor of 5). The proposed method allows for tuning the frequency of vortex generation on different parts of the tube and provides a reduction of the average number of vortices per nanosecond, which is important for noise and energy dissipation

reduction in superconductor applications, in particular, for an extension of the operation regime of superconductor-based sensors.

2.3 Voltage induced by superconducting vortices in open nanostructured microtubes

Nanostructuring of type II superconductor materials, which has been developed into the mature technology during the last two decades, provides a way to significantly modify the critical superconducting parameters. Widely known is the enhancement of a critical current by introducing artificial pinning centers, for example, an array of holes fabricated using either lithographical or ion-irradiation technique [Hilgenkamp03, Baert95, Ray13, Vlcek93]. Formation of a periodic lattice of pinning sites results in effects arising due to incommensurability between the vortex lattice and the lattice of pinning sites [Reichhardt97, Chiliotte09]. Other superconducting critical parameters, critical magnetic field and critical temperature, are reported to be modified by nanostructuring [Nishio08, Lara15]. Superconducting properties are controlled by imposing various geometric constraints at the micro- and nanoscale [Misko09, Grigorieva07, Henrich12, Henrich13a]. This effect occurs due to the impact of the confinement symmetry on the vortex pattern. Geometric restrictions can dramatically change magnetic properties of superconductors, for example, a giant reentrance of vortex pinning induced by increasing magnetic field is detected in a W-based nanowire [Cordoba13]. A pure boundary-stimulated effect of vortex dipole generation due to the interaction of the Meissner current with a pinning center in a superconductor sample is reported [Ge15].

A number of interesting effects are revealed due to hybridization of the reduced dimensionality with curved geometry of superconductor samples. In particular, fluxoid quantization is detected through magnetoresistance oscillations in various superconductor samples ranging from cylinders in earlier experiments to submicron loops more recently [Little62, Moshchalkov95, Tinkham63]. Curvature is found to be the key factor that controls depression of the critical temperature in a thin cylindrical superconductor shell as a function of the angle between the axis of the cylinder and the applied magnetic field [Meservey72].

The present section is aimed at a quantitative analysis of how self-rolling of the planar superconductor membranes modifies their transport properties. The voltage generated by moving vortices as a function of the applied magnetic field provides useful insight into spatial reorganization of the dynamical vortex patterns in self-rolled superconductor open tubes.

We focus on the superconducting properties of Nb tubes with typical for roll-up technology dimensions: length $L = 5$ μm and radius R of about 500 nm made from a 50 nm-thick film [Thurmer08, Thurmer10]. Figure 2.12 shows a scheme of the system under consideration. Two paraxial electrodes are attached to both edges of the

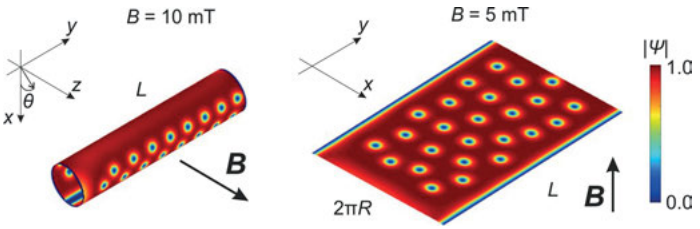

Fig. 2.12: L.h.s. panel: Scheme of a tube with a slit (open tube). The y-axis is selected as the polar axis of cylindrical coordinates (ρ, θ, y). The azimuthal angle θ is counted from the direction of the x-axis passing through the middle of the slit. The external magnetic field $\mathbf{B} = B\mathbf{e}_z$ is directed along the z-axis. The plot represents the distribution of the amplitude of the order parameter $|\psi|$. Vortices nucleate at the top (relative to the direction of the magnetic field) half-tube at the right edge, move in the direction of the y-axis and denucleate at the left edge and vice versa at the bottom half-tube [Fomin12a]. R.h.s panel: Distribution of the amplitude of the order parameter in a planar membrane (from [Rezaev19]).

slit in order to provide the transport current. The width of the slit is supposed to be much smaller compared to the circumference $2\pi R$. Electrodes extend through the entire slit edges. The system is placed in the magnetic field $\mathbf{B} = B\mathbf{e}_z$ (see Fig. 2.12), which induces Meissner currents circulating at each half-tube [Fomin12a]. The temperature of the tube is taken close to the critical one $T = 0.95T_c$, where $T_c = 9.2$ K. The superconducting state of the Nb tube with parameters presented in Table 2.2 is described by the TDGL equation for the complex-valued order parameter ψ [Dobrovolskiy12, Tinkham96, Gropp96] in the dimensionless form:

$$\frac{\partial \psi}{\partial t} = \left(\frac{\nabla}{\kappa} - i\mathbf{A}\right)^2 \psi + \left(1 - |\psi|^2\right)\psi - i\kappa\varphi\psi, \tag{2.10}$$

Table 2.2: Physical and geometrical parameters of the Nb film used for simulation (from [Rezaev19]).

	Denotation	Value
Penetration depth	λ	273 nm
Coherence length	ξ	58 nm
GL parameter	$\kappa = \lambda/\xi$	4.7
Fermi velocity	v_F	6×10^5 m/s
Thickness of the film	d	50 nm
Mean free electron path	l	6.0 nm
Diffusion coefficient	$D = lv_F/3$	12×10^{-4} m^2/s
Relative temperature	T/T_c	0.95
Normal conductivity [Dobrovolskiy12]	$\sigma = l/\left[3.72 \times 10^{-16}(\Omega \cdot \text{m}^2)\right]$	16 $(\mu\Omega \cdot \text{m})^{-1}$

where φ is the electric scalar potential. The boundary conditions (2.7a) imply the zero value of normal component of the superconducting current at the edges of the system without electrodes. The scalar potential φ is found as a solution of the Poisson equation coupled with TDGL equation (2.10):

$$\Delta\varphi = \frac{1}{\sigma}\nabla \cdot \mathbf{j}_{sc}, \tag{2.11}$$

where the superconducting current density is defined as $\mathbf{j}_{sc} = \frac{1}{2i\kappa}\left(\psi^*\nabla\psi - \psi\nabla\psi^*\right) - \mathbf{A}|\psi|^2$ and σ is the normal conductivity. The transport current density $j_{\mathrm{tr}}(y) = \mathrm{const} \equiv j_{\mathrm{tr}}$ is imposed via the boundary conditions for eq. (2.11) at the edges, to which electrodes are attached: $\mathbf{n} \cdot \nabla\varphi|_{\mathrm{electrode}} = -(1/\sigma)j_{\mathrm{tr}}$. Vector potential components $A_s(s,y)$ and $A_y(s,y)$ (where $s = R\theta$) are chosen in the Coulomb gauge: $A_s(s,y) = 0;\ A_y(s,y) = BR\cos\left(\frac{s}{R}\right)$. The set of eqs. (2.10) and (2.11) is solved numerically, based on Link-Variables technique (see [Gropp96]). The relaxation method is used with the random initial distribution $\Psi(s,y)$ of the order parameter. In the presence of the magnetic field ($B > B_{c1}$) and the transport current, the order parameter evolves to a quasistationary state, which is characterized by the periodic vortex nucleation/denucleation at the edge domains with the highest/lowest value of the normal to the surface component of magnetic field (see Fig. 2.12) [Gropp96, Kato93, Kogut79, Saad96]. Vortices are moving paraxially along the tube and generate the electric field, which is directed oppositely to the transport current density [Fomin12a]. Finally, the voltage $\langle\Delta\Phi\rangle$ averaged over time and the electrode length is obtained.

The effect of the vortex creep due to the activation from pinning centers is not of primary relevance in the system under consideration because the thickness of a membrane is less than the coherence length ξ. The pinning energy U_0 is a fraction of the maximum superconducting condensation energy of the vortex core $U_p \cong B_c^2\xi^2 d$, where B_c is the thermodynamic critical field and d is the film thickness [Embon15]. Because of this relation, the effect of vortex creep due to the activation from pinning centers is much more pronounced in bulk (3D) materials than in systems of lower dimensions [Burlachkov94]. Under these conditions, in the present analysis, a vortex is rather a topological defect at the 2D scale than a vortex line common at the 3D scale.

The typical vortex diameter in systems under consideration is about 100 nm ($d_v \sim 2\xi$). This value suggests the interval of tube radii, where the vortex dynamics and the spatial vortex distribution should significantly depend on the curvature. Vortices exist on the surface of the tube in the azimuthal sectors approximately between $\theta_1 \approx \pi/4$ and $\theta_2 \approx 3\pi/4$ at the top half-cylinder and between $\theta'_1 \approx 5\pi/4$ and $\theta'_2 \approx 7\pi/4$ at the bottom half-cylinder (see Fig. 2.12). When the number of vortex chains in the azimuthal direction exceeds a value from 9 to 10, the hexagonal lattice emerges. Starting from this regime, the effect of the curvature should be negligible,

since the vortex configuration corresponds to the planar structure. It follows from these numbers that for the prominent curvature effects, the radius of the tube should belong to the interval from 70 to 700 nm. Aimed at the state-of-the-art and feasible in the future self-rolled Nb structures, we consider the radius of tubes in the interval from 300 to 700 nm [Thurmer08, Thurmer10]. The numerical simulations for the current–voltage characteristics (CVCs) (see Fig. 2.13) show a little variation with radii larger than 450 nm in the magnetic field $B = 20$ mT for the transport current density j_{tr} ranging from 10 to 70 GA/m^2.

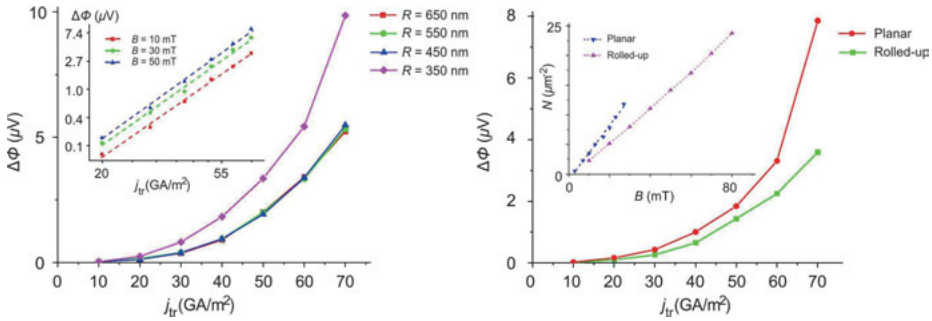

Fig. 2.13: L.h.s. panel: CVCs for different tube's radii with $L = 5$ μm. The external magnetic field $B = 20$ mT. The inset: CVCs for the tube with $R = 550$ nm in the logarithmic scale for the values of the magnetic field 10, 30 and 50 mT. R.h.s. panel: Comparison of the CVCs for a planar membrane (red solid line) and a self-rolled tube (green solid line) with $R = 550$ nm and $L = 5$ μm. The width and length of the planar membrane are 5 μm and 3.5 μm, correspondingly. The external magnetic field is $B = 10$ mT. Inset: Number of vortices per unit area as a function of B for the self-rolled tube (purple dashed line) and the planar membrane (blue dashed line) (from [Rezaev19]).

For all cases in Fig. 2.13, the voltage is a monotonically increasing function of both the transport current density and the magnetic field (see the inset in the l.h.s panel). The voltage is larger for smaller radii. At the transport current density $j_{tr} = 70$ GA/m^2 and the magnetic field $B = 20$ mT, there is an almost twofold growth of the vortex-induced voltage (10 μV vs. 5 μV) for $R = 350$ nm versus $R = 450$ nm. This increase demonstrates the impact of the curvature on the dissipative characteristics of the superconducting sample. To explain the difference between the induced voltages, we address the characteristic times of vortex dynamics – the period of nucleation at the edges Δt_2 and the time Δt_1, during which a vortex passes the distance L. The interplay of these characteristic times specifies the velocity of moving vortices [Fomin12a]. For smaller radii, the resulting velocity of vortices is higher as compared to the case of larger radii. This leads to a higher voltage in the former case, as long as the induced voltage is directly proportional to the velocity of vortices.

In the r.h.s panel of Fig. 2.13, the induced voltages on the tube having the radius $R = 550$ nm and the length $L = 5$ μm are compared with the induced voltages on the corresponding planar membrane, from which the tube is fabricated. The difference between voltages may be as large as twofold. The difference is more pronounced for higher values of the transport current density. It occurs due to various vortex dynamics in tubes versus planar membranes with the distinct current distributions in both cases [Fomin12a]. The current distribution in curvilinear structures with the paraxial transport current determines their transport or magnetic properties [Gladilin12, Sabatino11]. In the open tubes under analysis, the paraxial transport current would induce the azimuthal vortex motion of a rather restricted spatial range. At the same time, the azimuthal transport current leads to the paraxial motion of vortices extended along the whole tube; therefore this configuration of the transport current is selected as foreground. In this case, the characteristic times for the planar membranes are much bigger as compared to the tubes of the same dimensions subject to the same magnetic field at the same current density. The velocity of vortices moving in planar membranes is lower than that in tubes. However, at the same magnetic field, the number of moving vortices is larger in a planar membrane (see, for example, Fig. 2.12, where the total number of vortices in the planar membrane is larger even for a lower magnetic field). Since the generated voltage is accumulated from all vortices additively, the cumulative effect results in a higher voltage for the planar membrane as compared to the tube. The above-described character of voltage demonstrates sustainability (at least in the considered range of the magnetic field between 0 and 50 mT) of the lower dissipation in tubes as compared to planar membranes with the same dimensions and under the same boundary conditions and magnetic fields.

The voltage as a function of the magnetic field is presented in Fig. 2.14 at a fixed value of the transport current density for both the planar membrane and the tube. For the tube (green line), it is a piecewise-linear function, which consists of two (approximately linear) lines with different slopes. The value of the slope changes at the inflection point from 0.19 to 0.03 μV/mT, what means that the induced voltage growth with the magnetic field becomes sixfold lower, implying a switch between two regimes of vortex dynamics, which will be discussed below. In the planar membrane, there is no such a transition between regimes of vortex dynamics through $\Delta\Phi(B)$ (the red line). Visualization of the order-parameter distribution on the tube for magnetic fields just before and after the inflection point in Fig. 2.14 reveals a shift of the chain of moving vortices into the region with lower values of B_n (see inset in Fig. 2.14). Since B_n in a planar membrane is homogeneous, there is no such a shift of the chain of moving vortices.

Analysis of vortex dynamics on the tube leads to the following reasons for the aforementioned shifts. The shift of the chain of moving vortices with rising the magnetic field is caused by the occurrence of a quasistatic chain of vortices, which repels the active chain of moving vortices toward the azimuthal position, where $|B_n|$ is lower. When the number of vortex chains $N_{ch} > 1$, in each half-tube, there is one

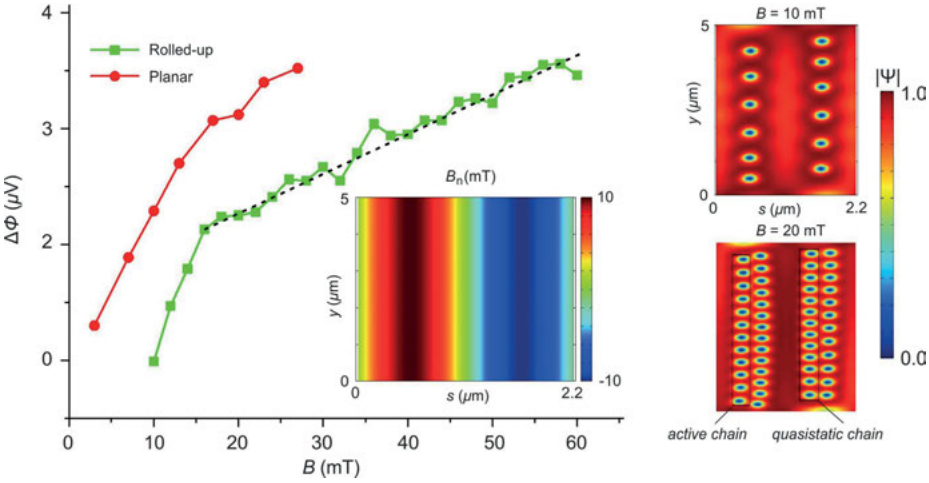

Fig. 2.14: L.h.s. panel: Induced voltage as a function of the external magnetic field B for the self-rolled tube with $R = 350$ nm (green solid line) and the planar membrane with the side $2\pi R$ (red solid line). The transport current density $j_{tr} = 50$ GA/m^2. Inset: the normal to the surface component $B_n = B\sin(\theta)$ of the external magnetic field ($B = 10$ mT) in the tube with $R = 350$ nm. R.h.s. panels: Snapshots of $|\psi(s,y)|$ at two external magnetic fields ($B = 10$ and 20 mT) for the open tube with $R = 350$ nm and $j_{tr} = 50$ GA/m^2 (from [Rezaev19]).

active chain of moving vortices, which is the closest one to the slit edge, while all other chains can be considered as quasistatic: vortices in these chains oscillate near their points of equilibrium. Quasistatic chains seem to be pinned to the surface, while vortices from the active chains move fast paraxially. A further increase of the magnetic field slows down the vortex motion and simultaneously increases the total number of vortices, while the moving vortices are shifted toward the slit edges. Hence, the induced voltage, which is proportional to the normal to the surface component of magnetic field B_n and the vortex velocity, tends to grow with the magnetic field much slower as compared to the case of one chain. Analysis of the voltage induced by moving vortices as a function of the magnetic field in conjunction with the vortex pattern suggests a possibility of the experimental study of vortex dynamics in open nanostructured microtubes by measuring this voltage.

Thus, rolling up superconductor nanomembranes gives rise to qualitatively new regimes of vortex dynamics that produce less dissipation. The average voltage induced by moving vortices in a self-rolled microtube is simulated to be twice smaller in comparison with the unrolled planar nanomembrane. A transition between different vortex patterns in a microtube results in a more than sixfold change of the slope of the voltage as a linear function of the magnetic field.

Under a strong transport current, the induced voltage in an open superconductor microtube shows a pulse on a certain interval of the magnetic field (see Fig. 2.15e). It is

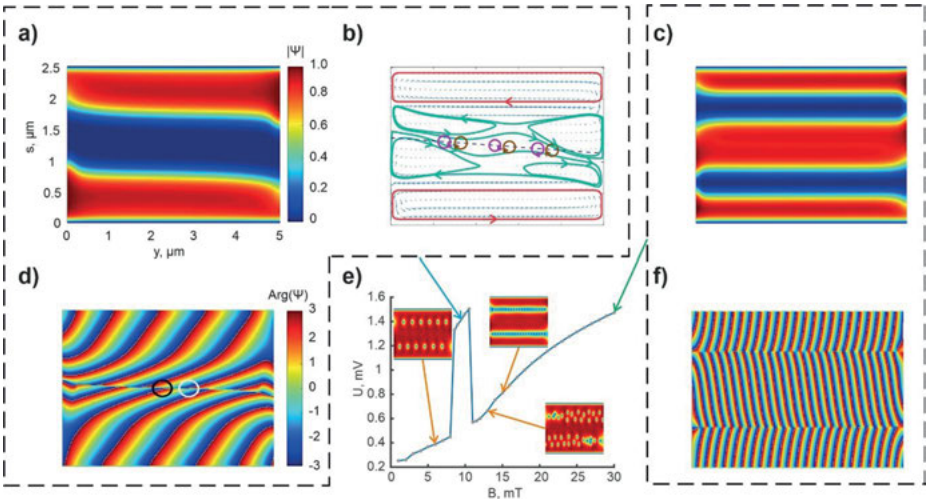

Fig. 2.15: The modulus (a) [(c)] and the phase (d) [(f)] of the order parameter and the streamlines of the superconducting current (b) in a Nb nanotube of radius 400 nm under the applied magnetic field 10 mT [30 mT]. Red lines are disconnected loops of SSCs flowing in both half-tubes. The current distribution within the phase-slip region (blue area in panel (a)) consists of two new disconnected loops (green lines in (b)), between which the (dashed) line of fast dynamics of vortex–antivortex pairs (burgundy and brown circles) occurs. The voltage induced due to the moving vortices as a function of the magnetic field (e); distributions of the modulus of the order parameter for a few magnetic fields are shown in insets. All results are obtained at $T/T_c = 0.95$ for the transport current density $j_{tr} = 20$ GA/m^2 (from [Rezaev20]. This work is licensed under a Creative Commons Attribution 4.0 International License, http://creativecommons.org/licenses/by/4.0/.).

a manifestation of a wide phase-slip domain. The topological transition accompanying the phase-slip effect consists in the occurrence of two new loops of weak superconducting currents connecting two regions of superconducting screening currents (SSCs), which are disconnected in case of vortex-chain dynamics. Namely, the green loops of SSCs in Fig. 2.15b connect front and rear half-tubes, thus introducing a new topology of the superconducting current. A topological transition from two disconnected regions of SSCs (red) to four (red and green) and then back to two (red) such regions occurs with increasing the magnetic field for certain intervals of values of the transport current. Under these conditions, in open tubes, the vortex nucleation locus connects both halves of the tube (Fig. 2.15b), as distinct from the previously known cases, when kinematic vortex–antivortex pairs do not occur and the both halves of the tube are strictly disconnected (Fig. 2.15c). Generation of the vortex–antivortex pairs marked with white and black circles in Fig. 2.15d results from (i) their unbinding due to the high transport current and (ii) motion due to the Magnus force caused by the magnetic field. Nucleation and separation of vortex–antivortex pairs at the side of the microtube, which is opposite to the slit, are followed by their motion till (i) their denuncleation at the sides of the

tube or (ii) annihilation of a vortex from the pair with an antivortex from a neighboring pair (respectively, an antivortex from the pair with a vortex from another neighboring pair), when there exist two or more vortex–antivortex pairs. The relatively fast motion of the vortices and antivortices (with the vortex/antivortex lifetime about 1×10^{-14} s) on the side of the microtube, which is opposite to the slit, leads to an apparent picture of an extended static phase slip (Fig. 2.15a).

In summary, self-rolling of nanomembranes allows for the submicron-scale inhomogeneity of the normal to the surface component of magnetic field. If the applied magnetic field is orthogonal to the axis of a microtube, which carries a transport current in the azimuthal direction, the phase-slip regime is characterized by the vortex/antivortex lifetime ~10^{-14} s versus the vortex lifetime ~ 10^{-11} s for disconnected vortex dynamics in the half-tubes. The phase-slip dynamics determine the magnetic field–voltage characteristics and CVCs in self-rolled superconductor nanoarchitectures.

2.4 Superconducting properties of micro- and nanohelices

Due to the *chiral geometry*, helical nanoarchitectures provide a significant advancement in modern nanosciences and nanotechnologies. Helical structures have been synthesized of various materials, including carbon-based [Motojima90, Amelincx94, Zhang14], all-semiconductor [Prinz00] and hybrid metal–semiconductor [Zhang05] nanocoils and nanocoils of semiconductor oxides [Kong04]. Because of their unique morphology as well as mechanical, electrical, magnetic and optical properties, nanospirals have attracted interest for application as electromagnetic actuators and sensors [Bell06], micro- and nanoelectromechanical systems [Dong06], nanoscale energy storage [Gao06], photodetectors [Hwang08], smart electric conductors, magnetic sensors and electromagnetic wave absorbers [Gao11].

Fabrication, characterization and application of spiral-shaped structures are of central interest for the advancement of superconductor technologies. The main attention in this field has been attracted to planar (2D) structures. For instance, X-ray [Gol'tsman01] and single-photon [Dorenbos08, Henrich13b] detectors based on superconductor nanowire planar spirals have developed into a mature technology [Natarajan12]. Spiral antennas are shown to produce a very effective coupling between hot-electron bolometers [Zhang13]. Superconductor spiral resonators have revealed potential for constructing one-, two- and three-dimensional metamaterials [Ghamsari13]. Superconducting metamaterials made up of planar spiral Nb elements have provided minimized Ohmic losses, compact design with high quality factor and sensitive tuning of resonant frequency via temperature and magnetic field [Kurter10]. The radio frequency current distributions in Nb planar spiral resonators along the width of the individual turns of the resonators reveal an unconventional behavior: the maximum current is observed in the middle of the structure, which is associated with the geometry and the cancellation of magnetic field between

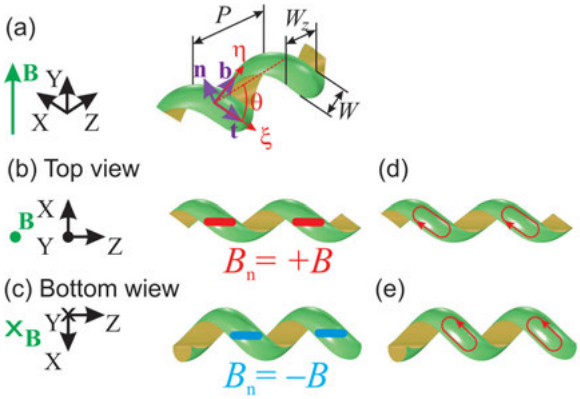

Fig. 2.16: (a) Schematics and geometrical parameters (see the text) of a helical coil. The spiral axis is along the *z*-axis. The magnetic field **B** is along the *y*-axis. At any point of the helical surface, **t**, **n** and **b** denote, correspondingly, tangential, normal and binormal unit vectors. (b) [(c)] Scheme of the areas with the maximal [minimal] values of the normal component of the magnetic field $B_n = B$ [$B_n = -B$]. The linear extent of those areas along the *z*-axis is of the order of W_z. (d) [(e)] Scheme of a set of superconducting screening currents in the top [bottom] parts of the helical turns (from [Fomin17]).

the turns [Zhuravel12]. This is favorable for handling high powers and thus expands the range of applicability for radio frequency/microwave resonators.

Macroscopic superconductor tapes of various materials (from Nb_3Sn [Garber76] to high-T_c [Mukoyama06, Noji07, Clem10]) helically wound around a cylinder have been intensively explored with the aim of reducing losses and cost of power transmission cables. The study of self-field hysteresis losses of helicoidal superconductor structures has demonstrated that the shape of the twisted wire has influence on the qualitative loss behavior [Stenvall13]. Investigations of 3D helical superconductor *micro- and nanostructures* remain a challenge for both experiment and theory. The heuristic value of such studies is implied by the fact that nano- and microstructuring is one of the main avenues of the modern advancement of superconductor physics and technology, including superconducting electronics [Clark10], radiation modulators in the THz or sub-THz range [Savinov12], and superconducting qubits for quantum computing [Schoelkopf08].

The roll-up technique allows for combining curvature at the nanoscale with chirality by fabricating micro- and nanocoils [Zhang09, Smith11]. The present section provides quantitative analysis of the synergetic effects of curvature and chirality on vortex equilibrium distributions on self-rolled superconductor helical nanocoils.

We consider a helical coil of radius R, width W and pitch distance P with $N = 2$ windings shown in Fig. 2.16a. The centerline of this helical coil in the Cartesian coordinates X, Y, Z is

$$\mathbf{r}(\xi) = \left\{ R\cos\left(\frac{2\pi}{\ell}\xi\right), R\sin\left(\frac{2\pi}{\ell}\xi\right), \frac{P}{\ell}\xi \right\}, \tag{2.12}$$

where $\ell = \sqrt{(2\pi R)^2 + P^2}$ is the length of a single turn, the (longitudinal) coordinate along the helix $\xi \in [0,L]$, $L = N\sqrt{(2\pi R)^2 + P^2}$ is the total length of the centerline. The helix angle θ, as defined through the relations

$$\frac{2\pi R}{\ell} = \sin\theta, \ \frac{P}{\ell} = \cos\theta, \ \Rightarrow \theta = \tan^{-1}\left(\frac{2\pi R}{P}\right),$$

allows for the following representation of the centerline (2.9):

$$\mathbf{r} = \left\{\frac{\ell}{2\pi}\sin\theta\cos\left(\frac{2\pi}{\ell}\xi\right), \frac{\ell}{2\pi}\sin\theta\sin\left(\frac{2\pi}{\ell}\xi\right), \xi\cos\theta\right\}. \tag{2.13}$$

The unit tangential vector along the centerline is

$$\mathbf{t}(\xi,\eta) = \frac{\partial\mathbf{r}(\xi,\eta)}{\partial\xi} = \left\{-\sin\theta\sin\left(\frac{2\pi}{\ell}s\right), \sin\theta\cos\left(\frac{2\pi}{\ell}s\right), \cos\theta\right\},$$

the unit normal vector to the cylindrical surface is

$$\mathbf{n}(\xi,\eta) = \frac{\partial\mathbf{r}(,\eta)}{\partial R} = \left\{\cos\left(\frac{2\pi}{\ell}s\right), \sin\left(\frac{2\pi}{\ell}s\right), 0\right\},$$

and the unit binormal vector $\mathbf{b}(\xi,\eta) = \mathbf{n}(\xi,\eta)\times\mathbf{t}(\xi,\eta)$ is

$$\mathbf{b}(\xi,\eta) = \left\{\cos\theta\sin\left(\frac{2\pi}{\ell}s\right), -\cos\theta\cos\left(\frac{2\pi}{\ell}s\right), \sin\theta\right\}.$$

The unit vectors **t**, **n** and **b** are shown in Fig. 2.16a.

Under the assumption of a thin helical coil, the superconducting order parameter ψ is governed by the TDGL equation, which will be used in the dimensionless form (2.1), where $\mathbf{A} = -Bx\mathbf{e}_z$ is the vector-potential of the uniform magnetic field $\mathbf{B} = B\mathbf{e}_y$ (see Fig. 2.16a). It is complemented with the boundary conditions on the free boundaries (2.2a). The external normal to the boundary of the helical stripe coincides with [is opposite to] the binormal **b** on the boundary $(\xi, W/2)$ $[(\xi, -W/2)]$, for instance:

$$(\nabla - i\mathbf{A})\ \psi\cdot\mathbf{b}(\xi, \pm W/2)|_{\text{boundary}} = 0 \text{ at any } \xi. \tag{2.14}$$

It coincides with [is opposite to] the tangential vector **t** on the boundary (L,η) $[(0,\eta)]$, for instance,

$$(\nabla - i\mathbf{A})\ \psi\cdot\mathbf{t}(L \text{ or } 0,\eta)|_{\text{boundary}} = 0 \text{ at any } \eta. \tag{2.15}$$

An infinitesimally thin *helical stripe* of width W is a two-parametric surface represented by the radius vector

$$\mathbf{r}(\xi,\eta) = \left\{R\cos\left(\frac{2\pi}{\ell}s\right), R\sin\left(\frac{2\pi}{\ell}s\right), \xi\cos\theta + \eta\sin\theta\right\}, \ s = \xi - \eta\cot\theta, \tag{2.16}$$

where the (transverse) coordinate across the helix is $\eta \in [-W/2, W/2]$. The width of the helical stripe measured along the z-axis [see Fig. 2.16a] is

$$W_z = W/\sin\theta = W\ell/(2\pi R). \tag{2.17}$$

The condition of no overlap of the consequtive turns $P > W_z$ is represented in the form

$$P > P_{\text{overlap}} \text{ with } P_{\text{overlap}} = \left(\frac{1}{W^2} - \frac{1}{(2\pi R)^2}\right)^{-1/2}. \tag{2.18}$$

The $N_\xi \times N_\eta$ mesh for the finite-difference calculation is naturally parameterized as follows:

$$\begin{gathered} r_{ij} = r\left(\xi_i, \eta_j\right) = \left\{R\cos\left(\tfrac{2\pi}{\ell}s_{ij}\right), R\sin\left(\tfrac{2\pi}{\ell}s_{ij}\right), \xi_i\cos\theta + \eta_j\sin\theta\right\},\ s_{ij} = \xi_i - \\ \eta_j\cot\theta;\ \xi_i = \tfrac{i-1}{N_\xi - 1}L,\ i = 1, \ldots, N_\xi;\ \eta_j = \tfrac{j-1}{N_\eta - 1}W - \tfrac{W}{2},\ j = 1, \ldots, N_\eta. \end{gathered} \tag{2.19}$$

As demonstrated below, the natural orthogonal coordinates (ξ, η) form a particularly convenient basis for solving the TDGL equation on a helical stripe. In terms of the cylindrical coordinates

$$\varphi = \frac{2\pi s}{\ell},\ z = \xi\cos\theta + \eta\sin\theta, \tag{2.20}$$

the helical stripe is represented as a part of the cylindrical surface:

$$\mathbf{r}(\varphi, z) = \{R\cos(\varphi), R\sin(\varphi), z\}. \tag{2.21}$$

In the cylindrical coordinates, the shifted Laplace operator has the form

$$(\nabla - i\mathbf{A})^2 = \frac{1}{R^2}\frac{\partial^2}{\partial\varphi^2} + \left(\frac{\partial}{\partial z} - iA\right)^2. \tag{2.22}$$

The substitution of $s = \xi - \eta\cot\theta$ into eq. (2.20) leads to the transformation of coordinates

$$R\varphi = (\xi\sin\theta - \eta\cos\theta),\ z = \xi\cos\theta + \eta\sin\theta. \tag{2.23a}$$

An inverse transformation can be interpreted as a rotation of the cylindrical coordinates by the helix angle:

$$\xi = R\varphi\sin\theta + z\cos\theta,\ \eta = -R\varphi\cos\theta + z\sin\theta. \tag{2.23b}$$

The coordinate axes (ξ, η) are represented in Fig. 2.16a. Under the rotation of eq. (2.23b), the shifted Laplace operator of eq. (2.22) transforms as follows:

$$(\nabla - i\mathbf{A})^2 = \frac{\partial^2}{\partial\xi^2} + \frac{\partial^2}{\partial\eta^2} - 2iA\left(\frac{\partial}{\partial\xi}\cos\theta + \frac{\partial}{\partial\eta}\sin\theta\right) - A^2. \tag{2.24}$$

It is represented in a compact form using the longitudinal and transverse components of the vector potential

$$A\cos\theta = A_\xi \quad \text{and} \quad A\sin\theta = A_\eta,$$

correspondingly:

$$(\nabla - i\mathbf{A})^2 = \left(\frac{\partial}{\partial\xi} - iA_\xi\right)^2 + \left(\frac{\partial}{\partial\eta} - iA_\eta\right)^2. \tag{2.25}$$

In terms of the longitudinal and transverse components of the vector potential, the boundary conditions on two pairs of boundaries are *explicitly independent* from each other:

$$\left(\frac{\partial}{\partial\eta} - iA_\eta\right)\psi(\xi, \pm W/2)|_{\text{boundary}} = 0 \text{ at any } \xi; \tag{2.26a}$$

$$\left(\frac{\partial}{\partial\xi} - iA_\xi\right)\psi(L \text{ or } 0, \eta)|_{\text{boundary}} = 0 \text{ at any } \eta. \tag{2.26b}$$

This property of the boundary conditions makes the coordinates introduced by the eq. (2.23b) particularly useful for solving the TDGL equation on a helical stripe.

The stationary vortex distributions in a helical stripe emerge as a result of strongly inhomogeneous normal magnetic field, whose pattern, shown in Fig. 2.17a in the coordinates (ξ, η), depends on the geometrical characteristics of the helical stripe. The normal component is maximal ($B_n = B$) in the areas, where the unit normal vector $\mathbf{n}(\xi, \eta)$ is parallel or close to the direction of the applied magnetic field $\mathbf{e}_y$ (red in Fig. 2.16b), and minimal ($B_n = -B$) in the areas, where the normal vector is antiparallel or close to the direction opposite to the applied magnetic field (blue in Fig. 2.16c). The above areas are favorable for the occurrence of vortices (compare with Section 2.1).

Calculation of the order parameter is performed using the finite-difference scheme (see [Fomin09], where it was developed for planar nanostructured superconductors) for the TDGL eq. (2.1) with the boundary conditions (2.14), (2.15) realized on the orthogonal mesh (see eq. (B4) in [Fomin17]). The materials parameters for nanostructured Nb at the relative temperature $T/T_c = 0.95$ are the same as in the previous sections: the coherence length $\xi = 56$ nm, the penetration depth $\lambda = 279$ nm, the Ginzburg–Landau parameter $\kappa = 5$, the diffusion coefficient $D = 11.2 \times 10^{-4}$ m^{2}s^{-1} [Fomin12a]. The initial distribution of the complex order parameter is taken as a random complex field. An ultrasmall stochastic potential is added to the shifted Laplace operator in eq. (2.1), in order to

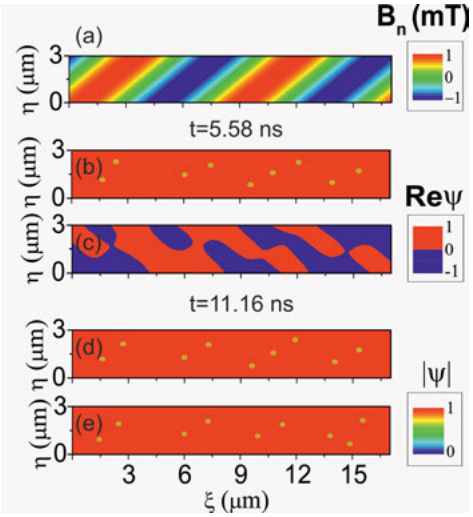

Fig. 2.17: (a) Distribution of the normal component of the magnetic field $B_n = \mathbf{B} \cdot \mathbf{n}(\xi, \eta)$ in a helical coil with parameters: $R = 0.96$ μm, $W = 3$ μm, $P = 6$ μm, $L = 2\ell = 17.02$ μm. The applied uniform magnetic field is $B = 1$ mT. (b, d, e) Distribution of the modulus of the order parameter $|\psi|$ in the helical coil calculated using the orthogonal mesh with $N_\xi = 481$ and $N_\eta = 241$. (c) Distribution of the real part of the order parameter Reψ. Data in panels (b) and (c) are obtained at $t = 5.58$ ns, while those in (d) and (e) are obtained at $t = 116$ ns. A stochastic potential, which enables transitions of the vortex system between patterns with close or equal energies (see Appendix D in [Fomin17] for details), has a higher magnitude in (e), than in (d) (from [Fomin17]).

allow for transitions of the vortex system between different configurations with close or equal energies and to facilitate the evolution of the order parameter to a state with a minimal free energy (see [Fomin17]). The evolution of the order parameter is traced toward a stationary state. As illustrated in Fig 2.17b, d, the stationary distribution of the order parameter contains single vortices or vortex chains aligned along the lines of the maximal or minimal normal component of the magnetic field (compare Fig. 2.17b, d with a). The fact that the lines of the 2π-phase shift of the order parameter (Fig. 2.17c)

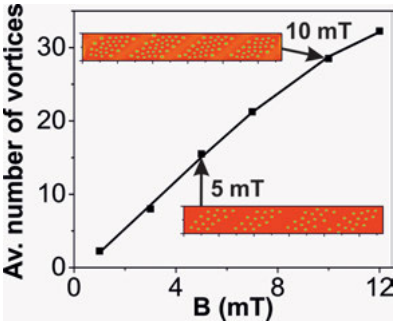

Fig. 2.18: Average number of vortices per half-turn as a function of the applied uniform magnetic field for a helical coil with the same geometrical parameters as those in Fig. 2.17. In insets, distributions of the order parameter are shown for $B = 5$ mT and 10 mT. The color scale is the same as in Fig. 2.17b. Data are obtained at $t = 5.58$ ns (in Figs. 2.18 to 2.22, the calculated data are represented with squares, while solid lines are guides to the eye) (from [Fomin17]).

go through dips of the modulus of the order parameter (Fig. 2.17b) evidences that those dips represent *superconducting vortices*.

Given the magnetic field, the pattern and number of vortices are determined by their confinement to the helical coil. The boundary conditions (2.15) are specific for the helical stripe and provide a major distinction from the case of an open cylinder [Fomin12a]. Qualitatively, a certain distribution of vortices on the surface of a cylinder is established due to the vortex–vortex interaction under the condition that screening currents flow close to the boundaries of the upper and the lower halves of the cylinder with respect to the direction of the applied magnetic field. In open superconductor tubes, SSCs flow in each half of *the whole cylinder* as shown in Fig. 2.1b. As distinct from that, in the helical coil those currents flow in each *half-turn* (as shown schematically in Fig. 2.16d,e), and therefore the confinement of vortices to the helical stripe affects the vortex pattern formation through a *longer boundary* than that in a cylinder of the same radius and comparable overall height.

The different numbers of vortices occurring in different half-turns (for example, two and three at $B = 1$ mT) are attributed to the adjustment of the vortex matter to such a magnetic field, which requires a number of vortices, which is *incommensurable* with (in other words, is not an integer multiple of) the total number of half-turns. In the course of evolution, alternative patterns of vortices distributed over half-turns may occur. At $B = 1$ mT, there are different configurations of nine vortices with three vortices in different half-turns, shown, for instance, in Fig. 2.17d,e. This is a manifestation of a *quasidegeneracy* of vortex patterns in a helical stripe. Henceforth, we describe the vortex distributions by the *average* number of vortices per half-turn.

A quantitative analysis of the vortex patterns in helical coils for different magnetic fields and geometrical parameters of a helical coil is represented in what follows. When increasing the magnetic field, the pattern of the vortex distribution changes from single linear chains aligned along the lines of the maximal or minimal values of B_n (see the case $B = 1$ mT in Fig. 2.17b, d) toward a few parallel chains represented in Fig. 2.18 (see the cases $B = 5$ and 10 mT). These vortex chains are concentrated in the areas of the maximal or minimal values of B_n, as sketched in Fig. 2.16b, c. This pattern of ordering emerges as a result of the interplay between the vortex confinement to the abovementioned areas in helical stripes and the vortex–vortex interaction.

The study of the impact of geometry on the distribution of vortices begins with a sparse helical coil, when the pitch distance appreciably exceeds the value $P_{overlap}$, so that there is a significant distance between neighboring turns. The average number of vortices per half-turn increases with W, as illustrated in Fig. 2.19. At a low magnetic field $B = 1$ mT, the average number of vortices per half-turn with increasing helical stripe width is a slow function of W due to the developing screening currents. With rising magnetic field up to $B = 5$ mT, the increase becomes faster due to developing multiple chain patterns. At even higher magnetic fields ($B > 5$ mT), the dependence approaches a linear function, which reflects the geometrical origin of the effect: in a sparse helical spiral with a fixed pitch distance, the magnetic flux through the helical stripe in a fixed

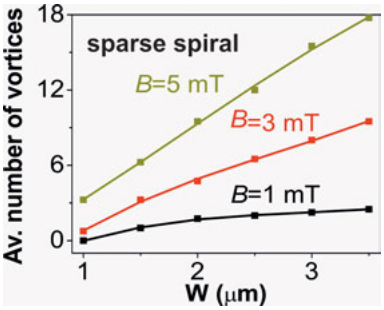

Fig. 2.19: Average number of vortices per half-turn as a function of the helical stripe width for a sparse spiral at $P = 6$ μm placed in a fixed magnetic field ($B = 1$, 3 and 5 mT). Data are obtained at $t = 5.58$ ns (from [Fomin17]).

magnetic field rises directly proportional to its width. The vortices occur even in sparse helical coils with rather narrow stripes ($W \sim 1$ μm), because the effective width of a stripe along the helical coil axis W_z [see eq. (B2) in [Fomin17]] increases with P.

Next, a dense helical coil is considered, when the pitch distance P slightly exceeds the value P_{overlap} [see eq. (2.18)], at which the subsequent turns start to overlap. In this case, the neighboring turns are close to (almost touching) each other. The distribution of vortices occurs to be very sensitive to the helical stripe width W. In Fig. 2.20, the average numbers of vortices per half-turn in dense helical spirals are represented as a function of the helical stripe width W. The increase of the average number of vortices per half-turn with increasing width W occurs faster than the linear dimension (of the order of $W_z \approx W$) of the areas with the maximal/minimal values of B_n. This nonlinear behavior can be again attributed to developing multichain patterns, as shown in the insets to Fig. 2.18.

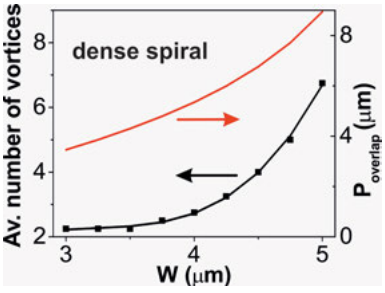

Fig. 2.20: Average number of vortices per half-turn as a function of the helical stripe width for a dense helical coil. At any value of W, the pitch distance slightly exceeds the value P_{overlap} (also plotted). Data are obtained at $t = 5.58$ ns. The applied uniform magnetic field is $B = 1$ mT (from [Fomin17]).

The increase of the average number of vortices with the pitch distance depends on the applied magnetic field. For single-chain patterns at weaker fields, as shown in Fig. 2.21 for $B = 1$ mT, the increase is slow presumably because of an appreciable impeding of the vortex nucleation due to the boundary conditions at the helical stripe edges. For multichain patterns at stronger fields, the increase of the average number of vortices per half-turn occurs faster than the linear dimension ($\sim W_z$) of the areas with the maximal/minimal values of B_n. This behavior may be attributed to the following *combination of geometrical and physical factors*: with increasing W_z, not only the magnetic flux

penetrating the helical stripe increases, but impeding of the vortex nucleation due to the boundary conditions at the helical stripe edges becomes relatively weaker. A stepwise increase of the average number of vortices as a function of the pitch distance in Fig. 2.21 reflects the geometric fact that in the helical coil with two turns, vortex nucleation or denucleation changes the average number of vortices per half-turn by 0.25 or −0.25. In helical coils with a larger number N of turns, the magnitude of the smallest change of the average number of vortices decreases as $1/(2N)$.

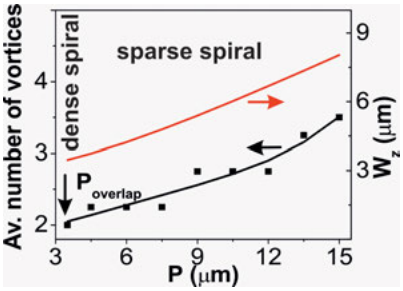

Fig. 2.21: Average number of vortices per half-turn as a function of the pitch distance at the helical stripe width $W = 3$ μm. The effective width of a stripe along the helical coil axis W_z is also plotted. The applied uniform magnetic field is $B = 1$ mT. Data are obtained at $t = 16.74$ ns (from [Fomin17]).

The average number of vortices per half-turn increases with the radius, as shown in Fig. 2.22. With rising magnetic field from $B = 1$ mT to $B = 5$ mT, the increase becomes faster due to developing of larger multichain fragments. This occurs because of the following geometric factor. When increasing the radius R at fixed values of the helical stripe width $W = 3$ μm and the pitch distance $P = 6$ μm, the areas with maximal [minimal] value of the normal component of the magnetic field $B_n = B$ [$B_n = -B$] [marked with red in Fig. 2.16d (blue in Fig. 2.16e)] expand proportionally to the increasing length of the stripe along the centerline L. The insets to Fig. 2.22 represent vortex patterns

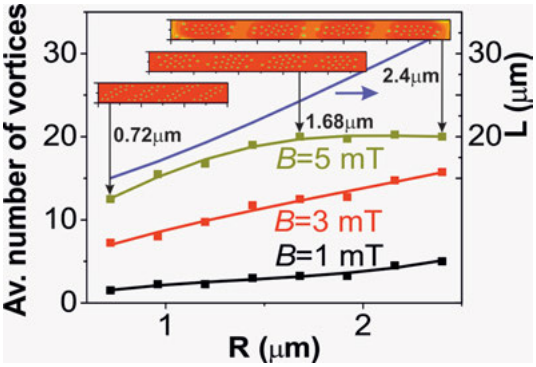

Fig. 2.22: Average number of vortices per half-turn as a function of the radius at the helical stripe width $W = 3$ μm and the pitch distance $P = 6$ μm for different values of the applied uniform magnetic field ($B = 1$, 3 and 5 mT). Data are obtained at $t = 16.74$ ns. The length of the stripe along the centerline L is also plotted. Distributions of the order parameter are shown in the insets for $R = 0.72$, 1.68 and 2.4 μm (from [Fomin17]).

at $B = 5$ mT for radii $R = 0.72$, 1.68 and 2.4 μm. For a smaller radius ($R = 0.72$ μm), vortex chains are arranged parallel to the lines, where the normal component of the magnetic field has its maximal [minimal] value of $B_n = B$ [$B_n = -B$]. With increasing radius, the average number of vortices per half-turn rises more prominently at higher magnetic field values, similarly to Fig. 2.18. At $B = 1$ mT and 3 mT, this behavior is manifested over the whole interval of the considered radii. However, at still higher magnetic fields, for example, $B = 5$ mT, the average number of vortices per half-turn as a function of radius saturates. This trend of vortex pattern in each of the upper and lower areas of the helical stripe reflects a behavior similar to that in a planar stripe perpendicular to an applied magnetic field, corresponding to the limit of negligible curvature. The multivortex pattern acquires the shape of vortex chains parallel to the sides of the helical stripe (inset for $R = 2.4$ μm). This may be attributed to stronger screening currents, which effectively repel vortices from the sides of the stripe in helical coils of a larger radius. At intermediate radii, an interplay of both trends of vortex ordering is observed: (i) parallel to the lines, where the normal component of the magnetic field has its maximal [minimal] value, which is typical of an open tube [Fomin12a], and (ii) parallel to the sides of the helical stripe, specific for a planar stripe [Tinkham96]. The interplay leads to a mixed pattern even with some signs of a hexagonal order (inset for $R = 1.68$ μm).

The pattern and number of vortices in a stationary distribution are determined by their confinement to the helical coil. For a dense helical coil, as well as for a sparse one at lower magnetic fields, the increase of the average number of vortices with increasing the stripe width occurs faster than the growth in the linear dimension of the areas with extremal values of the normal component of the magnetic field. This behavior can be presumably attributed to the trend of changing the vortex ordering patterns from one to a few chains of vortices. For a sparse helical coil at higher magnetic fields, the average number of vortices appears to be a linear function of the stripe width, which reflects the geometrical origin of the effect. The increase of the average vortex number with increasing pitch distance occurs faster than the growth in the linear dimension of the areas, where the normal component of the magnetic field has its extremal values, due to an interplay of geometrical and physical factors. The revealed quasidegeneracy of the vortex patterns generates very interesting dynamics of vortices in helical coils. Superconducting helical coils of increasing radius provide a physical realization of a transition from the vortex pattern of an open tube to that of a planar stripe. The revealed excellent tunability of the superconducting vortex patterns makes micro- and nanohelices highly promising for application in superconducting electronics and superconducting qubits. Innovative schemes have taken advantage of the third dimension for the development of high-performance and highly energy-efficient electronic components [Shulaker17]. Thus, 3D nanosuperconductivity could represent a breakthrough for future electronics components, particularly for sensors, energy-storage components and quantum computing. A significant improvement of the microwave radiation detection has been demonstrated through the fabrication of a superconducting bolometer by self-rolling 2D superconductor structures into 3D helical belts [Lösch19].

Novel schemes based on the design of complex 3D nanoscale architectures are required for the development of the next generation of advanced electronic components. He^+ FIB-microscopy in combination with a precursor gas allows one to fabricate 3D nanostructures with an extreme resolution, and a considerably higher aspect ratio than other FIB-based methods, such as Ga^+ FIB-induced deposition, or other additive manufacturing technologies. The fabrication of 3D tungsten carbide (WC) nanohelices with on-demand geometries via controlling key deposition parameters [Cordoba19] has led to the ultra small and densely packed nanohelices, with dimensions of 100 nm in diameter, and aspect ratio up to 65. These nanohelices become superconducting at 7 K and show large critical magnetic field and critical current density [Cordoba19]. The fingerprints of vortex and phase-slip patterns are revealed from the experimental data using numerical simulations based on the TDGL equation, given the 3D helical geometry of nanostructures [Cordoba19].

An interesting feature only visible in the measured resistance–current characteristics (RCCs) for the nanohelix of one type is that the resistive transition occurs in various steps, as observed in measurements under fixed perpendicular magnetic field of 1 and 2 T (see Fig. 2.23). Nanohelices of other types do not show this feature. In order to provide some insight to this behavior, numerical simulations based on the TDGL equation coupled with Poisson equation have been performed using the Link-Variables approach by finite-difference time-domain method.

The TDGL equation (2.10) is solved with the boundary conditions that follow from the vanishing of the normal component of the superconducting current at the free edges:

$$\mathbf{n}\cdot\left(\frac{1}{i\kappa}\nabla-\mathbf{A}\right)\psi|_{\partial D_s}=0;\ \mathbf{n}\cdot\left(\frac{1}{i\kappa}\nabla-\mathbf{A}\right)\psi|_{\partial D_y}=0. \tag{2.27a}$$

The electric potential φ is found as a solution of the Poisson eq. (2.11) coupled with eqs. (2.10) and (2.27). The transport current density $j_{\mathrm{tr}}(y)=\mathrm{const}\equiv j_{\mathrm{tr}}$ is imposed via the boundary conditions for eq. (2.11) at the edges, to which electrodes are attached:

$$\mathbf{n}\cdot\nabla\varphi|_{\partial D_s}=-\frac{1}{\sigma}j_{\mathrm{tr}};\ \mathbf{n}\cdot\nabla\varphi|_{\partial D_y}=0. \tag{2.27b}$$

Parameters in the aforementioned equations used for numerical simulation are presented in Tables 2.3 and 2.4. The parameters provided in Table 2.3 are calculated for the temperature $T=0.5$ K using the following expressions in the dirty limit [Esposito14]:

$$\xi=0.855\sqrt{\frac{\xi_0 l}{1-t}},\ t=\frac{T}{T_c},\ \lambda=\lambda_0\sqrt{\frac{\xi_0}{2(1-t)\cdot 1.33l}},$$

$$D=\frac{lv_F}{3},\ \tau_{\mathrm{GL}}=\frac{\xi^2}{D},\ B_{c2}=\frac{\Phi_0}{2\pi\xi^2},$$

$$j_c^{\mathrm{calc,G}} = \frac{cH_c}{3\sqrt{6}\pi\lambda}\ \text{(Gaussian units)},\ j_c^{\mathrm{calc,SI}} = k_{\mathrm{G}\to\mathrm{SI}}\, j_c^{\mathrm{calc,G}},\ k_{\mathrm{G}\to\mathrm{SI}} = \frac{1}{3\times 10^5}\ \text{(by value)},$$

$$H_c = \frac{H_{c2}}{\sqrt{2}\kappa},\ \kappa = \frac{\lambda}{\xi}.$$

For the numerical simulation, the 2D approximation is used with the mesh with $1{,}725 \times 25$ nodes that provides the spatial resolution as small as 0.5ξ. The discretization time is equal to $0.0005\tau_{\mathrm{GL}}$; however, this parameter is *dynamically adapted* to the dynamics of the system: when there occurrs only a small variation of the order parameter (phase and amplitude), the time discretization is increased and vice versa. With these parameters, the model is capable to reproduce the vortex dynamics in the presence of a transport current and a magnetic field. The number of iterations required to reach the specific order parameter pattern varies between 10^7 and 10^8.

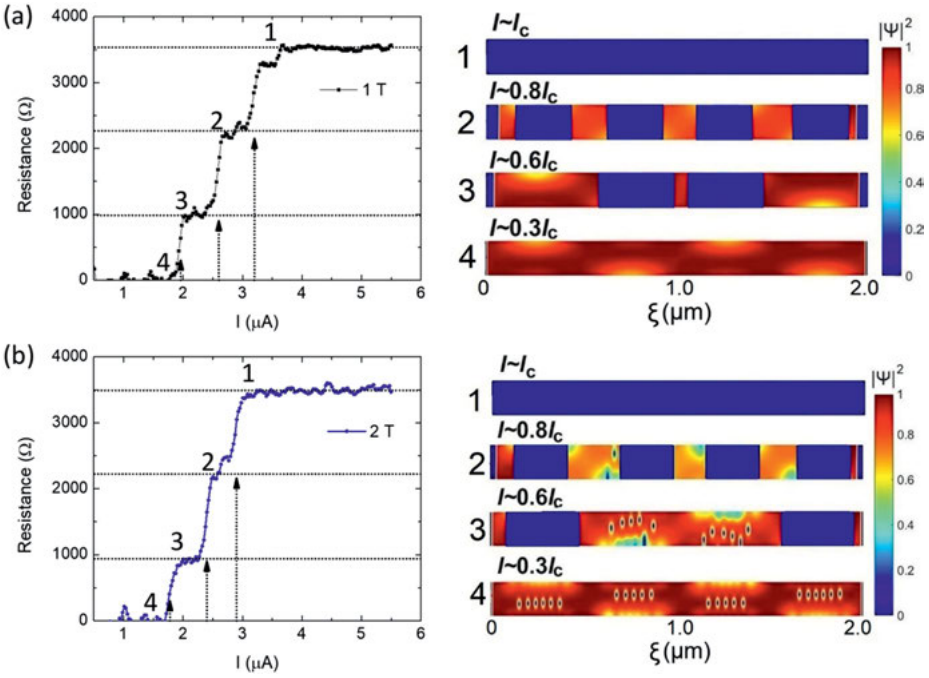

Fig. 2.23: Experimental RCCs (left panels) for the nanohelix type 6, and simulated order-parameter distributions plotted over the 2D surface of the helical structure (right panels) for the magnetic fields 1 T (upper-right panel) and 2 T (lower-right panel). The values of the applied transport current in units of the critical current are indicated in the panels. The critical currents are evaluated from the experimental data to be 3.3 μA for 1 T and 3.0 μA for 2 T. Different vortex and phase-slip patterns correspond to steps of resistance (the correspondence is shown by the arrows) (from [Cordoba19]).

Table 2.3: Calculated and evaluated parameters for the nanohelix type 6 (from [Cordoba19]).

Physical parameter and units	Value
Coherence length ξ, nm	5.4
Magnetic field penetration depth λ, nm	345.0
Diffusion coefficient D, m^2/s	8.5×10^{-6}
Second critical magnetic field B_{c2}, T	11.5
Critical current I_c, μA (for magnetic field 1 T)	3.3 (evaluated from the experimental data: the value at which the maximal resistance is reached)
Critical current I_c, μA (for magnetic field 2 T)	3.0 (evaluated from the experimental data: the value at which the maximal resistance is reached)
Relaxation time τ_{GL}, ps	3.4

Table 2.4: Parameters taken for the particular simulation of the nanohelix type 6 in the 2D approximation (from [Cordoba19]).

Geometrical and physical parameters and units	Value
Number of turns	2
Radius of the helical coil R, nm	138.5
Width W, nm	58
Coherence length ξ_0, nm	4.93 (averaged over all structures)
Magnetic field penetration depth λ_0, nm	665 (averaged over all structures)
Conductivity in the normal state σ, $1/\Omega \cdot m$	4.75×10^5 (extracted from the experimental data and averaged over all structures)
Critical temperatures T_c, K	6.63 (averaged over all structures)
Mean free electron path ℓ, nm	7.45 (evaluated from experimental data)
Fermi velocity v_F, m/s	3,419 (calculated from the Drude model)

This analysis reveals several patterns of the order parameter corresponding to the spatial distribution of the normal to the surface component of the magnetic field over the surface of the helical nanostructure. These patterns are represented in the right panels of Fig. 2.23a and b for magnetic fields 1 and 2 T, respectively. The order-parameter distribution over the surface of the helical structure is shown at different values of the applied transport current (in units of the critical current). The voltage generated by an individual vortex in motion for all patterns leads to a finite resistance of the order of 1 Ω. Experimentally observed jumps (higher than

100 Ω) in the RCCs are about two orders of magnitude higher than the resistance induced by an individual vortex, which follows from the numerical simulation. The most probable reason for the observed jumps is therefore the occurrence of phase slips, which start to appear at transport current values shown in Fig. 2.23. The transition of two half-turns into the full phase-slip regime causes the resistance to increase by about 1,000 Ω, whereas the presence of the phase slips in all half-turns without the vortex dynamics results in a resistance of about 2,250 Ω. The simulated order parameter at the magnetic field $B = 1$ T shown in Fig. 2.23a does not seem to reveal vortices in static or dynamic states.

From an arbitrary initial state (for which a random distribution is taken), the order parameter evolves to one of the three following quasistationary patterns: (i) pure vortex state (the number of vortices is in the range from 0 to N), (ii) mixed one: vortices plus order-parameter depression regions (phase slips) and (iii) pure order-parameter depression regimes. It is suggested that the whole half-turn, at which the order-parameter depression appears, switches to the normal state due to the Joule heating as shown in Fig. 2.24. In regions, where the absolute value of the normal to surface magnetic field is minimal, the order-parameter depression extent is suppressed. This mechanism explains the experimental shelf-like features in RCCs [Cordoba19]. As distinct from the planar 2D superconductor structures, the complex 3D geometry of nanohelices determines topologically nontrivial SSCs and confinement potentials that cardinally depend on radius and pitch (or, equivalently, curvature and torsion) and imply, as shown below, occurrence of different patterns of topological defects.

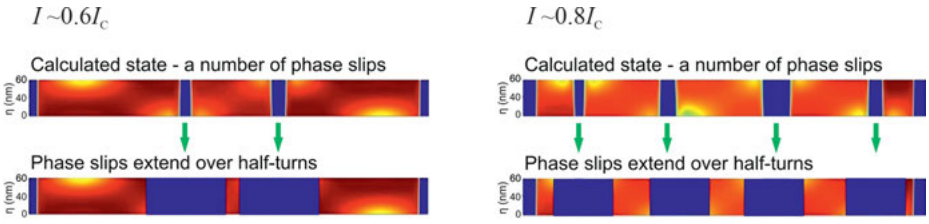

Fig. 2.24: Simulated order-parameter distributions plotted over the 2D surface of the helical structure (experimental type 6) for 1 T. Each calculated state manifesting a number of phase slips in some half-turns (top panels) and the assumed phase-slips extension over the half-turns (bottom panels). The values of the applied transport current in units of the critical current are indicated in the panels (from [Cordoba19]).

For all structures, a similar behavior is manifested, when the applied current increases from 0 to the critical value. Namely, the modulus of the order parameter evolves from a homogeneous state, which describes the pure superconducting phase, to different patterns of vortices, then to different phase-slip patterns, finally resulting in the normal

state. In order to check how phase-slip patterns evolve with increasing number of turns, a simulation is performed for structures with fixed width (50 nm), helical diameter (100 nm), and pitch (200 nm) under a magnetic field of 2 T. These geometrical characteristics of the simulated structures correspond to the experimental helix type 1. Results of this simulation for a fixed applied transport current ($I \sim 0.6I_c$) are shown in Fig. 2.25. For the structure with one turn, phase slips are represented by three extended regions over the half-turns. Phase slips occupy approximately 80% of the area of the structure. For the structure with two turns, there are five regions with phase slips, while the relative size of each phase-slip region is smaller than the relative size of a phase-slip region for the structure with one turn. The trend of decreasing the size of the phase-slip regions and increasing their number continues for the structure with three turns. For the structure with four turns, the phase-slip regions disappear in some parts of the structure. The increment of the resistance is proportional to the overall size of the phase-slip regions, so, when the phase-slip pattern is represented by a number of small regions, each new region gives a small increment to the resistance (the case realized in the experimental helix types 1, 4, 7). In this case, there occur no shelf-like features in the RCCs within the experimental conditions.

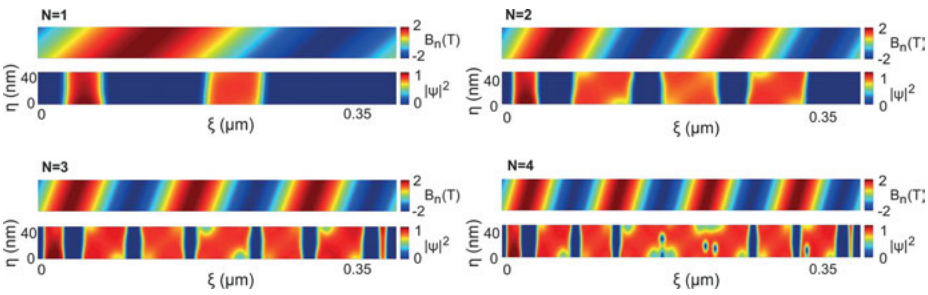

Fig. 2.25: The magnetic field and the order-parameter distributions for the nanohelix (experimental type 1) with the width $W = 50$ nm, the helical radius $R = 50$ nm, the pitch $P = 200$ nm and the number of turns $N = 1$, $N = 2$, $N = 3$ and $N = 4$. The transport current $I \sim 0.6I_c$ (from [Cordoba19]).

Extensive simulations performed for structures of different helical radii (from 50 to 150 nm) and pitches (from 200 to 925 nm) under various applied transport currents (from 0 to $1.2I_c$) reveal no qualitative difference in order-parameter patterns as a function of the applied transport current. To confirm the above-discussed impact of topology on the order parameter, the planar structures are simulated with the same dimensions as the helical ones. For each number of turns, the order parameter is provided for the corresponding planar structure (Fig. 2.26). It is remarkable that for all planar structures, the order-parameter pattern does not depend on the size, unlike that in helical structures (Fig. 2.25).

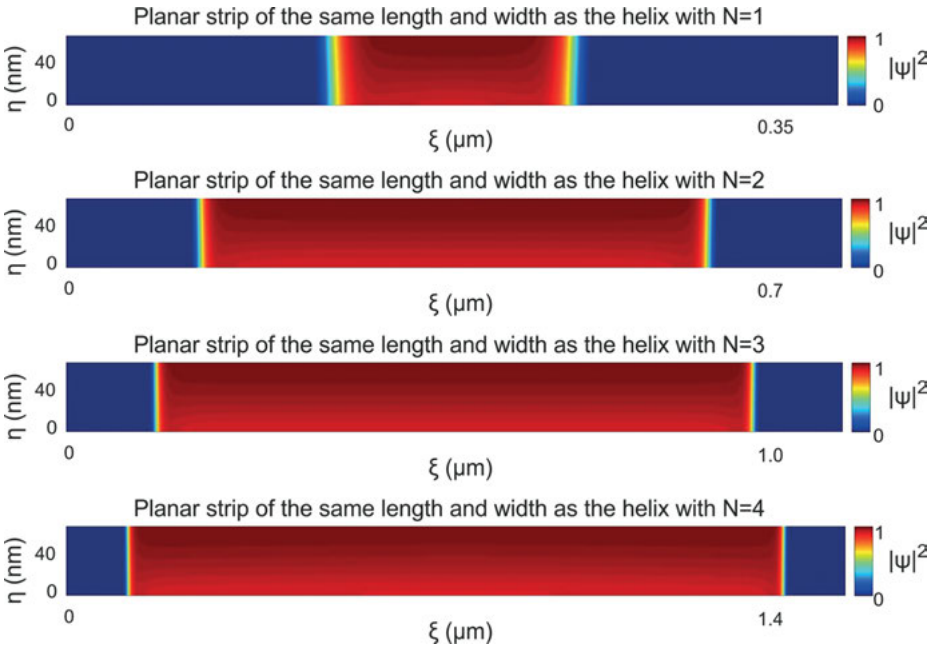

Fig. 2.26: The order-parameter distributions for planar structures of the width $W = 50$ nm and different lengths corresponding to the nanohelices with the numbers of turns $N = 1, 2, 3, 4$. The transport current $I \sim 0.6I_c$ (from [Cordoba19]).

In Fig. 2.27, the evolution of the order parameter with increasing transport current is illustrated for the nanohelix with two turns and for the corresponding planar structure. The spatial regions occupied by the normal phase of the order parameter in a planar structure approximately linearly grow with the current, while the similar spatial regions in the helical structure remain almost unchanged. This comparison qualitatively demonstrates how the helical geometry changes the resistive properties of self-rolled nanoarchitectures.

Figures 2.25 to 2.27 demonstrate how chirality of nanohelices determines the order-parameter patterns that are quite distinct from those in planar structures and thus provide an insight into the occurrence of the shelf-like features in the RCCs in some nanohelices, while there are no such features in other nanohelices. The same mechanism seems to be responsible for the step-like CVCs detected in the much larger microhelical belts [Lösch19].

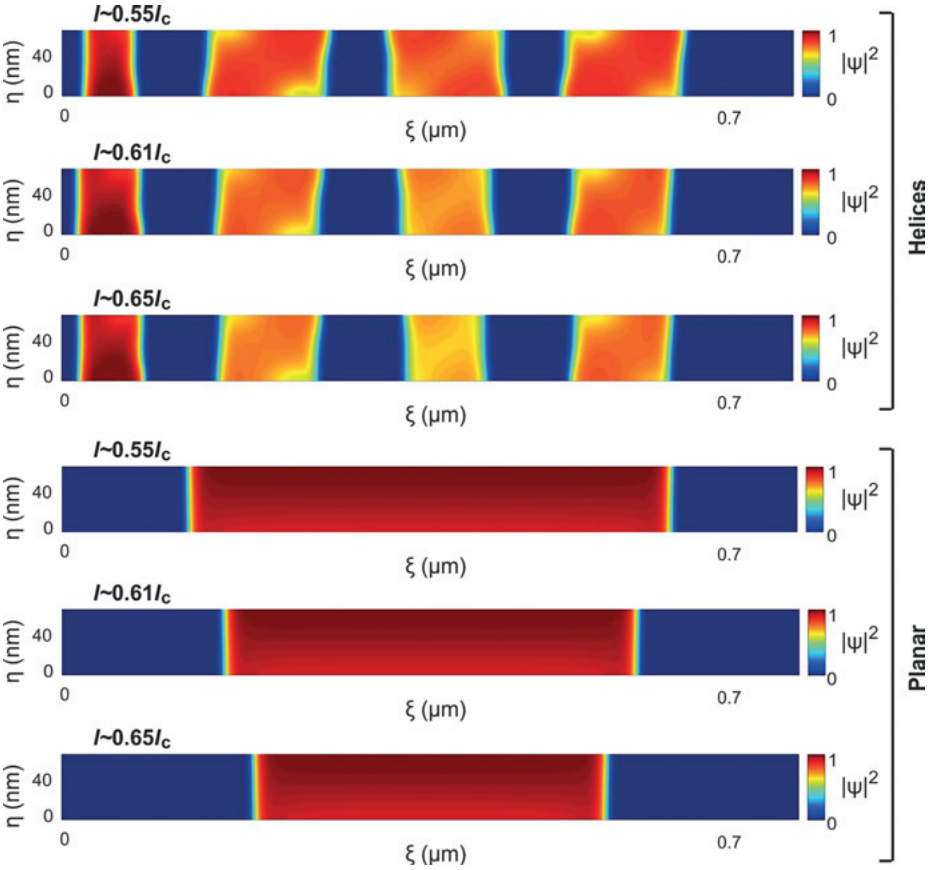

Fig. 2.27: The order-parameter distributions (panels 1–3) for the nanohelix (experimental type 1) with the $W = 50$ nm, $R = 50$ nm, pitch $P = 200$ nm and the number of turns $N = 2$. The three bottom panels (4–6) show the order-parameter distributions for the planar structures of the same dimensions. The values of the applied transport current in units of the critical current are indicated in the panels (from [Cordoba19]).

3 Theory of phonons in advanced semiconductor micro- and nanoarchitectures for thermoelectric applications

Efficient nanoscale control of acoustic phonons is of immanent importance for design and fabrication of novel nanoelectronic systems, nano- and optomechanical devices, micro- and nanoscale resonators, phonon-based quantum memories and biomedical applications, thermoelectric materials. Spatial confinement of acoustic phonons in semiconductor thin films, superlattices and nanowires changes their properties in comparison with bulk materials. Phonon confinement in nanostructures leads to emergence of the quantized energy subbands with corresponding modification of the phonon density of states (DOS). Nanostructuring, as suggested in ref. [Hicks93], creates a timely opportunity to search for new advanced thermoelectric materials (see [Dresselhaus07, Balandin12, Fomin18c] for reviews). A combined "roll-up press-back" technology has been presented to fabricate novel acoustic metamaterials/mechanically joined nanomembrane superlattices [Grimm14], which reveal a significant reduction of the measured cross-sectional phonon transport compared to a single nanomembrane layer [Li17].

It has been demonstrated theoretically that phonon heat flux can be significantly suppressed in Si and Si/SiO_2 nanowires with the periodically modulated cross section area (MNWs) [Nika12, Cocemasov15]. Redistribution of the phonon energy spectra in MNWs leads to a strong decrease of the average phonon group velocities and hence to a suppression of the phonon thermal flux in these nanowires as compared to the generic nanowires. This effect is explained by the exclusion of the phonon modes trapped in MNW segments from the heat flow.

Efficient engineering of the acoustic phonon energy spectrum has been achieved in self-rolled multishell tubular structures. The acoustic phonon dispersion is determined by solving the equations of elastodynamics for InAs and GaAs material systems. It is shown that the number of shells is an important control parameter of the phonon dispersion together with the structure dimensions and acoustic impedance mismatch between the superlattice layers. Analysis of phonon spectra in multishell nanostructured microtubes [Fomin15, Fomin18c] has revealed the fact that the number of shells is an important control parameter of the phonon dispersion, which implies a prominent effect on the group velocity dispersion and the phonon DOS as well as on the phonon transport. The obtained results suggest that self-rolled nanoarchitectures are promising for thermoelectric applications owing to a possibility of significant reduction of the thermal conductivity without degradation of the electronic transport.

For the radial Si/SiO_x hybrid nanomembrane superlattices (HNMSLs) [Li17], the in-plane thermal conductivity of a one-winding Si tube shows a tremendous reduction

https://doi.org/10.1515/9783110575576-003

compared to both the bulk Si material and other Si thin-film systems with the same thickness. Interestingly, as the number of windings of Si tubes increases, the in-plane thermal conductivity drops owing to the thermal interaction among various windings. The theoretical simulation fits the experimental data very well and implies that the thermal conductivity of the fabricated Si/SiO_x HNMSLs is strongly affected by the phonon processes in the amorphous SiO_x layers. The obtained thermal properties together with the unique roll-up and compression technique pave a novel way for Si-based thermoelectric applications.

The optical phonon spectra in multilayer cylindrical quantum wires manifest a geometric structural effect [Klimin94], which is of immanent importance for understanding of the pairing of charge carries in quantum wires [Pokatilov00], as well as the electron–phonon phenomena in multilayer coaxial cylindrical $Al_xG_{1-x}As$/GaAs quantum cables [Zhang03] and double-coupled nanoshell systems [Kanyinda08]. The aim of the present section is to demonstrate the feasibility of controlling the acoustic phonon energy spectra and corresponding phonon velocity dispersion in self-rolled micro- and nanoarchitectures. Of fundamental importance in this context is the experimental evidence [Deneke07] that due to oxide formation during fabrication, a single period of a radial superlattice is represented by a semiconductor/amorphous oxide/polycrystalline metal/amorphous oxide layer rather than a semiconductor/metal layer. This implies a necessity to investigate multilayer tubes. The elastodynamic boundary conditions on spiral interfaces of a self-rolled microtube with multiple windings or on cylindrical interfaces of a multilayer tube, which consists of coaxial cylindrical shells, (multishell) immediately affect the acoustic phonon energy spectrum and, hence, phonon group velocities for propagation along the tube. Since the effect of these boundary conditions depends on the number of shells along with the geometric parameters, multishells are qualified into acoustic metamaterials. This introduces, in particular, extra capability for tuning the phonon spectrum, engineering the phonon transport and advancement of thermoelectric materials [Balandin12].

3.1 Phonon spectra in multishell microtubes

Spiral interfaces of a self-rolled microtube with multiple windings (Fig. 3.1a,b) are modeled by cylindrical interfaces of a multishell as shown schematically in Fig. 3.1c. The elastic continuum model is used because it works well for the considered dimensions of the structures. It was shown previously that such a model gives results in good agreement with the lattice dynamics and molecular dynamics (MD) simulations [Nika09, Hu11b, Bi12, He12]. The acoustic phonon modes near the Brillouin zone (BZ) center are primarily responsible for heat transfer. The elastic continuum model is particularly accurate for the BZ center phonons. Infinitely long structures can be

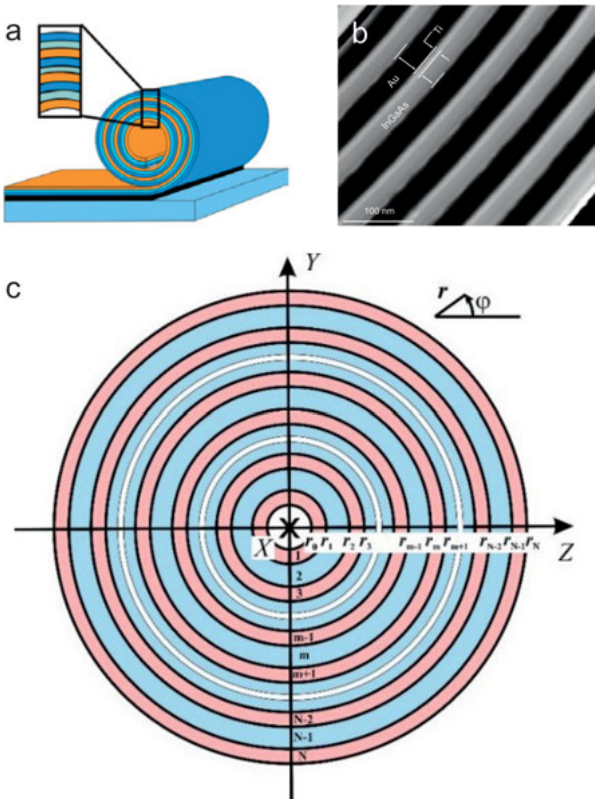

Fig. 3.1: Microtube with multiple windings fabricated using roll-up technology, a scheme (a) and a STEM image of a radial superlattice from a self-rolled 20 nm InGaAs/10 nm Ti/46 nm Au layer (b) (republished with permission of IOP Publishing from ref. [Deneke09] © (2009) IOP Publishing.). Cross section in the plane orthogonal to the *X*-axis of a multilayer tube consisting of coaxial shells (multishell) (c). The tube core and the outer medium are vacuum. The axis of the structure is selected as the *X*-axis. The polar coordinates in the *YZ*-plane are (r,φ). The picture corresponds to a multishell with a periodic alternation of two materials (from [Fomin15]).

considered because the length of fabricated micro- and nanotubes is much larger than their diameter. The effect of the finite length on the phonon energies is supposed to be negligible.

The displacement vector $\mathbf{u}_m$ in each layer ($m = 1, \ldots, N$), treated as an elastic continuum, obeys the equations of elastodynamics [Graff91]:

$$\mu_m \nabla^2 \boldsymbol{u}_m + (\lambda_m + \mu_m) \nabla\nabla \cdot \boldsymbol{u}_m = \rho_m \frac{\partial^2 \boldsymbol{u}_m}{\partial t^2}. \tag{3.1}$$

At every intershell boundary r_m ($m = 1, \ldots, N–1$), the following six boundary conditions represent continuity of the stress tensor components:

$$\begin{aligned} \sigma_{rrm} &= \sigma_{rrm+1}; \\ \sigma_{rxm} &= \sigma_{rxm+1}; \\ \sigma_{r\varphi m} &= \sigma_{r\varphi m+1}; \end{aligned} \tag{3.2}$$

and of the displacement vector components:

$$\begin{aligned} u_{rm} &= u_{rm+1}; \\ u_{xm} &= u_{xm+1}; \\ u_{\varphi m} &= u_{\varphi m+1}. \end{aligned} \tag{3.3}$$

At the internal boundary $r_{0,}$ the following three boundary conditions represent vanishing of the stress tensor components:

$$\begin{aligned} 0 &= \sigma_{rr1}; \\ 0 &= \sigma_{rx1}; \\ 0 &= \sigma_{r\varphi 1}. \end{aligned} \tag{3.4}$$

Similarly, at the external boundary r_N, the following three boundary conditions represent vanishing of the stress tensor components:

$$\begin{aligned} \sigma_{rrN} &= 0; \\ \sigma_{rxN} &= 0; \\ \sigma_{r\varphi N} &= 0. \end{aligned} \tag{3.5}$$

In total, there are $6N$ boundary conditions. The boundary problem described by eq. (3.1) and the boundary conditions (3.2) to (3.5) for an arbitrary number of the shell pairs satisfy the correspondence principle with respect to the case of a two-shell composite coaxial tube [Armenakas66, Armenakas71].

The solutions to the equations of elastodynamics are sought in the form of a combination of dilatational waves and shear (equivoluminal) waves:

$$u_m = \Delta\Phi_m + \nabla \times \mathbf{H}_m. \tag{3.6}$$

Here, the scalar potential of the dilatational motion and the vector potential of the shear motion along the axis of the structure (which has only two independent components) satisfy the equations:

$$\begin{aligned} v_{1m}^2 \nabla^2 \Phi_m &= \ddot{\Phi}_m, \\ v_{2m}^2 \nabla^2 \mathbf{H}_m &= \ddot{\mathbf{H}}_m. \end{aligned} \tag{3.7}$$

The velocities v_{1m} and v_{2m} correspond to dilatational and shear waves in the material of the mth layer. The solutions to the wave equations are sought as plane waves traveling along the axis of the structure.

Every two neighboring layers are assumed to be perfectly bonded. Therefore, the eigenwaves in all layers have the same longitudinal wave vector ζ and circular frequency ω:

$$\begin{aligned} \Phi_m &= f_m(r)\cos(n\varphi)\cos(\omega t+\zeta x),\\ H_{rm} &= h_{rm}(r)\sin(n\varphi)\sin(\omega t+\zeta x),\\ H_{\varphi m} &= h_{\varphi m}(r)\cos(n\varphi)\sin(\omega t+\zeta x),\\ H_{xm} &= h_{xm}(r)\sin(n\varphi)\cos(\omega t+\zeta x). \end{aligned} \tag{3.8}$$

A multishell with a periodic alternation of two materials is further assumed (see Fig. 3.1c with $r_0 = 100$ nm. All odd shells ($m = 2k+1$) consist of one and the same material with elastic properties λ_1, μ_1, density ρ_1 and have the same thickness: Δr_1. All even shells ($m = 2k$) consist of the same material with elastic properties λ_2, μ_2, density ρ_2 and have the same thickness: Δr_2. They are represented in Table 3.1. In what follows, the number of layers is denoted by N_L. The wave characteristics in the materials are defined in Table 3.2.

Table 3.1: Geometric and materials parameters of the multishell.

Parity *i* of the layer number *m*	**1**	**2**	**1**	**2**
Material	InAs [Ioffe98]	GaAs [Ioffe98]	Si [Ioffe98]	SiO_2[Bondi10]
λ_i, dyn/cm^2	4.54×10^{11}	5.34×10^{11}	9.8×10^{11}	5.67×10^{11}
μ_i, dyn/cm^2	1.90×10^{11}	3.285×10^{11}	5.2×10^{11}	3.4×10^{11}
ρ_i, g/cm^3	5.68	5.317	2.329	2.3
Δr_i, nm	5	5	18	2

Table 3.2: Definitions of the wave characteristics in the materials (from [Fomin15]).

Characteristic of the layer with parity *i* of the number *m*	**Denotation**
Velocity of a dilatational wave	$v_{1i} = [(\lambda_i + 2\mu_i)/\rho_i]^{1/2}$
Velocity of a shear wave	$v_{2i} = [\mu_i/\rho_i]^{1/2}$
Squared radial wave number for a dilatational wave	$\alpha_i^2 = \omega^2/v_{1i}^2 - \zeta^2$
Squared radial wave number for a shear wave	$\beta_i^2 = \omega^2/v_{2i}^2 - \zeta^2$
Dispersion of the Rayleigh waves $\alpha_i^2 = 0$	$\omega = v_{1i}\zeta$
Dispersion of the Rayleigh waves $\beta_i^2 = 0$	$\omega = v_{2i}\zeta$

The further procedure is a generalization of that in [Armenakas66] for a two-shell tube onto an arbitrary number of shells. Substituting the eigenwaves of eq. (3.8) into the differential equations of motion (3.7), we exclude three coordinates (t, x and φ) and arrive at a set of differential equations with respect to the radial coordinate r for the amplitude functions $f_m(r)$ and $h_{xm}(r)$ at $m = 1, 2, \ldots, N_L$:

$$\begin{aligned} &\frac{\partial^2 f_m}{\partial r^2} + \frac{1}{r}\frac{\partial f_m}{\partial r} + \left(\alpha_m^2 - \frac{n^2}{r^2}\right) f_m = 0, \\ &\frac{\partial^2 h_{xm}}{\partial r^2} + \frac{1}{r}\frac{\partial h_{xm}}{\partial r} + \left(\beta_m^2 - \frac{n^2}{r^2}\right) h_{xm} = 0 \end{aligned} \tag{3.9}$$

and two similar equations for the amplitude functions $h_{rm}(r)$ and $h_{\varphi m}(r)$. Due to gauge invariance of the vector potential, one of the functions $h_{rm}(r)$, $h_{\varphi m}(r)$, $h_{xm}(r)$ can be selected arbitrarily; we use, like in [Armenakas66], the calibration $h_{rm}(r) = -h_{\varphi m}(r) \equiv h_{1m}(r)$. The differential equations (3.9) are Bessel equations ([Abramowitz72], Chapter 9). Their solutions can be represented in the general form:

$$\begin{aligned} f_m(r) &= A_{1m} Z_n(|\alpha_m| r) + B_{1m} W_n(|\alpha_m| r), \\ h_{1m}(r) &= A_{2m} Z_{n+1}(|\beta_m| r) + B_{2m} W_{n+1}(|\beta_m| r), \\ h_{xm}(r) &= A_{3m} Z_n(|\beta_m| r) + B_{3m} W_n(|\beta_m| r), \end{aligned} \tag{3.10}$$

where Z_n (W_n) are the Bessel functions of the first kind J_n (second kind Y_n) ([Abramowitz72], p. 358) for the real radial wave numbers α_m and β_m and the modified Bessel functions I_n (K_n) ([Abramowitz72], p. 374) for the imaginary wave numbers α_m and β_m. In the set of solutions (3.10), there are in total $6N_L$ unknown coefficients, which can be represented as a $6N_L$-dimensional vector $\Xi \equiv \{A_{1m}, B_{1m}, A_{2m}, B_{2m}, A_{3m}, B_{3m} | m = 1, 2, \ldots, N_L\}$. After substituting the solutions (3.10) in the set of $6N_L$ boundary conditions (3.2) to (3.5), a homogeneous set of $6N_L$ linear algebraic equations with respect to $6N_L$ components Ξ_j ($j = 1, \ldots, N_L$) of the vector Ξ follows:

$$\sum_{j=1}^{6N_L} C_{ij} \Xi_j = 0, \quad i = 1, \ldots, 6N_L. \tag{3.11}$$

A nontrivial solution to this system exists under the condition that its $6N_L \times 6N_L$ determinant vanishes:

$$\det(C_{ij}) = 0, \quad i, \ j = 1, \ldots, 6N_L. \tag{3.12}$$

A numerical solution to the secular equation (3.12) is found using Intel® Visual Fortran with Microsoft Visual Studio 2008 [Intel08]. It provides phonon eigenfrequencies as a function of the longitudinal wave vector ζ. The resulting phonon dispersion

curves are represented below in the nondimensional form using the units, which are defined in Table 3.3.

Table 3.3: Units for wave characteristics (from [Fomin15]).

Physical quantity	Unit
Longitudinal wave vector ζ	$1/\Delta r_2$
Frequency ω	$\pi v_{22}/\Delta r_2$
Group velocity $d\omega/d\zeta$	πv_{22}

The lowest phonon dispersion curves (in the window of eigenfrequencies [0, 1.5]) are shown for axially symmetric waves $n = 0$, $N_L = 2$ in Fig. 3.2. More time-consuming calculations are required for flexural waves with $n \geq 1$. There are *anticrossings* of torsional or nontorsional modes, but there might occur *crossings* of torsional ($u_x = u_r = 0$, $u_\varphi \neq 0$) and nontorsional (associated with the displacement components u_x and u_r, $u_\varphi = 0$) modes. Dispersion of the phonon group velocity for the dispersion curves in Fig. 3.2 is represented in Fig. 3.3. The group velocity dispersion practically stops when the eigenfrequency ω goes beyond the window [0, 1.5].

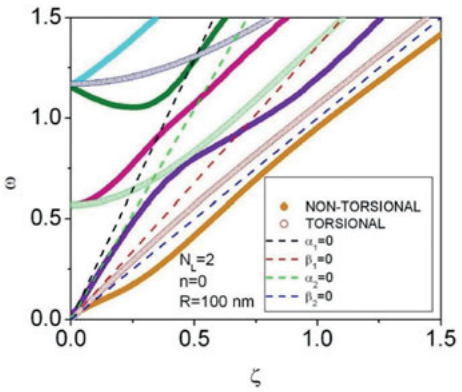

Fig. 3.2: Phonon dispersion curves for $n = 0$, $N_L = 2$. The inner and outer radii of a multishell are $r_0 = 100$ nm and $r_2 = 110$ nm, respectively. Nontorsional and torsional modes are represented with filled and empty circles, correspondingly. Dashed lines indicate the dispersion curves for dilatational ($\alpha_l = 0$) and shear ($\beta_l = 0$) waves in the material with parity i of the number m (from [Fomin15]).

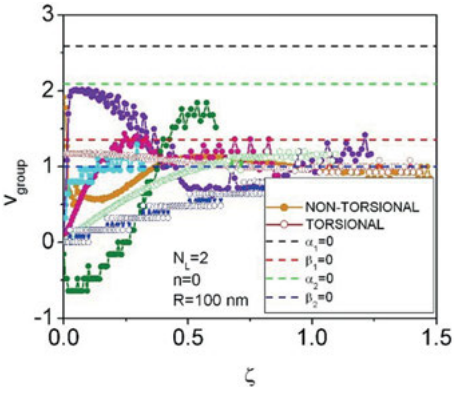

Fig. 3.3: Phonon group velocity dispersion curves for $n = 0$, $N_L = 2$. Denotations of nontorsional and torsional modes are the same as in Fig. 3.2 (from [Fomin15]).

The lowest phonon dispersion curves are shown for axially symmetric waves $n = 0$, $N_L = 4$ in Fig. 3.4. For clarity, dispersion curves for nontorsional and torsional waves are represented separately. A larger number of phonon dispersion curves in multishells with four shells emerge within the same interval of energies and wave vectors as for multishells with two shells in Fig. 3.2. Dispersion of the phonon group velocity for the lowest dispersion curves in Fig. 3.4 is represented in Fig. 3.5.

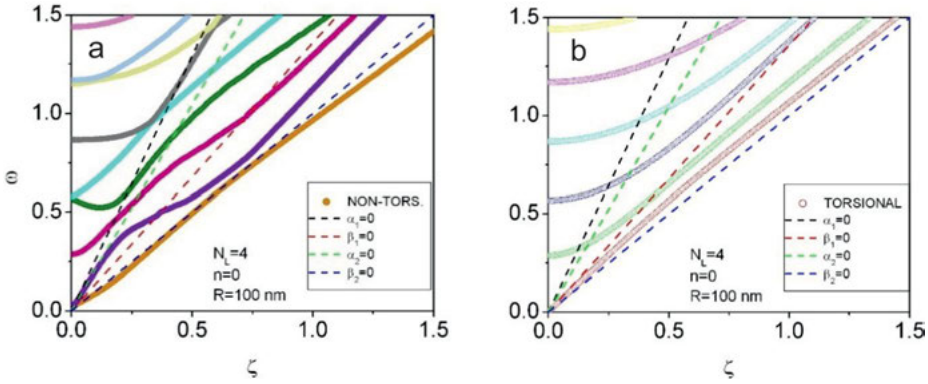

Fig. 3.4: Phonon dispersion curves for nontorsional (a) and torsional (b) waves at $n = 0$, $N_L = 4$. The inner and outer radii of a multishell are $r_0 = 100$ nm and $r_4 = 120$ nm, respectively (from [Fomin15]).

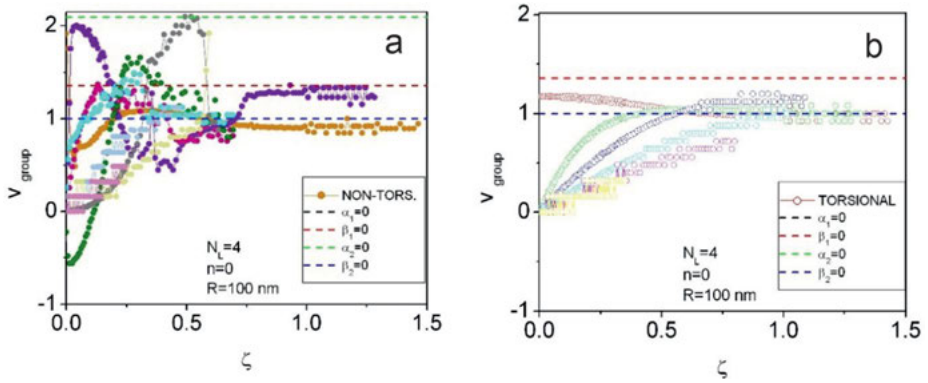

Fig. 3.5: Phonon group velocity dispersion curves for nontorsional (a) and torsional (b) waves at $n = 0$, $N_L = 4$ (from [Fomin15]).

The lowest phonon dispersion curves are shown for axially symmetric waves $n = 0$, $N_L = 6$ in Fig. 3.6. A larger number of dispersion curves in multishells with six shells emerge within the same interval of energies and wave vectors as for multishells with four shells in Fig. 3.4 and even more so for multishells with two shells in Fig. 3.2. Dispersion of the phonon group velocity for the lowest dispersion curves in Fig. 3.6 is represented in Fig. 3.7.

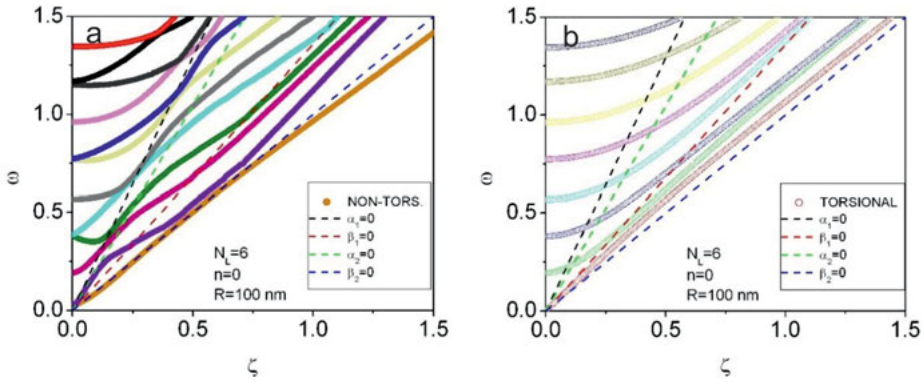

Fig. 3.6: Phonon dispersion curves for nontorsional (a) and torsional (b) waves at $n = 0$, $N_L = 6$. The inner and outer radii of a multishell are $r_0 = 100$ nm and $r_6 = 130$ nm, respectively (from [Fomin15]).

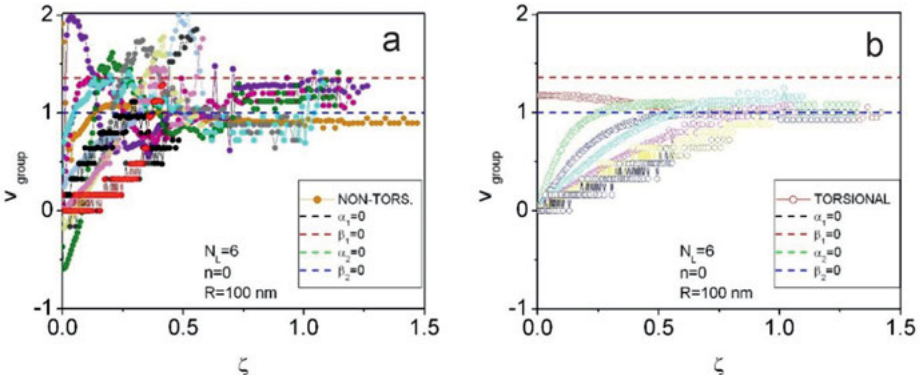

Fig. 3.7: Phonon group velocity dispersion curves for nontorsional (a) and torsional (b) waves at $n = 0$, $N_L = 6$ (from [Fomin15]).

For the axially symmetric waves ($n = 0$), as follows from Figs. 3.2, 3.4 and 3.6, the lowest group of the phonon dispersion curves, containing one torsional and two nontorsional modes, at the small wave vectors ζ is only slightly changed by the number of layers N_L. In the same region of wave vectors, the second, consisting of one torsional and one nontorsional modes (the third, consisting of one torsional and two nontorsional modes) group of the phonon frequencies ω significantly decreases from 0.57 (1.17) for $N_L = 2$ to 0.29 (0.57) for $N_L = 4$ and 0.19 (0.38) for $N_L = 6$. Within the numerical accuracy, the decrease of the phonon frequencies in the long-wave limit is inversely proportional to N_L. Away from the long-wave limit, a general trend of "compression" of the phonon energy spectrum towards lower values of phonon frequencies persists.

As shown in Figs. 3.3, 3.5 and 3.7, the phonon group velocity related to the fundamental (lowest) torsional mode is a weakly varying function of the wave vector ζ, while for the higher torsional modes it monotonously increases with the wave vector ζ towards saturation. For a fixed value $\zeta = 0.05$, the phonon group velocity related to the lowest (second lowest) torsional mode depends on the number of layers N_L as follows: 1.17 (0.13) for $N_L = 2$; 1.17 (0.27) for $N_L = 4$ and 1.17 (0.37) for $N_L = 6$. Within the numerical accuracy, the increase of the phonon group velocity for the second lowest torsional mode is directly proportional to N_L.

The phonon group velocity related to the lowest two nontorsional modes is a weak function of the wave vector ζ, while for higher torsional modes it always strongly depends on ζ. For the same fixed value $\zeta = 0.05$ as above, the phonon group velocity related to the lowest (second lowest and third lowest) nontorsional mode depends on the number of layers N_L as follows: 0.75 (2.02 and 0.43) for $N_L = 2$; 0.75 (1.98 and 0.82) for $N_L = 4$ and 0.78 (1.94 and 1.06) for $N_L = 6$. Within the numerical accuracy, the phonon group velocity for the third lowest non torsional mode reveals a sublinear dependence on N_L.

Finally, in order to clearly visualize the overall impact of the number of layers in a multishell on the group velocity dispersion, the average and root-mean-square (RMS) phonon group velocities are calculated for the branches available from the results of the previous analysis. The results, shown in Fig. 3.8, demonstrate that an increase of N_L from two to four leads to an appreciable decrease of the average and RMS phonon group velocities. A further increase of N_L from four to six has a smaller impact on the average and RMS phonon group velocities. For the wave vector $\zeta = 0.05$, the average phonon group velocity decreases from 0.82 for $N_L = 2$ to 0.54 for $N_L = 4$ and further to 0.53 for $N_L = 6$. At the same time, the RMS phonon group velocity is reduced from 0.95 for $N_L = 2$ to 0.71 for $N_L = 4$ and further to 0.65 for $N_L = 6$. At small wave vectors, the trend persists: the average and RMS phonon group velocities decrease with increasing N_L.

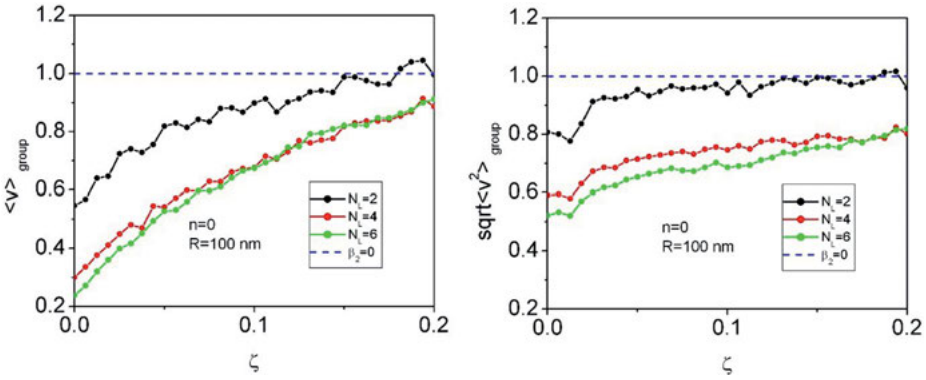

Fig. 3.8: Average (left panel) and RMS (right panel) phonon group velocity dispersion curves for $n = 0$ at $N_L = 2$, 4 and 6 (from [Fomin15]).

In summary, there exists a possibility of efficient engineering of the acoustic phonon energy dispersion [Balandin15] in multishell tubular structures produced by a novel method of self-assembly of micro- and nanoarchitectures. A dependence on the number of layers in a multishell structure is a manifestation of geometric effects on phonon energy spectrum. Such geometric effects are features pertinent to acoustic metamaterials and phonon crystals. Based on the calculated energies, the phonon confinement effects should be directly observable using Brillouin–Mandelstam spectrometry [Kargar16]. The changes in the acoustic phonon spectrum affect phonon transport and can be experimentally detected in thermal conductivity measurements. The above-discussed reduction of the phonon group velocity and phonon thermal conductivity seems to be possible without significant roughness scattering and degradation of electron transport. The arrays of self-rolled multishell tubular structures are prospective candidates for advancement in thermoelectric materials and devices.

3.2 Phonons in Si/SiO_2 multishell microtubes

Using the elastodynamic model of Section 3.1, the phonon properties are analyzed for Si/SiO_2 multishell microtubes with the inner radius $r_0 = 1,050$ nm. The geometric and materials parameters are provided in Table 3.1. As evident from the phonon dispersion curves in Fig. 3.9, with increasing the wave number, more phonon modes reveal an appreciable dispersion and therefore provide a larger contribution to the average phonon group velocity. The dispersion curves of torsional modes in a multishell structure exhibit moderate kinks when hitting the dispersion curve of a Rayleigh

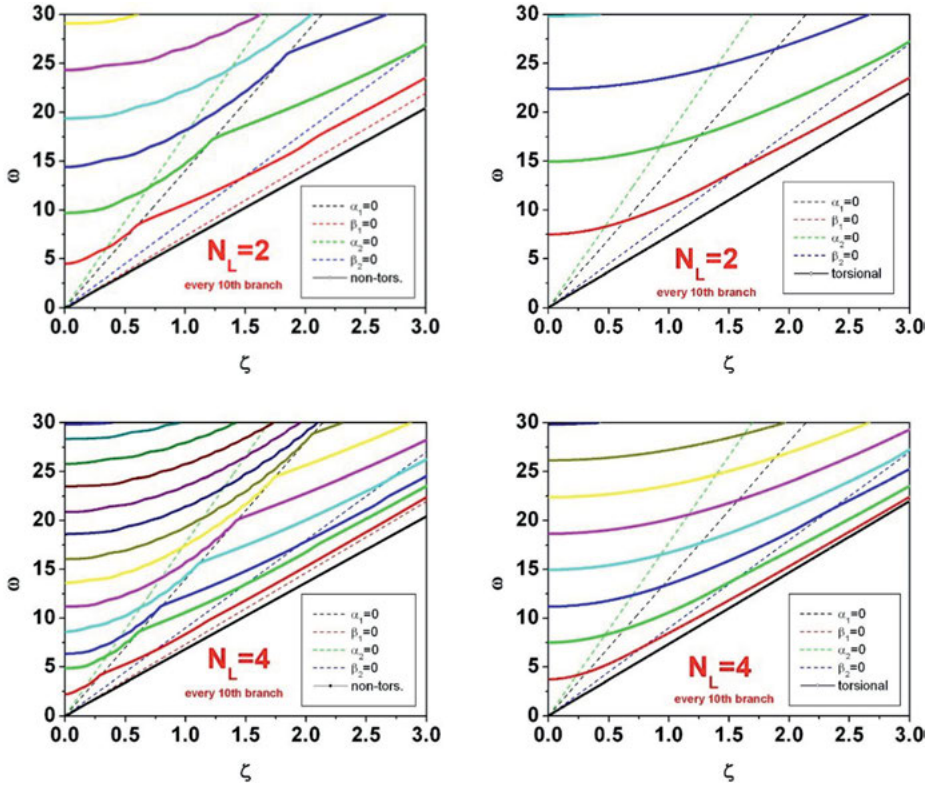

Fig. 3.9: Phonon dispersion curves in multishell tubes Si/SiO_2 with one winding ($N_L = 2$) and two windings ($N_L = 4$). The geometric parameters are $\Delta r_1 = 18$ nm, $\Delta r_2 = 2$ nm and $r_0 = 1,050$ nm. Thel unit for the phonon energy $\hbar\omega$ is ~5 meV. The unit for the wave number is ~5×10^8 m^{-1}. The lowest torsional branches are close to the Rayleigh wave $\beta 1 = 0$ (from [Fomin18c]).

wave at the surface of SiO_2, which stems from the dispersion relation for a shear wave $\beta_2 = 0$. The dispersion curves of nontorsional modes in a multishell structure manifest significant kinks when hitting the dispersion curve of a Rayleigh wave at the surface of Si, which corresponds to the dispersion relation of a dilatational wave $\alpha_1 = 0$. The phonon DOS represented in Fig. 3.10 reveals almost equidistant peaks typical of a one-dimensional quantum wire. It is worthy of notice, that the periods of the phonon DOS manifest a hyperbolic dependence on the number of windings $N_L/2$. The corresponding average group velocities represented in Fig. 3.10 as a function of energy reflect the spectral structure of the phonon DOS. Similar to Fig. 3.8, the phonon group velocity calculated for long-wave phonons in Si/SiO_2 multishell tubes systematically decreases within increasing N_L [Fomin18c].

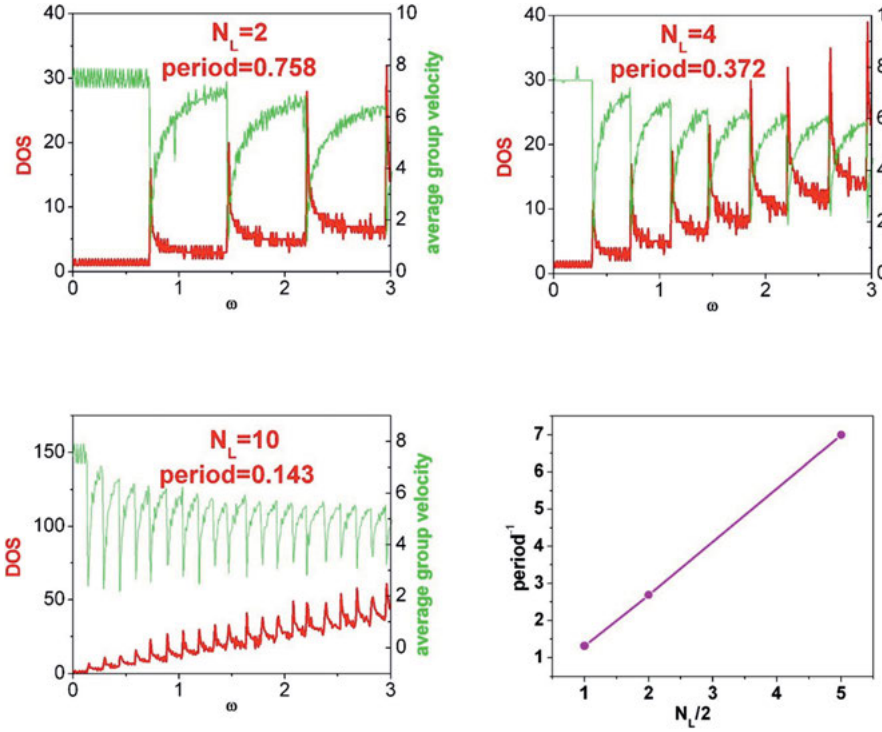

Fig. 3.10: Phonon DOS (red) and the average phonon group velocity (green) in multishell tubes Si/SiO_2 with one winding ($N_L = 2$), two windings ($N_L = 4$) and five windings ($N_L = 10$) calculated for the dispersion curves shown in Fig. 3.9. The periods of DOS (found using FFT) as a function of frequency are shown in panels (a) to (c) (after [Fomin18c]) and as a function of the number of windings in panel (d).

Phonon thermal conductivity is calculated within the formalism of ref. [Callaway59] using the average group velocities from Fig. 3.10 and the phonon scattering mechanisms for superlattices [Li17]. Within the assumed model, the scattering rate is generalized as compared to [Li17] (Supporting Information) as follows:

$$\tau^{-1}(\omega) = \frac{d_{\mathrm{Si}}}{d}\tau^{-1}_{\mathrm{bulk\,Si}}(\omega) + \frac{d_{\mathrm{SiO_2}}}{d}\tau^{-1}_{\mathrm{bulk\,SiO_2}}(\omega) + \frac{N_L}{2}\tau_I^{-1}(\omega). \tag{3.13}$$

Here, the bulk scattering rates of materials of both shell types are weighted with factors, representing their relative width d_{Si}/d, $d_{\mathrm{SiO_2}}/d$, while the number of windings $N_L/2$ as a factor in front of the interface scattering rate for a single interface is invoked in order to explicitly take into account the corresponding increase of the mechanical interface area. As shown in Fig. 3.11, the elastodynamic model of

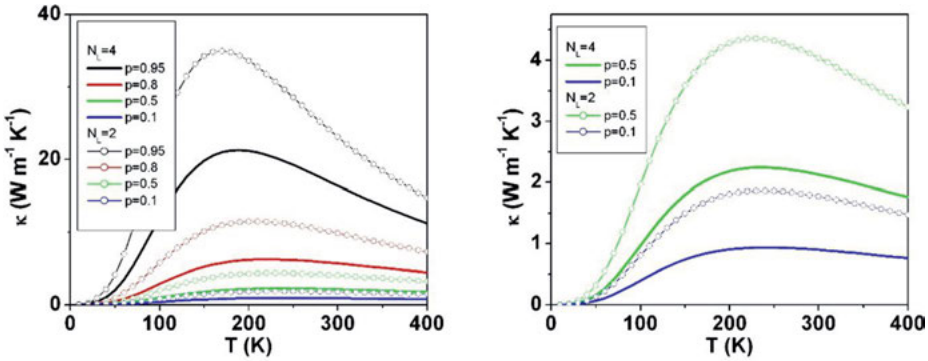

Fig. 3.11: Phonon thermal conductivity for multishell tubes Si/SiO_2 with one winding ($N_L = 2$) and two windings ($N_L = 4$) estimated within the formalism of ref. [Callaway59] using the average group velocities from Fig. 3.10 and the phonon scattering mechanisms for superlattices [Li17].

phonons allows for an explanation of the decay of the calculated phonon thermal conductivity with increasing the number of windings.

Scattering parameters significantly change the value of the thermal conductivity and its behavior as a function of temperature. For instance, when decreasing the specularity parameter p from 0.95 to 0.1, which corresponds to enhancement of the interface scattering, the maximum of the thermal conductivity as a function of temperature shifts to higher temperatures, while the values of the thermal conductivity at 400 K decrease by a factor of more than 10. Optimization of the thermal conductivity range requires a fine-tuning of the scattering parameters appropriate for multishell tubes in conjunction with the available experimental data.

3.3 Thermal conductivity of HNMSLs

A novel approach to manage thermal conductivity of Si thin-film-based high-tech nanoarchitectures through the formation of rolled-up radial and pressed-back planar Si/SiO_x HNMSLs shown in Fig. 3.12 has been realized [Li17]. The in-plane thermal conductivity is measured in three types of Si/SiO_x HNMSLs configurations with diverse numbers of windings (1, 2 and 5), while three planar HNMSLs each incorporating stacked Si/SiO_x nanomembranes are then selected to carry out comparative measurements. First, it is demonstrated that the in-plane thermal conductivities of the radial Si/SiO_x HNMSLs with various numbers of windings (1, 2 and 5) show a tremendous reduction relative to the bulk single-crystalline silicon at temperatures ranging from 300 to 400 K. Second, a continuous reduction in thermal conductivity with increasing number of windings is observed, indicating thermal correlations

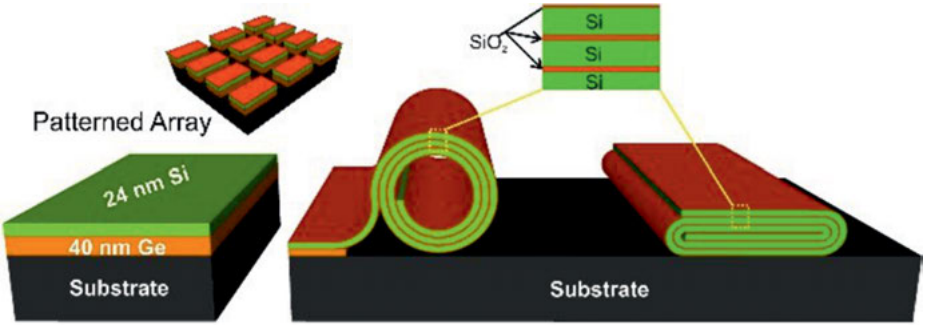

Fig. 3.12: Schematic diagram of a Si thin-film sample as well as a self-rolled radial and pressed-back planar Si/SiO_x HNMSL (from [Li17]).

between the layers of Si/SiO_x HNMSLs. Third, planar Si/SiO_x HNMSL, which are fabricated by mechanically compressing the 5-winding radial tube, shows the in-plane thermal conductivity in the range of 4.4 to 5.7 W m^{-1} K^{-1} at temperatures from 200 to 400 K, which is the smallest among the values of Si-based planar superlattices reported before ref. [Li17].

To obtain an insight into the phonon transport processes in HNMSLs, we propose a model simulating the phonon thermal conductivity of planar Si/SiO_x HNMSLs in the framework of a linearized Boltzmann transport equation (BTE) [Volz99, Mingo03, Nika12]. For the simulation, we assume a superlattice period consisting of 20-nm single-crystalline Si and 2-nm amorphous SiO_2 on each side, as shown schematically in Fig. 3.12a. Within the Born–von Kármán (BvK) theory of lattice dynamics, the phonon dispersion is calculated in planar Si/SiO_2 HNMSLs. The set of equations of motion for atoms from the monolayer s of a HNMSL can be written in a harmonic approximation as follows:

$$m\omega^2 U_i(n_s,\vec{\mathbf{q}}) = \sum_{n'_{s'}} \sum_{j=x,y,z} \Phi_{ij}(n_s, n'_{s'}) \exp\left(i\vec{\mathbf{q}} \cdot \left(\vec{\mathbf{r}}(n'_{s'}) - \vec{\mathbf{r}}(n_s)\right)\right) U_j(n'_{s'},\vec{\mathbf{q}}), \qquad (3.14)$$

where $i = x, y, z$, m is the mass of an atom, ω is the phonon frequency, $\vec{\mathbf{q}}$ is the phonon wave vector, $\vec{\mathbf{U}}$ is the displacement vector, $\vec{\mathbf{r}}(n_s)$ is the radius-vector of the nth atom from the sth monolayer and Φ is the force constant matrix. The interaction is considered between the atoms from the nearest- and second nearest-neighbor atomic spheres; therefore, the summation in eq. (3.14) is performed over all atoms $n'_{s'}$ from two neighbor spheres of the atom n_s. The force constant matrix contains three independent force constants: α, β and μ. Having solved eq. (3.14) in the long-wavelength limit $q \to 0$, we express the interatomic force constants through independent elastic moduli of a bulk material c_{11} and c_{44} as: $\alpha = a\pi^2 c_{11}/16$, $\beta = \sqrt{\alpha(a(c_{11} - 2c_{44}) + \alpha)/2}$ and $\mu = (ac_{11} - \alpha)/8$, where a is the corresponding lattice constant.

The amorphous SiO_2 layers are treated in the virtual crystal (VC) approximation, which has been extensively used for modeling vibrational and thermal properties of disordered materials and interfaces. The translational symmetry of the SiO_2 material under the VC approximation [Abeles63, Ma05, Beechem07, Larkin13] results in the appearance of a pseudo-BZ with definite wave numbers q_x, q_y, q_z characterized by the microscopic reference state in the form of a crystal lattice with a lattice constant a. The pseudo-BZ terminology for glasses is discussed in ref. [Grest84]. Using the pseudo-BZ concept, the authors of ref. [Chumakov11] associate the well-known "boson peak," characteristic to all amorphous materials, with the singularities of transverse acoustic vibrations near the pseudo-BZ boundary. Moreover, both longitudinal and transverse acoustic phonon dispersion curves in SiO_2, calculated within the BvK model (see green curves in Fig. 3.13b), are in a good accordance with the inelastic X-ray and neutron scattering experiments for amorphous silica at wave numbers up to ~6 nm^{-1} [Baldi08]. For Si/SiO_2 HNMSL, the periodicity of the $SiO_2/Si/SiO_2$ segments results in the occurrence of the pseudo-BZ with the wave number q_z between 0 and π/d, where $d = d_{Si} + 2d_{SiO_2}$ is the superlattice period.

In Fig. 3.13b,c, the obtained phonon energy spectra are shown for the in-plane $\omega_s(q_x)$ and cross-plane $\omega_s(q_z)$ directions. For comparison, both in-plane and cross-plane phonon branches of bulk Si and SiO_2 are shown together. It is worthy of noticing that for the in-plane direction, the BZs of bulk materials and HNMSLs are almost of the same size, while the BZ of the HNMSL for the cross-plane direction is ~1/90th of the corresponding value for the in-plane case due to the zone folding. The average phonon group velocity is calculated over all (q_x, q_z) directions in the BZ and the results are plotted as a function of the phonon energy in Fig. 3.13d. From Fig. 3.13d, the impact of the phonon confinement on phonon energy dispersion and group velocities in Si/SiO_2 HNMSLs is revealed. Importantly, there appear hybrid vibrational modes propagating in the whole structure, rather than separate vibrational modes in individual Si or SiO_2 layers. Finally, a linearized BTE approach is used to calculate the heat transport. By comparing the experimental temperature dependence of thermal conductivity of bulk Si with our model, we find phonon scattering mechanisms characteristic of this material. A good agreement between theoretical and experimental thermal conductivities is obtained considering Umklapp and point-defect scattering:

$$\tau^{-1}_{\mathrm{Si},\,s}(q) = \tau^{-1}_{U,\,s}(q) + \tau^{-1}_{\mathrm{PD},\,s}(q). \tag{3.15}$$

The Umklapp scattering rate is calculated as [Mingo03]

$$\tau^{-1}_{U,\,s}(q) = B(\omega_s(q))^2 T \exp\left(-\frac{C}{T}\right), \tag{3.16}$$

where $B = 1.82 \times 10^{-19}$ s/K and $C = 177.0$ K. The point-defect scattering rate is calculated as [Klemens94]

$$\tau^{-1}_{\mathrm{PD},\ s}(q) = \frac{V_0}{4\pi} \Gamma \frac{(\omega_s(q))^4}{(v_s(q))^3}, \tag{3.17}$$

where V_0 is the volume per atom, Γ is the strength of the point-defect scattering ($= 0.0002012$ for natural Si).

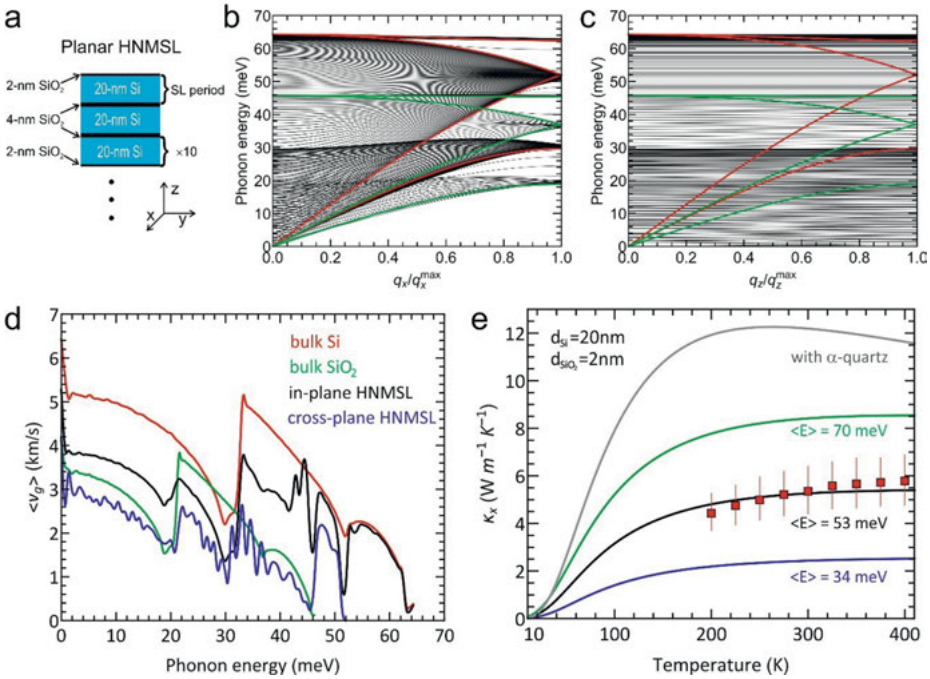

Fig. 3.13: (a) Schematic structure of a planar Si/SiO_2 HNMSL with a SL period consisting of 2 nm SiO_2, 20 nm Si and 2 nm SiO_2. (b–c) Phonon energy spectra along the q_x (in-plane) and q_z (cross-plane) directions from the Brillouin zone center for Si/SiO_2 HNMSL (black curves), bulk Si (red curves) and bulk SiO_2 (green curves). For bulk Si: $q_x^{max} = q_z^{max} = 11.57\ nm^{-1}$; for bulk SiO_2: $q_x^{max} = q_z^{max} = 11.64\ nm^{-1}$; for the superlattice: $q_x^{max} = 11.57\ nm^{-1}$, $q_z^{max} = 0.13\ nm^{-1}$. (d) Average phonon group velocity as a function of the phonon energy for Si/SiO_2 HNMSL (black curve, in-plane component; purple curve, cross-plane component), bulk Si (red curve) and bulk SiO_2 (green curve). (e) In-plane lattice thermal conductivity as a function of temperature in Si/SiO_2 HNMSL. Red solid squares denote the experimental data. Theoretical calculations for HNMSL with amorphous SiO_2 layers at different values of mean vibrational energy: $\langle E \rangle = 34$ meV (purple curve), $\langle E \rangle = 53$ meV (black curve) and $\langle E \rangle = 70$ meV (green curve) are presented, along with those for HNMSL with crystalline α-quartz layers (gray curve) (from [Li17]).

In case of bulk amorphous SiO_2 or other amorphous materials, it is accepted [Allen89] that the major part of thermal energy is transferred by diffusion between localized atomic vibrations, rather than by propagating waves (as in crystalline materials). Therefore, a description of the thermal transport should be carried out in terms of vibration diffusivity rather than in terms of phonon lifetimes or group velocities. However, comparing the equation for thermal conductivity obtained in ref. [Allen89] based on vibration diffusion mechanism with that obtained from BTE, an "effective relaxation rate" of phonons in amorphous SiO_2 can be introduced in the form:

$$\tau^{-1}_{SiO_2,\ s} = (v_s(q))^2 \frac{3\omega_s(q)}{a^2 A \bar{\omega}^2}, \tag{3.18}$$

where $a = 0.235$ nm is the bond length, $\bar{\omega}$ is the mean vibrational frequency, $v_s = \frac{d\omega_s(q)}{dq}$ is a group velocity of the (s, q) vibration mode and $A = 0.33$ is taken from ref. [Allen89]. The validity of this approach is checked by comparison of theoretical and experimental [Cahill87] curves of temperature-dependent thermal conductivity in bulk amorphous SiO_2. The best accordance between theory and experiment is achieved for mean vibrational energy $\hbar\bar{\omega} = 34$ meV. The obtained good agreement between theoretical and experimental results [Cahill87] confirms accuracy of the proposed model for the description of thermal processes in amorphous SiO_2.

The resulting in-plane phonon thermal conductivity$_{kx}$ of a Si/SiO_2 HNMSL is plotted as a function of temperature in Fig. 3.13e. The theoretical calculations are performed for different values of the mean vibrational energy $\langle E\rangle = \hbar\langle\bar{\omega}\rangle$ in SiO_2, namely, 34 meV (purple curve), 53 meV (black curve) and 70 meV (green curve). The experimental data points are denoted with red squares. The computed values of κ_x show a good agreement with experimental data for $\langle E\rangle = 53$ meV.

In order to reveal the impact of the structural disorder of amorphous SiO_2 on the thermal conductivity of Si/SiO_2 HNMSL, we have carried out calculations with crystalline SiO_2 layers. As an example of crystalline SiO_2, α-quartz is taken, and the in-plane κ_x in Si/ α-quartz HNMSL is shown by the gray curve in Fig. 3.13e. A 53–60% drop of thermal conductivity for temperatures between 100 and 400 K is observed when comparing HNMSLs with crystalline α-quartz layers and amorphous SiO_2 layers, respectively. Therefore, our calculations reveal a strong dependence of the lattice thermal conductivity in Si/SiO_2 HNMSL on the structural and vibrational properties of the SiO_2 layers. This conclusion is, generally, in line with that made in ref. [Neogi15] based on MD simulations, namely, that ultrathin SiO_x layers natively grown on both sides of a silicon membrane could significantly suppress the overall thermal conductivity of the structure. A 100-fold drop of the thermal conductivity in comparison with bulk Si is also predicted in ref. [Donadio09] for thin Si nanowires with amorphous surface, due to a decrease of propagating

mode lifetimes at the crystalline–amorphous interface combined with the presence of diffusive vibration modes. In conclusion, based on the developed theoretical model and under the same scattering mechanisms, the cross-plane thermal conductivity $\kappa_z = 1.1$ $\mathrm{Wm^{-1}K^{-1}}$ at room temperature is obtained in a good agreement with the experimental value [Grimm14].

4 Magnetized rolled-up microstructures

4.1 Dynamics of magnetized microhelix coils

Along with the ferro- (parallel) and antiferromagnetic (antiparallel) spin ordering in magnetic materials, nature proposes a variety of complex topologically stable magnetic configurations. Examples of such configurations are skyrmion magnetic (spin) texture, in which the magnetic moments (spins) form a vortex-like configuration or point in all the directions wrapping a sphere [Bogdanov89, Bogdanov01, Romming13], helical spin texture, which is characterized by a gradual spatial tilt of adjacent discrete spins [Uchida06] or magnetic toroidal moment [Ederer07] observed in bulk multiferroic materials. They lead to novel topology-driven transport effects, such as the topological Hall effect [Lee09, Yu10]. Design and characterization of self-rolled 3D microhelices with different magnetization configurations [Smith11] offer an unprecedented microscale implementation of topologically nontrivial magnetic textures.

Three-dimensional microhelix coils are fabricated by rolling up highly strained magnetic strips on a substrate surface [Smith11]. The strips are magnetized in different orientations prior to roll up, thus leading to various different magnetic states. The concept outlined by micromagnetic simulations (see [Smith11] for details) is shown in Fig. 4.1a–c. If the magnetic moment is oriented in-plane, orthogonally to the strip axis, the coiling process results in a *hollow-bar-magnetized structure* (Fig. 4.1a). If the magnetic moment is oriented in-plane, parallelly to the strip axis, a *corkscrew-magnetized helical* coil structure occurs (Fig. 4.1b). If the easy axis of magnetization of the strip is pointing out-of-plane, a *radial-magnetized helical* coil geometry is realized (Fig. 4.1c).

The fabrication relies on the following process [Smith11]. First, SU8 strips ($L = 1$ mm $\times$ $W = 7$ μm $\times$ $H = (2–10$ μm$)$) are defined by means of photolithography. Next, an "active" magnetic layer is deposited. A 20-nm-thick Co film is chosen to create either corkscrew-magnetized or hollow-bar-magnetized helix coil structures (Fig. 4.1a,b). The radial-magnetized coils (Fig. 4.1c) are made using an "active" magnetic $[Co(0.4\ nm)/Pt(0.6\ nm)]_5$ multilayer stack with a well-defined out-of-plane easy axis of magnetization [Hashimoto89, Carcia85]. In addition, a reference nonmagnetic sample consisting of a $[Cu(0.4\ nm)/Pt(0.6\ nm)]_5$ multilayer is also prepared [Smith11]. Deposition of the "active" layer onto SU8 leads to a differential strain throughout the structure [Schmidt01a]. A delamination process is then performed by placing the sample into *N*-methyl-2-pyrrolidone, and the "active" strips spontaneously form into the 3D hybrid helix coils of radius 35 μm and length 50 μm.

Because it is challenging to directly measure the magnetic configuration of the coils, the magnetic state is revealed by probing the response of the coils to an alternating external magnetic field [Smith11]. If the magnetic strip is prepared out of the

https://doi.org/10.1515/9783110575576-004

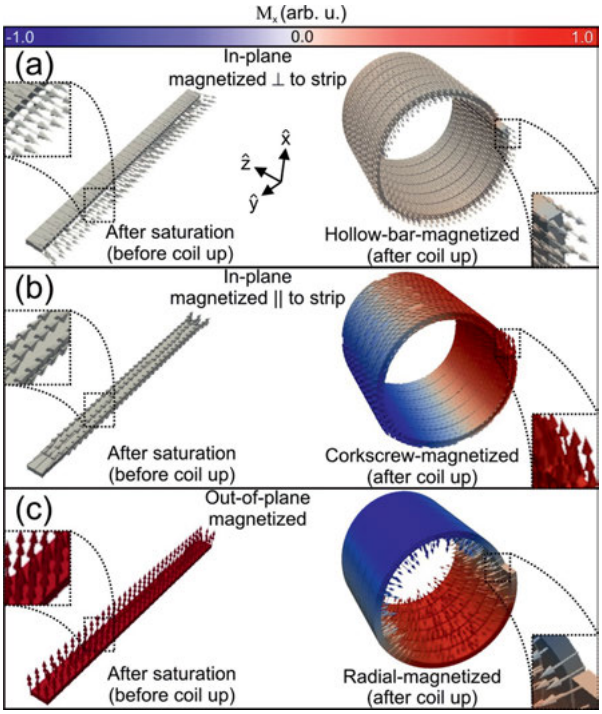

Fig. 4.1: FEM simulations of the different obtainable magnetizations using a coiling approach. (a) With initial in-plane, perpendicular-to-strip magnetized structures (left), hollow-bar-magnetized helix coils can be created (right). (b) With initial in-plane, parallel-to-strip magnetized structures (left), corkscrew-magnetized structures can be created (right). **(c)** If the strips have an out-of-plane magnetic moment (left), radial-magnetized structures result (right) (after [Smith11]).

[Co/Pt] multilayers, which are initially out-of-plane magnetized, the forward motion of the coil is found to be directionally deterministic (Fig. 4.2a). The coils with an in-plane "active" layer (magnetized parallelly to the strip before roll-up) exhibit a forward dancing motion (Fig. 4.2b). The coils with the other in-plane magnetized configuration (magnetized perpendicularly to the strip before roll-up) perform end-over-end tumbling because the effective magnetic moment is similar to a hollow bar magnet (Fig. 4.2c). The directionally deterministic motion is exceptional for the out-of-plane magnetized coil.

Given the small size of the coil and the distance from the sample to the external magnet (approximately 3 cm), the magnetic field gradient of the external magnet is rather small. Therefore, the main source of the force acting on the coil is due to a magnetic torque, while the magnetic field gradient has only a minor influence over the motion.

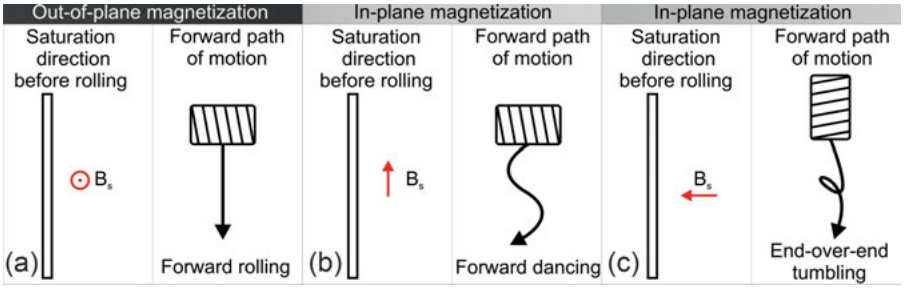

Fig. 4.2: Coil trajectory versus magnetized film orientation. (a) Straight and deterministic forward motion of coils with out-of-plane magnetized films. (b) Coils with in-plane magnetized films in the parallel-to-strip direction exhibit forward dancing motion. (c) Coils with in-plane magnetized films in the perpendicular-to-strip direction exhibit end-over-end tumbling motion (after [Smith11]).

Due to its symmetry, a radial-magnetized cylinder is expected to be magnetically compensated. However, a coil structure has an uncompensated magnetic moment as a result of the windings at either end. The uncompensated moment of the coil tries to align to the orientation of the external magnetic field. Given that the coercive field of the film (≈ 22 mT) is sufficiently larger compared to the external magnetic field (≤10 mT), a switching of the magnetic moment orientation in the $[Co/Pt]_5$ multilayer stack is unlikely. Therefore, alignment of the uncompensated magnetic moment is only possible through a physical rotation of the coil around the z-axis (Fig. 4.3). We can track one end of a coil in comparison to the rotation of the external magnetic field (schematized in Fig. 4.3b,d, respectively).

The external magnet is rotated at various angular velocities, ω_{mag}. The time evolution of the applied external magnetic field of the bar magnet, measured using a Hall probe, is shown in Fig. 4.4. This experimentally determined field profile, red dots, is fitted with different functions, with the best fit resulting from an average of the first five odd powers of a cosine functions, $\frac{\zeta}{5}\sum_{n=0}^{4}\cos^{2n+1}(\omega_{mag}t+\varphi)$, blue line.

The responding angular position of the coil, Ψ_{coil}, is recorded (Fig. 4.5a–c). The slopes of the data fit, τ, are used to derive an average rotational angular velocity of the coil. Yet, as discussed later, due to the nonlinear nature of the motion, τ does not represent the real full angular velocity of the coil. The average rotational angular velocity increases with increasing ω_{mag}. However, as ω_{mag} increases, τ begins to lag behind and eventually drops off above a certain critical frequency $\omega_{mag}^{transition}$. This behavior is characteristic of all coils investigated, and $\omega_{mag}^{transition}$ is found to be dependent on the coil dimensions. For the coil under discussion, a critical frequency region of $250°\ s^{-1} < \omega_{mag}^{transition} < 300°\ s^{-1}$ is measured, described as a transition from rotational to *oscillatory-like rotational* (OLR) motion. If a close-up (3 s time lapse) is made for $\omega_{mag} = 150°\ s^{-1}$ and $200°\ s^{-1}$, Fig. 4.5b, one can see that Ψ_{coil} versus t has an overall positive slope. When $\omega_{mag} > \omega_{mag}^{transition}$, OLR motion of the coil occurs, which is composed of oscillations superimposed over the rotational motion, Fig. 4.5c.

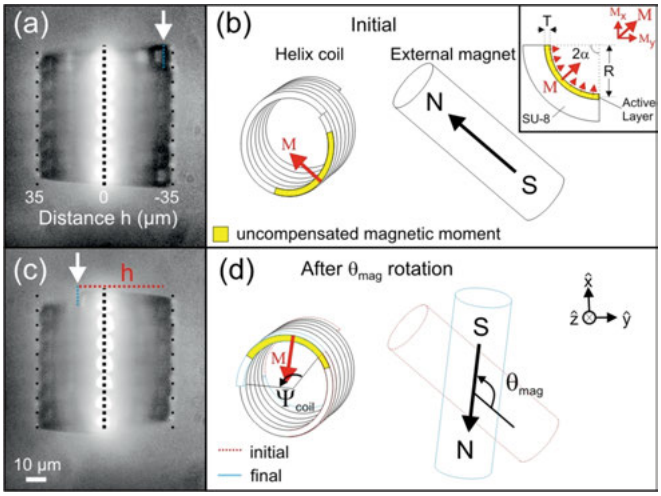

Fig. 4.3: Response of radial-magnetized coils to an external magnetic field. (c) An external magnetic field leads to an alignment of the coil's magnetic moment. (b) A schematic of the coil's uncompensated magnetic moment (highlighted in yellow) aligning with the external magnetic field. The inset of (b) shows the geometry making up the uncompensated magnetic moment component of the active layer. As the external magnet is rotated, the coil is forced to rotate by approximately the same number of degrees due to the uncompensated out-of-plane magnetic moment of the coil. (c) Tracking of either end of the coil can be made (red dotted line) to show the motion over approximately 120° rotation of the external magnet. (d) A schematic of coil's rotation, Ψ_{coil}, after a rotation of the external magnet, θ_{mag} (from [Smith11]).

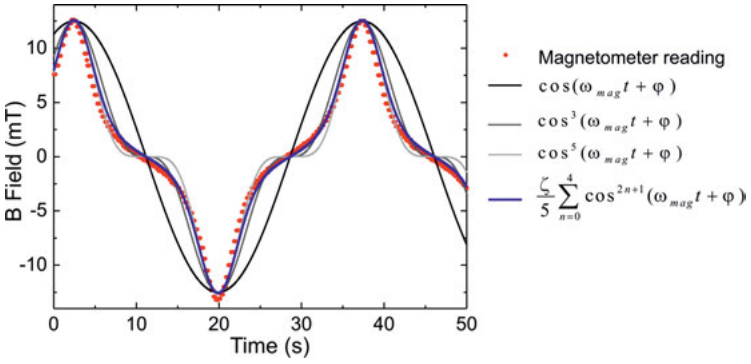

Fig. 4.4: Fit for the external applied magnetic field as a function of time. The magnetic field intensity as a function of time measured with a Hall probe (red dots). Different functions are used to fit the data. The best fit is an average of odd cosine functions, $\frac{\zeta}{5}\sum_{n=0}^{4}\cos^{2n+1}(\omega_{mag}t+\varphi)$ (blue line) (from [Smith11]).

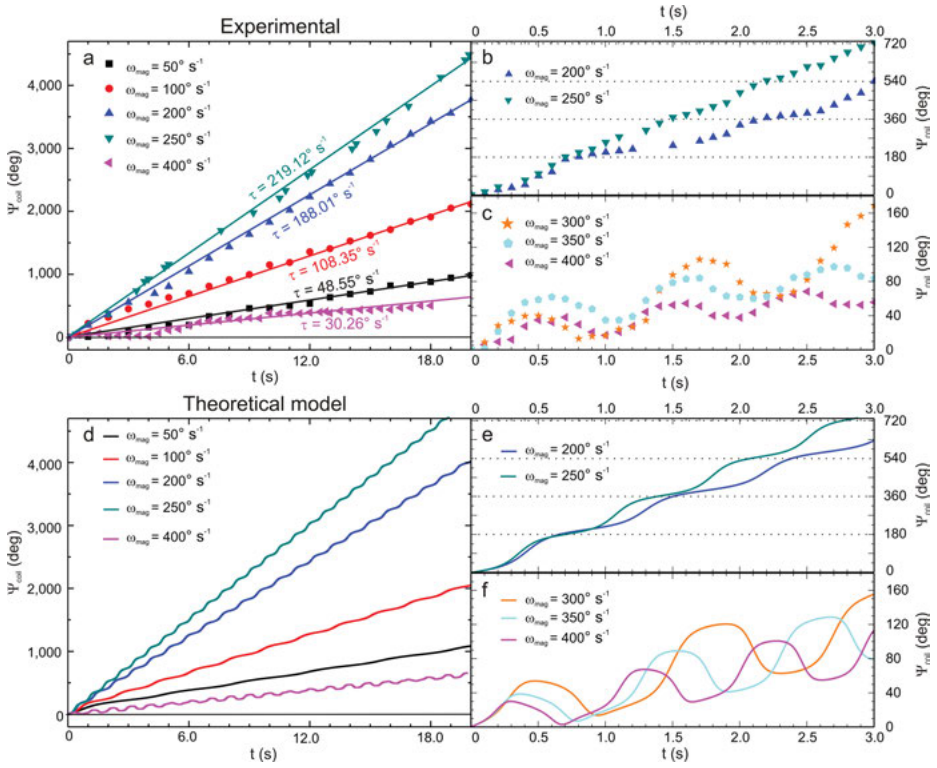

Fig. 4.5: Dynamics of coil versus rotation of external magnetic field. (a) Data taken comparing Ψ_{coil} versus t for various ω_{mag}. The slope, τ, of each curve reveals the average rotation speed of the coil for a corresponding ω_{mag}. When $\omega_{mag} \geq \omega_{mag}^{transition}$ (here 250° s^{-1} <$\omega_{mag}^{transition}$< 300° s^{-1}), the average rotational velocity of the coil drops off. (b) A close-up view of two full rotations of the coil for values of $\omega_{mag} < \omega_{mag}^{transition}$ shows that $\Psi_{coil}(t)$ is not linear; however, the motion of the coil is rotational. (c). A close-up view for $\omega_{mag} > \omega_{mag}^{transition}$ over the same timescale as in (b) illustrates an OLR motion of the coil, revealing the drop-off in the average rotational velocity. Corresponding theoretical trajectories in panels (d), (e) and (f) are calculated using the model described in the text (from [Smith11]).

The dynamics of a coil possessing an uncompensated magnetic moment **M** (Fig. 4.3b) and immersed in a liquid are modeled by the equation of motion:

$$I\frac{d^2\Psi_{coil}}{dt^2} = T(\Psi_{coil}, t), \tag{4.1}$$

where $I = m(R_{ext}^2 - R_{int}^2)/2$ is the moment of inertia for a coil of mass m with internal and external radii R_{ext} and R_{int}, correspondingly. The total torque [Helgesen90]

$$T(\Psi_{coil}, t) = T_M(\Psi_{coil}, t) + T_H \tag{4.2}$$

consists of the magnetic torque

$$T_{\mathrm{M}}(\Psi_{\mathrm{coil}}, t) = [\mathbf{M}(\Psi_{\mathrm{coil}}) \times \mathbf{B}(t)]_z = M_x(\Psi_{\mathrm{coil}})B_y(t) - M_y(\Psi_{\mathrm{coil}})B_x(t) \tag{4.3}$$

and the hydrodynamic (damping) torque

$$T_{\mathrm{H}} = -\gamma \frac{d\Psi_{\mathrm{coil}}}{dt}. \tag{4.4}$$

Here, the drag coefficient $\gamma = \kappa V \eta \partial$ is determined by the coil shape factor [Tirado84] κ, the total volume of the coil $V = \pi R_{\mathrm{ext}}^2 L$ with length L, and the effective viscosity of the medium η. The optional factor ∂ accounts for a superlinear behavior of the damping torque as a function of the angular velocity [Pawasche09]. The Cartesian components of the uncompensated magnetic moment of the coil are $M_x = M\cos\Psi_{\mathrm{coil}}$, $M_y = M\sin\Psi_{\mathrm{coil}}$ (see inset of Fig. 4.3b). The magnitude of the uncompensated magnetic moment in a magnetic stripe of width W and thickness T, which is a part of a cylindrical surface with radius $R = (R_{\mathrm{ext}} + R_{\mathrm{int}})/2$ and central angle 2α (see inset of Fig. 4.3b), is $M = 2M_s RTW \sin\alpha$, where M_s is the saturation magnetization. The magnitude of the applied magnetic field acquires the form factor $\mathrm{FF}(t) = \frac{\zeta}{5}\sum_{n=0}^{4}\cos^{2n}(\omega_{\mathrm{mag}}t + \varphi)$ due to the specific profile of the magnetic field used for the excitation (Fig. 4.5). Its rotation is described by the harmonic evolution of the Cartesian components of the applied magnetic field: $B_x(t) = B_0\mathrm{FF}(t)\sin(\omega_{\mathrm{mag}}t + \varphi)$, $B_y(t) = B_0\mathrm{FF}(t)\cos(\omega_{\mathrm{mag}}t + \varphi)$. This leads to a magnetic torque from eq. (4.3) of the form

$$T_M(t) = MB_0\mathrm{FF}(t)\sin(\omega_{\mathrm{mag}}t + \varphi - \Psi_{\mathrm{coil}}). \tag{4.5}$$

A nonlinear nature of the dynamics of the coil is implied by the presence of Ψ_{coil} in the argument of the trigonometric function in eq. (4.5). The time-dependent form-factor FF(t) in the magnetic torque (4.5) represents a parametric excitation of the coil. Plugging eqs. (4.4) and (4.5) into eq. (4.1), we are left with the equation of motion:

$$I\frac{d^2\Psi_{\mathrm{coil}}}{dt^2} = MB_0\mathrm{FF}(t)\sin(\omega_{\mathrm{mag}}t + \varphi - \Psi_{\mathrm{coil}}) - \gamma\frac{d\Psi_{\mathrm{coil}}}{dt}\ . \tag{4.6}$$

The parameters used for calculating the plots for Fig. 4.5d–f are as follows: $m = 5.02 \times 10^{-11}$ kg, $R_{\mathrm{int}} = 30$ µm, $R_{\mathrm{ext}} = 37$ µm, $L = 38.5$ µm, $\eta = 1.002 \times 10^{-3}$ Pa · s, the factor ∂ is 0.625 for $\omega_{\mathrm{mag}} \leq 250°\ \mathrm{s}^{-1}$, increases from 0.625 to 1.0 in the range $250°\ \mathrm{s}^{-1} \leq \omega_{\mathrm{mag}} \leq 300°\ \mathrm{s}^{-1}$ and is 1.0 for $\omega_{\mathrm{mag}} \geq 300°\ \mathrm{s}^{-1}$, $M_{\mathrm{s}} = 480$ kA/m, $T = 5.0$ nm, $W = 7.0$ µm, $\sin\alpha = 0.0226$ and $\varphi = \pi/2$.

Equations of motion with and without inertia are considered. In agreement with the classical work [Purcell77], the motion of the coil can be described neglecting inertia at low Reynolds numbers. Although the model without inertia allows for simulating the dynamics of the coil, the physical picture based on the balance of

the torques acting on the coil is not accessible in this simplified model. For this reason, the model with inertia is investigated in [Smith11]. Using this model of motion, the trajectories observed in the experiment, Fig. 4.5a–c, can be recreated theoretically in Fig. 4.5d–f, respectively. The model also reveals other subtleties going from rotational ($\omega_{mag} \leq 250°\ s^{-1}$) to the OLR ($\omega_{mag} \geq 300°\ s^{-1}$) motion, which are hardly seen experimentally.

The frequency region of a transition from rotational, Fig. 4.6a, to OLR motion, Fig. 4.6d, is theoretically explored in Fig. 4.6. When ω_{mag} slightly exceeds $250°\ s^{-1}$, the motion of the coil consists of periods, where it performs rotation (accompanied by relatively weak oscillations) interrupted by "hiccups" representing back-and-forth motions of the coil (seen as dips in the upward slope of plots in Fig. 4.6b,c). They become more frequent as ω_{mag} increases until the motion is comprised only of "hiccups." At this point, the coil has entered the OLR regime. The origin of the "hiccups" is found in the balance between the magnetic and damping torques, which is easily traced in the model with inertia (see below). As follows from the value of the scaling factors in Fig. 4.6 (8,000 for $T(\Psi_{coil}, t)$), the magnetic and damping torques in eq. (4.2) compensate each other to a high extent.

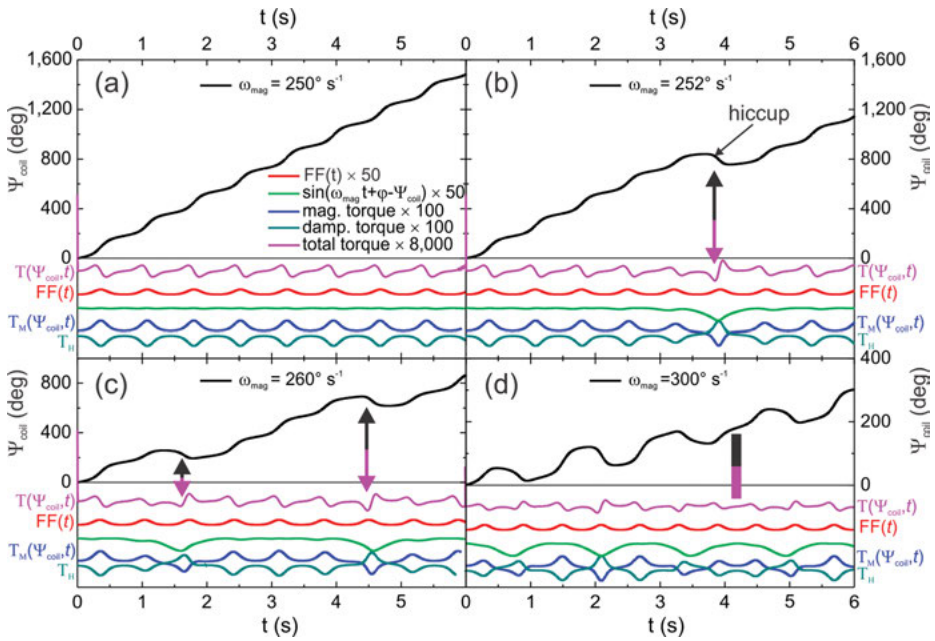

Fig. 4.6: Origin of a transition in the coil dynamics. (a) $\omega_{mag} = 250°\ s^{-1}$; (b) $\omega_{mag} = 252°\ s^{-1}$; (c) $\omega_{mag} = 260°\ s^{-1}$; (d) $\omega_{mag} = 300°\ s^{-1}$. Arrows and a vertical bar are explained in the text. Different scaling factors are used for magnetic and damping torques (×100) compared to the total torque (×8,000) (from [Fomin11]).

On the basis of the parametric magnetic excitation in combination with the nonlinear dynamics, a quantitative explanation of the experimentally observed behavior of radial-magnetized microhelix coils is provided: a rotation at lower frequencies ($\omega_{mag} \leq 250° \text{ s}^{-1}$) and an OLR motion at higher frequencies ($\omega_{mag} \geq 300° \text{ s}^{-1}$). A closer comparison of the dynamics obtained theoretically to the dynamics observed experimentally demonstrates that the coil shape factor κ in the drag coefficient γ increases from 0.173 for lower frequencies to 0.276 for higher frequencies, implying a dependence on the coil angular velocity. At lower frequencies, the system undergoes a periodic pulsed torque and therefore performs a rotational motion (accompanied by relatively weak oscillations). The OLR motion at higher frequencies originates from a periodic sequence of pairs of positive and negative pulses of the total torque, which produce swings of the coil back and forth [Fomin11].

This observation confirms the popular approximate derivation [Helgesen90, Purcell77] of the dynamics from the condition $T(\Psi_{coil}, t) = 0$. Nevertheless, the compensation is not complete. The remaining uncompensated torque, though small, governs the specific pattern of the coil dynamics, which can be explained by virtue of inertia in the system. The rotation accompanied by oscillations originates from a periodic sequence of positive and negative pulses of the total torque (Fig. 4.6a). The jumps of the coil in the direction opposite to the direction of rotation occur when a pair of negative pulses of the uncompensated torque acts on the coil consecutively (labeled with arrows in Fig. 4.6b, c). For $\omega_{mag} = 300° \text{ s}^{-1}$, pairs of positive and negative pulses of the total torque act in a sequence, producing the back-and-forth swings of the coil, which are only rarely interrupted by a combination of a positive and a negative pulse of the total torque (labeled with a vertical bar in Fig. 4.6d), which leads to a slight pure rotation. At this point, there are no longer clearly manifested periods of the rotation at all: the coil has entered the OLR regime. A close-up view of the torques at the "hiccup" regions in the transition of the coil dynamics is given in Fig. 4.7.

An insight into the nonlinear dynamics of the coil with parametric excitation is provided by plotting the phase trajectories in the phase plane [Tabor89] ($d\Psi_{coil}/dt$, Ψ_{coil}) (Fig. 4.8b–d). The regime of rotation (accompanied by weak oscillations) is represented by an oscillating phase portrait (see black curves $\omega_{mag} = 250° \text{ s}^{-1}$ in all panels). Every back-and-forth motion of the coil is represented by a loop in the phase space. An increase in ω_{mag} leads to a decrease of the angular separation between the loops, δ (inset of Fig. 4.8b). This is typical of the transition between two regimes of the coil dynamics. For $\omega_{mag} = 270° \text{ s}^{-1}$ and $280° \text{ s}^{-1}$, a periodic pattern of the envelope of the minima and maxima of the loops is manifested (Fig. 4.8c). At $\omega_{mag} = 300° \text{ s}^{-1}$, different loops begin to touch each other, characteristic of the OLR regime (Fig. 4.8d). The sequences of interpenetrating loops, which emerge for higher ω_{mag} (Fig. 4.8d), resemble a phase portrait of a driven oscillator.

In summary, a straightforward method has been put forth for creating helical coil structures with a number of different magnetic states: radial, corkscrew and hollow-bar magnet. In order to experimentally confirm the magnetization configurations, the

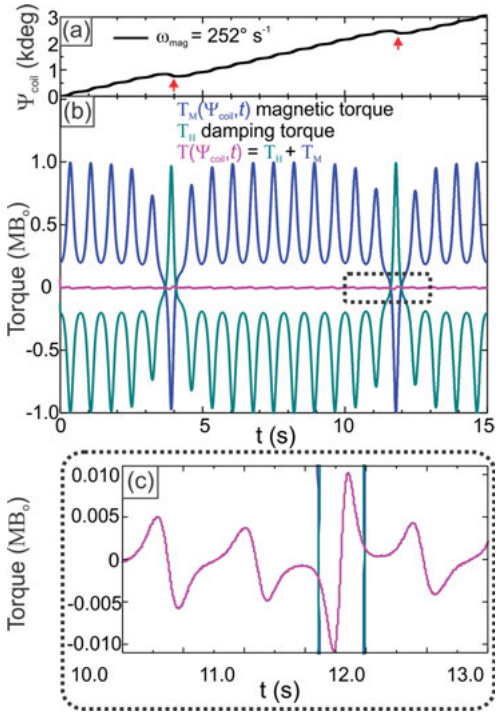

Fig. 4.7: Dynamics of the coil. (a) Trajectory of the coil exposed to the magnetic field with excitation frequency $\omega_{mag} = 252° \text{ s}^{-1}$. (b) Magnetic torque ($T_M$) and damping torque ($T_H$) are shown. The resulting total torque $T(\Psi_{coil},t) = T_M(\Psi,t) + T_H$ (magenta curve) is very close to zero as it is expected for microobjects moving in a viscous medium at low Reynolds number. (c) A close-up of $T(\Psi_{coil},t)$ reveals a deviation of the resulted torque from zero, which can be followed in the model accounting for inertia. The "hiccup" in total torque directly correlates to a transition from rotational to oscillatory motion, marked by red arrows in (a) (from [Fomin11]).

response of the coils to an alternating external magnetic field is explored. The dynamical behavior of the coils with different magnetizations experience unique features; for instance, radial-magnetized coils respond to an external field through a directionally deterministic motion. The experimental results are confirmed theoretically [Smith11], and three distinct dynamical regimes are identified: a rotational region when $\omega_{mag} < \omega_{mag}^{transition}$, a transitional region when $\omega_{mag} \approx \omega_{mag}^{transition}$ and an OLR region when $\omega_{mag} > \omega_{mag}^{transition}$.

The continuously distributed macroscopic magnetic moment of the microhelix coils resembles that of the discrete spin patterns of helimagnetic materials. Given that, a magnetic toroidal moment [Ederer07] can be generated by a ring-like arrangement of magnetic dipoles [VanAken07] (as shown in Fig. 4.1), the self-rolled magnetized microhelices provide a technique for its implementation [Smith11], thus allowing for experimental investigations on this novel type of multiferroic material. It has been

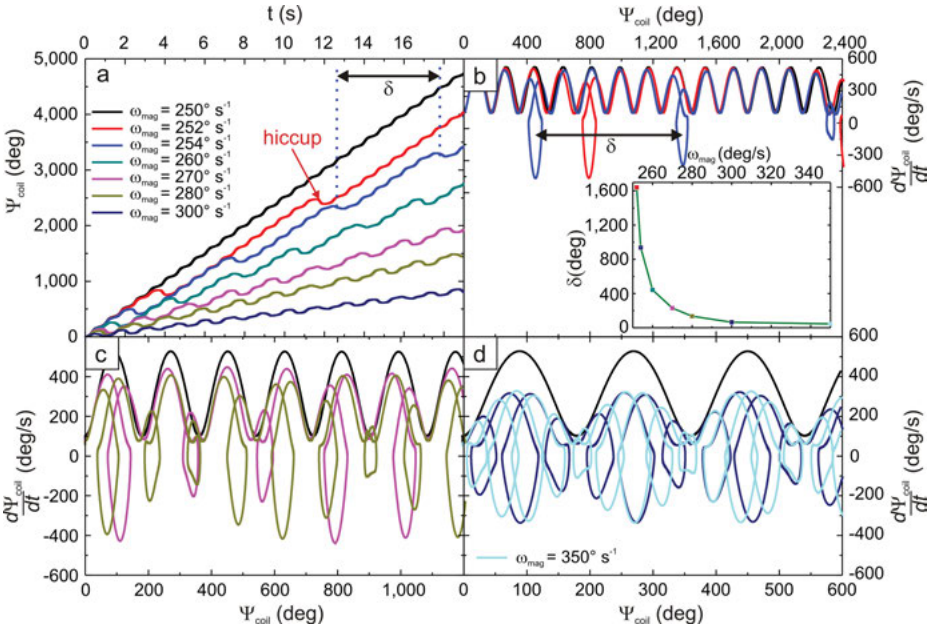

Fig. 4.8: Transition and phase portraits of coil dynamics. (a) Detailed dynamics of a coil transition from rotational to OLR motion over the transition frequency region ($250° s^{-1} < \omega_{mag}^{transition} < 300° s^{-1}$). Phase portraits ($d\Psi_{coil}/dt$ versus Ψ_{coil}) of the coil dynamics for (b) $\omega_{mag} = 252° s^{-1}$ and $254° s^{-1}$; (c) $\omega_{mag} = 270° s^{-1}$ and $280° s^{-1}$; (d) $\omega_{mag} = 300° s^{-1}$ and $350° s^{-1}$ – in all panels in comparison with $\omega_{mag} = 250° s^{-1}$. Inset to panel (b): Angular separation (δ) between loops versus the magnetic field frequency (ω_{mag}) (from [Smith11]).

shown theoretically and experimentally that diverse nontrivial topologic effects occur due to a special geometry of spin and magnetic textures in curved magnetized microarchitectures [Pylypovskyi15, Nord15, Streubel16, Krtavchuk16, Volkov19]. In addition, due to their particular deterministic motion, the radial-magnetized helical coils offer practical applications in microrobotics and roving sensors acting in fuel-free environments, such as in biomedicine.

4.2 Dynamics of a deformable microcoil: asymmetric drag in oscillatory motion

Asymmetry of magnetic objects in a fluid under an oscillating magnetic field leads to a wealth of nonequilibrium dynamics phenomena including a novel ratchet effect without an asymmetric substrate. These nonlinear dynamics are explained in the framework of the Stokes' model by a drag coefficient, which depends on the direction of motion [Fomin13].

Nonlinear dynamics imply various regimes of motion. Some examples of these regimes include laminar versus turbulent flows of a liquid [Feynman63] or synchronous versus asynchronous rotations of molecules in a liquid crystal driven by a rotating magnetic field [Migler91]. One of the types of nonlinear dynamics is the ratchet effect arising due to the asymmetry of the potential, for example, owing to the interaction with substrate [Engel03, Tierno08, Tierno10], or the asymmetry of the drive or of the surrounding media [Reichhardt05, Reichhardt06, Cole06, Tierno07] without asymmetric substrates. In contrast to the aforementioned reasons, analysis in [Fomin13] shows that a ratchet effect can occur due to asymmetry of the dissipation, owing to the shape of a system. Moreover, transitions between different regimes of motion are due to external influences, that is, interaction with the surrounding media and applied fields. A dependence of the drag coefficient on the direction of motion, due to the asymmetry of the object's shape, readily explains the nonlinear behavior in the presence of a periodic driving force. This explanation is general and is independent of the size of the object and the physical mechanism of the directional dependence of the drag coefficient.

In contrast to the non-linearity of the drag torque as a function of the angular velocity developing for a rotationally asymmetric object at high Reynolds numbers, there are two possible physical mechanisms underlying the directional dependence of the drag coefficient in the Stokes' regime at low Reynolds numbers. One is related to nonrigidity of the moving object leading to its rotationally asymmetric shape, while another is pertinent to the motion of a chiral body immersed in a bounded fluid. Experimental verification is provided to the applicability of the theoretical model [Fomin13] for two systems, a nonrigid magnetic microcoil and a chiral magnetic macroobject immersed in a bounded fluid.

Consider motion of an object carrying a magnetic moment $\mathbf{M}(t)$, in a viscous medium, which is subject to a rotating external magnetic field $\mathbf{B}(t; \omega_{\mathrm{mag}})$, with frequency ω_{mag}. The magnetic moment tends to align to the magnetic field. The position of the object at any given time is characterized by the angle $\Psi_{\mathrm{obj}}(t)$ between $\mathbf{M}(t)$ and an axis in the plane, where $\mathbf{B}(t; \omega_{\mathrm{mag}})$ rotates. The resulting time-dependent driving torque is $T_{\mathrm{M}}(\Psi_{\mathrm{obj}}, t) = F\sin(\omega_{\mathrm{mag}}t - \Psi_{\mathrm{obj}})$, where F is a product of the amplitudes of the magnetic moment and the magnetic field. Rotational dynamics of the object with the moment of inertia I under the action of the driving magnetic torque $T_{\mathrm{M}}(\Psi_{\mathrm{obj}}, t)$ and the drag torque $T_{\mathrm{D}}(d\Psi_{\mathrm{obj}}/dt)$ is governed by the equation of motion (4.1), which is represented here in the form

$$I\frac{d^2\Psi_{\mathrm{obj}}}{dt^2} = T_{\mathrm{M}}(\Psi_{\mathrm{obj}}, t) - T_{\mathrm{D}}(d\Psi_{\mathrm{obj}}/dt). \tag{4.7}$$

The system may reveal a uniform-in-time rotation (*linear regime*), synchronized to the driving torque, with a phase shift φ: ${\Psi^{\mathrm{lin}}}_{\mathrm{obj}}(t) = \omega_{\mathrm{mag}}t - \varphi$. The linear regime is possible only when the frequency ω_{mag} is lower than a certain transition frequency ω_{T} [Cebers06]: $\omega_{\mathrm{mag}} \le \omega_{\mathrm{T}} = \frac{F}{\kappa V\eta}$, where the parameters in the denominator are

determined in eq. (4.4). At the transition frequency ω_T, the system enters a *nonlinear regime* characterized by back-and-forth motions [Cebers06, Sudo06, Zhang08, Bermudez09, Ranzoni10, Smith11, Fomin11] (see the previous section). For a chiral object, there are *different* shape factors depending on the direction of motion, κ_{CW} for clockwise (CW) and κ_{CCW} for counterclockwise (CCW) rotational motion. Therefore the drag torque is modified in a time-dependent way, which is mediated by the dependence of the shape factor κ on the *sign* of the angular velocity [sgn $(d\Psi_{obj}/dt)$]:

$$T_D \frac{d\Psi_{obj}}{dt} = \kappa \left[\operatorname{sgn} \frac{d\Psi_{obj}}{dt} \right] V\eta \frac{d\Psi_{obj}}{dt}, \tag{4.8}$$

where V is the volume of the object and η is the dynamic viscosity of the environment. In the systems considered below, the Reynolds number for the macroscopic object at the highest angular velocity $d\Psi_{obj}/dt = 0.5$ kdeg/s reaches it maximal value ~ 1 at the most distant points from the rotation axis, and for the microhelix structure, it constitutes ~ 10^{-4}, which makes it reasonable to assume the regime of linear drag force.

The dynamics of a chiral macroobject possessing such a direction dependent, but velocity independent, drag coefficient is investigated theoretically and experimentally. The investigated object consists of three NdFeB magnets ($1 \times 1 \times 3$ mm^3; weight = 22 mg) glued together in a Z-like configuration [Fomin13]. The object is rotated about the magnetic field (of a rotating magnet below the sample) perpendicular to the object's plane and passing through the geometrical center of the middle magnet. Due to the asymmetry of the object, the shape factor for the CW (κ_{CW}) direction of motion is significantly different compared to that for the CCW direction (κ_{CCW}). The experimental setup consists of the object placed in an oil-filled Petri dish positioned ~ 15 cm above a rotating magnet on a motor, which can be set to the desired rotational speeds. The magnitude of the kinematic viscosity for the oil is 30 mm^2/s (at 40 °C), and the density of the oil is 900 kg/m^3. The magnetic field, at the height of the Petri dish, is selected to be 0.35, 0.65, 0.8 and 1.15 mT at maximum. The rotations of the motorized magnet are performed in plane parallel to that of the magnetic macroobject (similarly to a typical stirring-rod setup).

The macroobject is chiral, that is, it does not have *mirror symmetry* about a plane that contains its rotational axis (Fig. 4.9a). Shape factors $\kappa_{CCW} = 672$ and $\kappa_{CW} = 139$ are derived from experimental data fitting (see below). In this case, we obtain $\omega_T(\kappa_{CCW}) < \omega_T(\kappa_{CW})$, with $\omega_T(\kappa_{CCW}) = 123$ deg/s and $\omega_T(\kappa_{CW}) = 596$ deg/s. In the course of the theoretical simulations of the dynamics of the macroobject, κ_{CW} is kept constant and the object becomes more and more asymmetric by increasing κ_{CCW} from 139 (= κ_{CW}) to 672. Initially, when $\kappa_{CCW} = \kappa_{CW}$, trajectories characterizing the motion of the object (black and blue lines in Fig. 4.9a) are mirror symmetric with respect to the time axis and independent of the frequency ω_{mag} of the magnetic field. This holds for both the

linear and the nonlinear (Fig. 4.9a) regimes of motion. When the object becomes asymmetric, a significant difference between CCW and CW trajectories emerges.

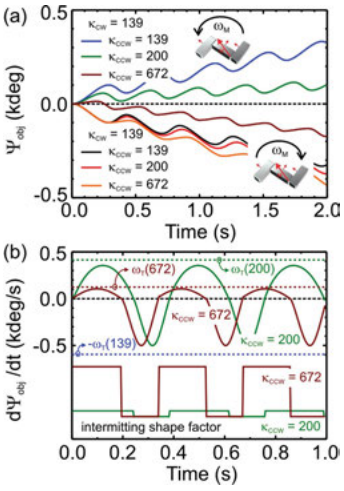

Fig. 4.9: (a) Theoretical dynamics of a magnetized object with chiral geometry, in a viscous medium, excited at $|\omega_{mag}| = 1.0$ kdeg/s by a magnet rotating in the clockwise (CW) or counterclockwise (CCW) direction. (b) Theoretically revealed time evolution of $d\Psi_{obj}/dt$ for $|\omega_{mag}| = 1.0$ kdeg/s, with an intermittency of the direction-dependent (for the CW and CCW motion) shape factor (from [Fomin13]).

Simulations start with the magnetic field of 0.35 mT. The calculations for $\omega_{mag} = \pm 0.5$ kdeg/s and 1.0 kdeg/s (Fig. 4.9) reveal the following common feature of the shape factor. For CCW excitation at $|\omega_{mag}| > \omega_T(\kappa_{CCW})$, the system is in the nonlinear regime revealing back-and-forth motion (Fig. 4.9a, upper part). Its rotational velocity increases until it reaches the maximum (Fig. 4.9b) close to the transition frequency $\omega_T(\kappa_{CCW})$. Further on, the velocity decreases and the motion deviates significantly from the linear regime of rotation, resulting in back-and-forth motions; that is, at a certain moment, the velocity $d\Psi_{obj}/dt$ changes its sign from positive to negative (Fig. 4.9b). This causes the system to simultaneously acquire a *smaller* shape factor κ_{CW} and continue to move in the CW direction until its negative velocity reaches the transition frequency $-\omega_T(\kappa_{CW})$. At this instant, the negative velocity starts to increase. A driving torque forces the system to rotate in the CCW direction, so that the velocity $d\Psi_{obj}/dt$ further increases and, at a certain moment, again changes its sign (Fig. 4.9b), now from negative to positive with a *larger* shape factor κ_{CCW}. As a result, the shape factor as a function of time manifests *intermittent* behavior.

For frequencies $|\omega_{mag}| > \omega_T(\kappa_{CW})$, the system is always in a nonlinear regime of motion. For CW excitation ($\omega_{mag} = -1.0$ kdeg/s), the motion (Fig. 4.9a, lower part) is only slightly affected by increasing κ_{CCW}. In contrast, for a CCW excitation ($\omega_{mag} = +1.0$ kdeg/s), the trajectories are strongly influenced by changing the value of κ_{CCW}. The maximal angular velocity, equal to $\omega_T(\kappa_{CCW})$, decreases inversely proportional to κ_{CCW}, while the minimal angular velocity always remains the same [equal to

$\omega_T(\kappa_{CW})$]. Therefore, even for the CCW excitation (ω_{mag} = +1.0 kdeg/s), starting from a certain magnitude of the shape factor κ_{CCW}, the overall angular displacement of the object is in the CW direction (Fig. 4.9b, upper part, curve for κ_{CCW} = 672). This is a hallmark of *a ratchet effect due to the strongly asymmetric drag*, and the corresponding average angular velocity becomes negative (Fig. 4.9b).

The motion of the chiral macroobject is an intermitting sequence of stages governed by two different shape factors. Its characteristics, for example, the *average angular velocity* (Fig. 4.10a) and the *average shape factor* (Fig. 4.10b), are controlled by the frequency of the magnetic field, ω_{mag}. As shown in Fig. 4.10a, for an object of asymmetric shape, at a given value of the CCW excitation frequency (e.g., ω_{mag} = + 0.5 kdeg/s), an increase of the value of κ_{CCW} (a stronger asymmetry) results in a transition from the linear regime of rotation to the nonlinear regime of back-and-forth motions, followed by the occurrence of the ratchet effect. As typically observed in the experiment, there is a transition between different regimes of motion with increasing ω_{mag} [Fomin13]. By making the selection of the intermittent κ for the object rotating CW and CCW, the experimental dynamics fits the theoretical prediction. For a symmetric object, the model with a single, direction-independent, shape factor is sufficient for interpreting the experimentally observed dynamics.

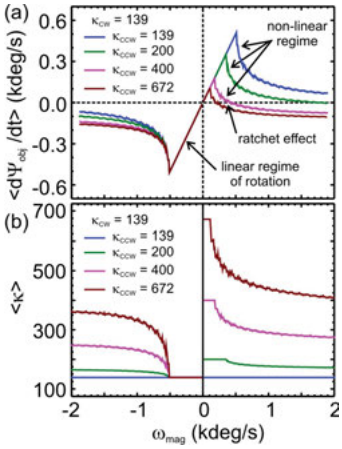

Fig. 4.10: Motion of the chiral macroobject. (a) $< d\Psi_{obj}/dt >$ as a function of ω_{mag}. (b) $< \kappa >$ as a function of ω_{mag} (from [Fomin13]).

It is known from experiment (see, e.g., Fig. 4.6 in [Migler94]) that even in the linear drag regime, the shape of a chiral object *may be* dependent on the direction of rotation. This finding *does not* contradict the conclusion of Happel and Brenner ([Happel83], p. 172) (where it is stated that for a rigid body in an *unbounded fluid* in the linear regime of rotation, the rotation tensor is symmetric) because *the body is not rigid*, that is, it is not identical to itself when it rotates CW and CCW. This mechanism is relevant to explain the asymmetry of the shape factor of a deformable microcoil [Smith11, Fomin11].

Asymmetry of a nonlinear drag can, in principle, result in a similar observation. To clarify this point, additional measurements of the transition frequencies, ω_T, are performed at different values of the applied magnetic field for the chiral macroscopic object (Fig. 4.11). The experimental data are fitted to the model assuming the same values of κ_{CW} and κ_{CCW} independently of the applied magnetic field. By making the earlier-described selection of the intermittent κ for the object rotating CW (positive angular velocity; $\kappa_{CW} = 672$) and CCW (negative angular velocity; $\kappa_{CCW} = 139$), the experimental dynamics fit the theoretical prediction (Fig. 4.11). This clear agreement between the theory and experiment implies that rotationally anisotropic shape factors explain the experimental observation. In turn, this data confirm that a linear, rather than quadratic, drag is experienced by the chiral macroscopic object. This finding *does not* contradict the earlier-mentioned conclusion of ref. [Happel83], because the chiral macroscopic object does move in a *bounded fluid*, that is, it experiences different influences from the side of the bottom of an oil-filled Petri dish, when it rotates CW and CCW [Fomin13].

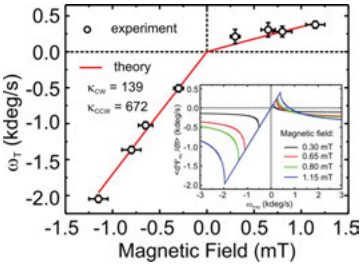

Fig. 4.11: Motion of the chiral macroobject. ω_T as a function of B. Theory (for $\kappa_{CW} = 139$ and $\kappa_{CCW} = 692$) and experiment compare well. Inset: $< d\Psi_{obj}/dt >$ as a function of B (from [Fomin13]).

Also a "classical" ratchet effect is demonstrated due to the directional asymmetry of the *potential*, which leads to a time-irreversible evolution of systems [Loutherback09, Balvin09]. A ratchet (gear and pawl) with a pronounced structural asymmetry is fabricated [Fomin13], and its rotation is investigated under an external magnet with excitation frequency $\omega_{mag} = 400$ deg/s. The ratchet is a curved plastic gear with two NdFeB permanent magnets (sizes $1 \times 1 \times 3$ mm^3; weight 20 mg). The ratchet is placed on oil in a Petri dish positioned 8 cm above a rotating motorized permanent magnet. It is important to indicate that the teeth of the gear do not touch the surface of the oil. The strength of the magnetic field at the height of the Petri dish is ~2 mT. Two series of experiments are performed. In the first series, the gear *without* the pawl is rotating with the same angular velocity in the CCW and CW direction. As the object is rotationally symmetric, its motion is observed to be independent of the excitation direction. On the contrary, when the pawl is engaged, the strongly asymmetric potential for rotation of the gear becomes relevant. The position of the pawl is chosen to forbid rotation of the gear in the CCW direction, but not to influence its CW motion. Therefore, a

pronounced asymmetry in the motion of the ratchet is visualized. Peculiarly, as predicted, when excited in the CCW direction, the ratchet is found to rotate in the CW direction.

The behavior of the average shape factor with increasing the CCW excitation frequency $|\omega_{mag}|$ (Fig. 4.10b) provides an explanation for the increase of the effective shape factor with increasing excitation frequency. As shown in the previous section, this is experimentally observed [Smith11] in the dynamics of radial-magnetized *microhelix coils* (Fig. 4.12). More specifically, a radial-magnetized microhelix coil with small structural asymmetry (Fig. 4.12a) is considered to be driven by an external magnetic field with excitation frequency ω_{mag}. The dynamics of this coil is theoretically mapped with the angular coordinate Ψ_{coil} assuming again *different* shape factors for CW and CCW motion (Fig. 4.12b) about the coil axis. However, both parameters remain constants, independent of the absolute value of ω_{mag}. The experiment [Smith11] implies that the transition region between different regimes of motion (rotational and OLR) is between $\omega_{mag} = 250°\ s^{-1}$ and $300°\ s^{-1}$. By selecting an intermittent κ, the theoretical model explains the experimental dynamics. The motion on a long-time scale can be described by introducing an average shape factor $<\kappa>$ calculated through a probability of either CW or CCW motion occurring (Fig. 4.12c). The coil average angular velocity $<d\Psi_{coil}/dt>$ as a function of ω_{mag} is *linear* for $\omega_{mag} < 250°\ s^{-1}$ and *decaying* for $\omega_{mag} > 250°\ s^{-1}$ (Fig. 4.12d).

4.3 Star-shaped thermoresponsive magnetic microrotors

An intermittent shape factor leads to a dramatic qualitative difference between the regimes of dynamics of a chiral object for both directions of rotation of the magnetic field. This is distinct from the case of symmetric dynamics for both directions of excitation, revealed by a symmetric object. The fundamental asymmetric dissipation in oscillative motion is of significance not only for macrosystems, but also for obtaining insight into the mechanical properties of a wide class of driven microobjects, including magnetic microsystems, biological cells with magnetite [Erglis07] and magnetotactic bacteria [Neuman08, Blakemore75]. Manipulation of magnetic particles with a rotating magnetic field provides a straightforward technique to wind up biological molecules and study their structural properties [Midgley09] by following the rotational dynamics of the microobjects in fluids.

Using materials with properties similar to those of cells and microorganisms together with innovative fabrication methods, soft and smart microrobots can be developed, with increased adaptability and flexibility toward in vivo applications. These tiny robots are designed to carry out difficult tasks, such as noninvasive microsurgery, diagnosis and therapy in complex environments, including viscous media and intricate channels. Moreover, the novel property of the soft materials to

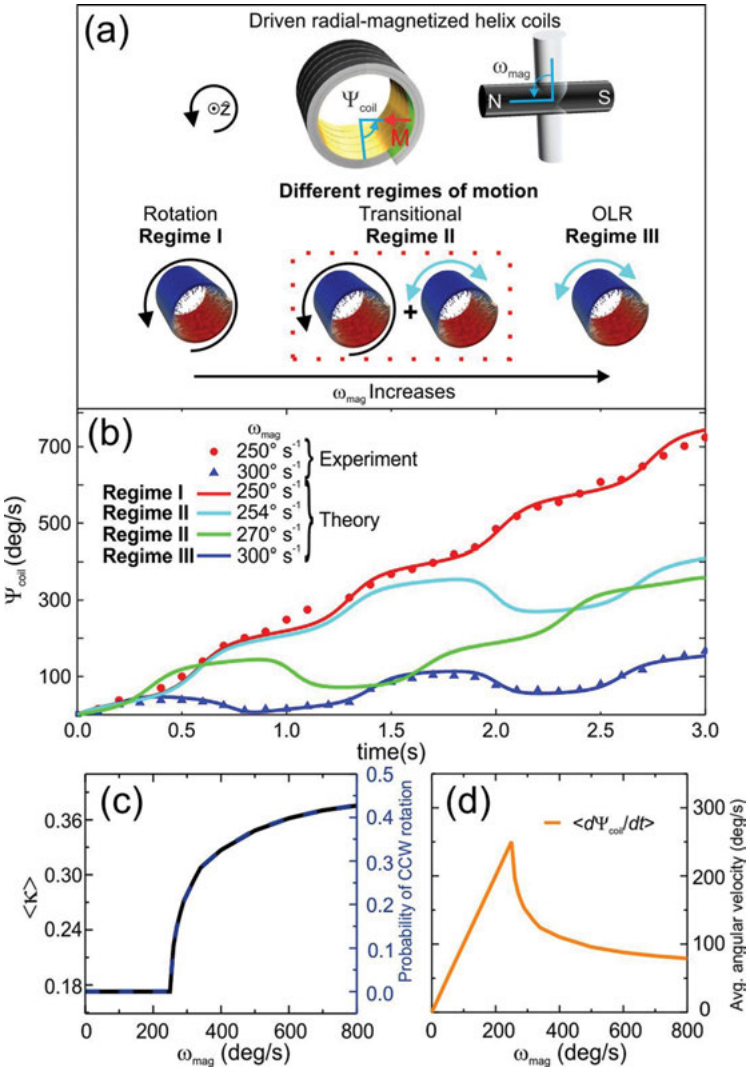

Fig. 4.12: (a) A microhelix coil reveals complex dynamics when nonlinearly excited by a rotating magnet. (b) Time evolution of $d\Psi_{coil}/dt$ for two values of ω_{mag} with an intermittency of the direction-dependent shape factor (CW and CCW motion). (c) The average shape factor calculated as a function of ω_{mag}. (d) $< d\Psi_{coil}/dt >$ as a function of ω_{mag} (from [Fomin13]).

respond to stimuli has paved the way for the creation of reconfigurable and smart microrobots with both sensing and actuation capabilities. As a representative case [Medina18], soft flower-shaped microrotors are able to respond to a magnetic field as well as to temperature changes. These microrotors, as depicted in Fig. 4.13a, are composed of temperature-responsive polymer poly(*N*-isopropylacrylamide)-AB with

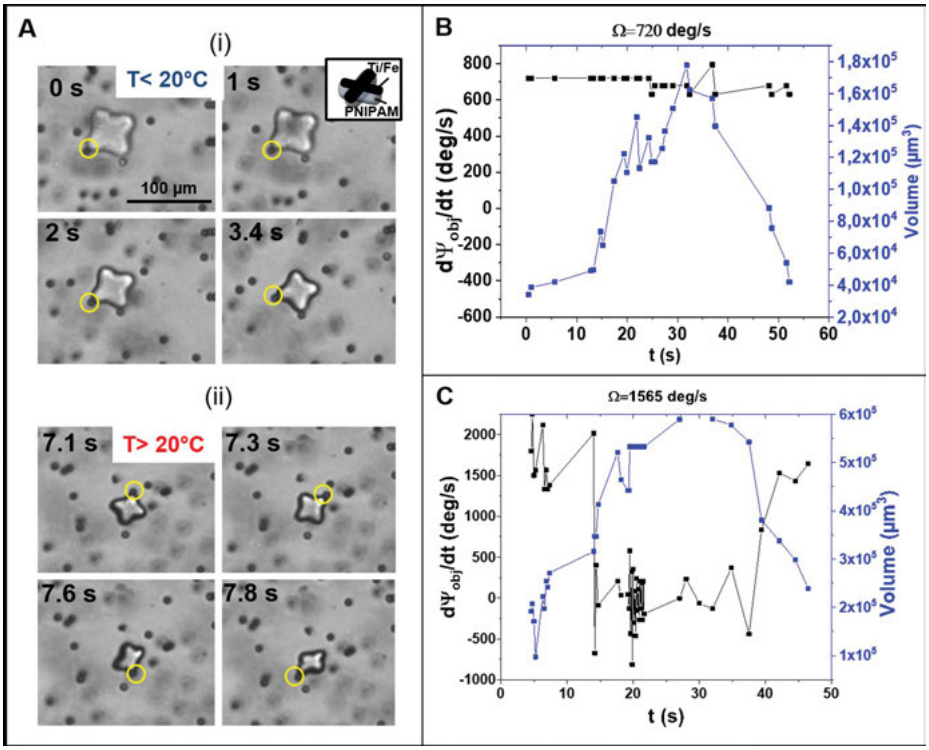

Fig. 4.13: Flower-shaped thermoresponsive magnetic microrotor. (a) In the cool, swollen state, the microrotor does not rotate (i), whereas in the warm, shrunk state it rotates (ii) according to the pulsed magnetic field of a rotating permanent magnet. Angular velocity and volume of microrotors as a function of time with (b) lower frequency of 720 deg/s of the pulsed applied magnetic field and (c) higher frequency of 1,565 deg/s (from [Medina18]).

a thin magnetic coating of 3 nm Ti and 10 nm of Fe on one side, deposited by the angled electron beam evaporation. The deposition of the thin iron layer makes the microstructures responsive to an external magnetic field. The structures can be rotated in the solution, if a permanent magnet is rotated near the sample. This can be used for improved mixing and also directional motion of the microrotors, when the rotating magnetic field is changing its rotation direction. An interesting phenomenon is observed, when in addition to the magnetic rotation, temperature cycles are applied: when the structures swell due to cooling, their volume increases and they seem to drop out of the rotation.

A closer look at the behavior of the flower-shaped microrotors reveals the fact that it does not stop completely, when the volume increases, but rather switches to an oscillating motion. As the volume of the microstructure increases due to swelling, the friction also increases and, at a certain volume, the microrotor cannot

follow the rotational motion so that only oscillations are left. In fact, in the rotational state, the oscillations are also present, but latent. Also, the critical volume, at which the micromotor drops out and does not follow the rotation, decreases with increasing the applied magnetic field frequency, as shown in Fig. 4.13b,c.

The image sequences in Fig. 4.13a illustrate the observations. In the upper four images, the microstructure does not rotate, but oscillates, even though an external field is continuously applied. Once the structure is heated and thereby shrinks, it starts rotating, as can be seen in the lower image series in Fig. 4.13a. The yellow circles point at a microparticle, which is attached to one of the tips of the star-shaped structure. The dynamics of the flower-shaped thermoresponsive structure is modelled following [Fomin11, Fomin13]. Consider the motion of a "flower" carrying a magnetic moment $\mathbf{M}(t)$, in a viscous medium, which is subject to a pulsed magnetic field $\mathbf{B}(t;\Omega)$ of a permanent magnet rotating with frequency Ω. The magnetic moment tends to align to the magnetic field. The position of the object at any given time is characterized by the angle $\Psi_{\text{obj}}(t)$ between $\mathbf{M}(t)$ and an axis in the plane, where $\mathbf{B}(t;\Omega)$ rotates.

In the systems under consideration, the Reynolds number constitutes $\sim 2\times10^{-2} \ll 1$. In the low-Reynolds-number regime, the torque equation is represented in the form:

$$T_{\text{D}}\frac{d\Psi_{\text{obj}}}{dt} = F_{\sin}(\Omega t - \Psi_{\text{obj}}) \tag{4.9}$$

Moreover, the smallness of the Reynolds number makes it reasonable to assume the regime of linear drag force. For the thermoresponsive "flower," there are *different* values of volume depending on the temperature that varies with time. Therefore, the drag torque is modified in a time-dependent way, which is mediated by the dependence of the volume of the "flower" $V(t)$ on time:

$$T_{\text{D}} = \kappa\, V(t)\eta, \tag{4.10}$$

where κ is a form factor of the "flower" and η is the dynamic viscosity of the environment. The system may reveal a uniform-in-time rotation (*linear regime*), synchronized to the driving torque, with a phase shift φ: ${\Psi^{\text{lin}}}_{\text{obj}}(t) = \Omega t - \varphi$. The linear regime (in the case when F and V are constants) is possible, only when the frequency Ω is lower than a certain transition frequency ω_{T} [Cebers06]: $\Omega \le \omega_{\text{T}} = \frac{F}{\kappa V \eta}$. At the transition frequency ω_{T}, the system enters a *nonlinear regime* characterized by back-and-forth motions (see [Fomin13] as well as Fig. 4.14). The modeling of the dynamics of a "flower" in a pulsed magnetic field $\mathbf{B}(t;\Omega)$ of a rotating permanent magnet is performed by solving the nonlinear differential eq. (4.9) numerically with using the dependence $V(t)$ extracted from the experiment.

The simulations of the microrotor dynamics represented in Fig. 4.14a,b(c,d) are performed for the square-shaped change of the volume of the flower-shaped object

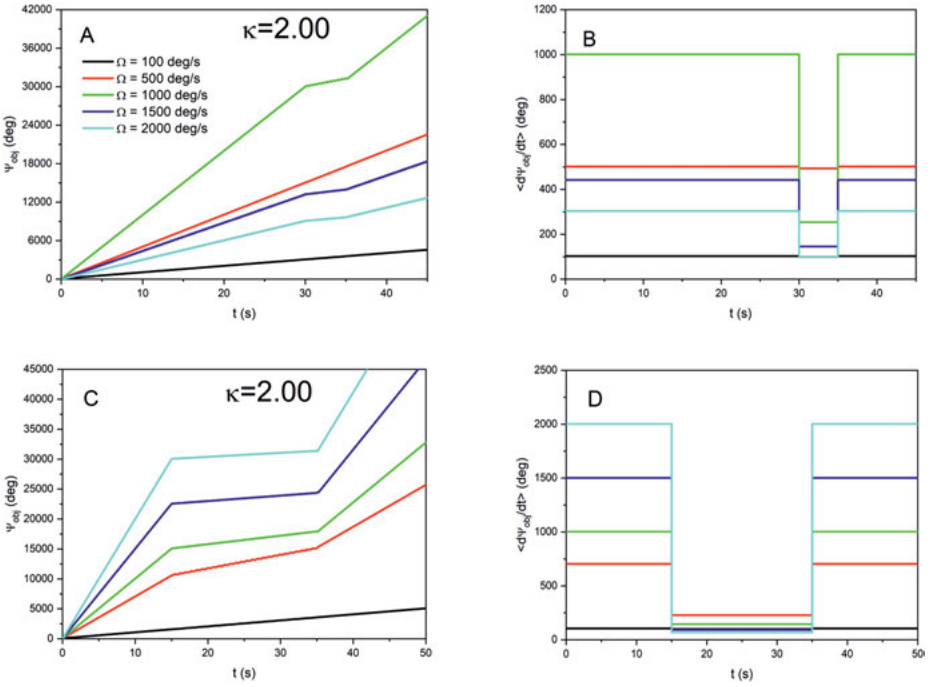

Fig. 4.14: Model calculations for the flower-shaped microrotors with a form factor $\kappa = 2$. Angle (a and c) and angular velocity (b and d) as a function of time, when a cycle of cooling and heating is applied, as described in the text and corresponding to experimental demonstrations in Fig. 4.13b,c (panels a,b from [Medina18]).

$V(t)$ from 74,000 μm^3 to 120,000 μm^3 in the interval from 30 to 35 s (15 to 35 s) and back to 74,000 μm^3. For $\Omega = 1{,}000$ deg/s, this change of the volume leads to a corresponding increase of the drag torque (4.10), which drives the dynamics from a linear regime to a nonlinear regime within the pulse duration, characterized by a dramatic reduction of the average rotational angular velocity.

In Fig. 4.13b, a lower frequency of 720 deg/s is applied, which keeps the flower-shaped microrotor in the linear regime throughout the whole volume modification. When the frequency is increased above the critical frequency, the microrotor enters the nonlinear regime as long as it increases in size (Fig. 4.14). This mechanism shows potential as a novel type of fine spatiotemporal control for actuators by the combination of the magnetic and thermal control as an example for multistimuli actuation.

The versatile control of soft microrobots by their ability to respond to multiple stimuli offers important advanced applications. In particular, the multiple inputs and their combinations can be used to demonstrate logic-gate behavior of the microrobots. There have been some attempts to demonstrate logic-gate behavior using

individual- or multiple-stimuli-responsive microrobots. Examples of multistimuli control mostly use the addition of magnetic nanoparticles or magnetic layers for the directional control of microrobots or magnetically driving robots in combination with a light-, pH-induced or thermal mechanism to reconfigure the shape or release an agent (see table 1 in [Medina18] for details).

5 Propulsion mechanisms of catalytic tubular micromotors

Within the recent advancements in micro- and nanorobotics [Ozin05, Mallouk09, Sanchez09, Sengupta12, Wang12], of particular importance are self-rolled catalytic micromotors, which exhibit self-propulsion in the presence of chemical fuels, such as hydrogen peroxide solutions [Mei08, Solovev09]. The smallest man-made jet engine (600 nm in diameter and 1 pg of weight) is synthesized based on self-rolling of heteroepitaxially grown layers [Mei08, Solovev09, Sanchez11]. Several applications of these catalytic micromotors have been proposed [Solovev12] and several geometries have been designed [Pumera11]. Bubble-free propelled tubular nanomotors (200 nm in diameter, grown of silica on silver nanowires by sol–gel chemistry) powered by an enzyme-triggered catalytic reaction using a naturally occurring compound, urea, as a biocompatible fuel render possible biomedical applications [Ma16b].

The energy needed to propel micromotors is based on the catalytic decomposition of the hydrogen peroxide fuel into molecular oxygen and water with the aid of the material, of which the tube is fabricated, platinum, as a catalyst. Some review papers summarize the different mechanisms that have been proposed for these active swimmers [Wang09, Sanchez09, Mirkovic10]. In the particular case of microtubular jets, the propulsion force originates from the generation of oxygen bubbles that are expelled from the tube [Mei08, Solovev09]. This mechanism makes microjets very interesting since, up to now, microtubular jets generate a higher propulsion force than nanorods, spherical Janus particles or microhelices, to name a few [Gao12]. In addition, they can navigate in biological media, which makes them potentially attractive for environmental and medical applications [Balasubramanian11]. Enhanced degradation of organic pollutants in water at small-scale environments underlies an important potential application of catalytic micromotors [Soler13].[2]

The development of these catalytic micromotors illustrates one of the first steps toward designing and powering small-scale robotic systems for applications in diverse fields, such as medicine or nanomanufacturing. Substantial efforts have been made toward demonstrating that these micromotors can develop useful tasks [Solovev12]. The present Chapter is devoted to a discussion of the propulsion mechanisms of these micromotors. A typical experimental realization of a self-rolled catalytic micromotor is provided in Fig. 5.1.

Microsystems combining diverse functionalities, like untethered motion, actuation and communication, are in demand for applications ranging from microrobotics to micro-/nanocargo delivery and teranostics in nanomedicine. To this end, a broad variety of components, such as microelectronic circuits, engines, actuators,

2 This paper counts 376 citations according to [Scholar20] (as of 30.09.2020).

https://doi.org/10.1515/9783110575576-005

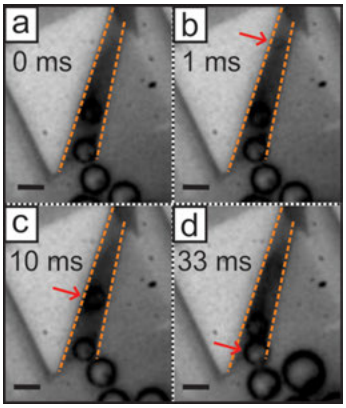

Fig. 5.1: Generation of an O_2 bubble inside of the tube in an aqueous solution of 1% H_2O_2 and 1% sodium dodecyl sulfate (SDS). (a) Aqueous solution fills the microtube from the smaller opening. (b) The inner surface of Pt catalyzes the decomposition of H_2O_2 fuel and, consequently, the generation of an O_2 bubble. (c) Bubble growth and movement to the larger opening of the tube. (d) The bubble is released. The dashed orange lines highlight the walls of the self-rolled tube. The red arrow shows the evolution of one single bubble inside of the tube. Scale bar 10 μm (from [Fomin14]).

power supplies, detectors and sensors, must be integrated on a single platform. Single-tube micromotors have been intensively explored and optimized toward their functionalization. However, the restricted room and accessibility provided by a single-tube micromotor impede integration of additional functional components. A more advanced microsystem designed and fabricated toward this goal is a motile twin-jet-engine microsystem (MTJEMS), which is based on two parallel self-rolled tubes [Mei11] and possesses three promising features due to its complex geometry. (i) The platform bridging the two tubular micromotors provides enough room for circuits and devices that enable versatile functionalities, in particular, a remote power supply, steering of the microsystem and chemical detection. (ii) Individual MTJEMSs can be addressed in a swarm, for example, by using radiofrequency. (iii) The MTJEMS generates more powerful propulsion and, by decreasing the stochastic spread of gas bubbles nucleation, growth, motion and expulsion from each micromotor, its locomotion obtains an enhanced stability. A flexible MTJEMS is fabricated, which consists of two catalytic tubular micromotors connected via a flat polymeric structure (Fig. 5.2a). Being driven by wireless power transfer, it is capable of controlled locomotion and actuation. A square coil that is integrated into the platform enables wireless energy transfer via inductive coupling of the transmitter coil with the catalytic micromotors (Fig. 5.2a). A local heating of one of the micromotors in a symmetric MTJEMS allows for a control over the direction of motion (Fig. 5.2b). Circular motion is achieved by maintaining the wireless energy transfer for several seconds. When the wireless power transfer is deactivated, the tubular engine cools down and the MTJEMS returns to a linear motion. Steering and turning the microsystem can be achieved by controlling the generation and expulsion rate of gas microbubbles from one of the two micromotors, which is realized by actively and remotely controlling the “on” and “off” states of the wireless energy transfer. For example, by applying different voltages at the transmitter coil, a complex trajectory of MTJEMS consisting of turning left, linear motion and turning right is achieved

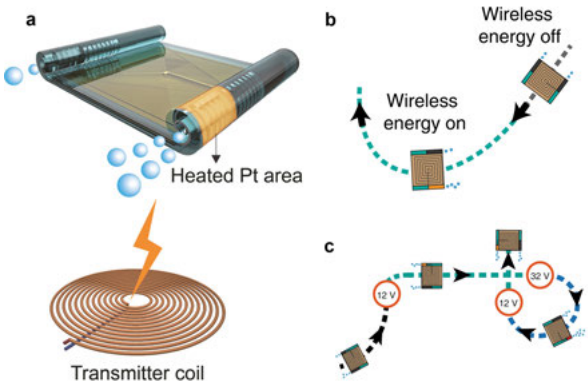

Fig. 5.2: Local heating effect via wireless energy transfer and locomotion of the MTJEMS. (a) Scheme of wireless energy transfer from the transmitter coil (shown in the bottom of the panel) to the receiver coil on board the MTJEMS. The area with Pt catalyst pads in one micromotor is heated, generating a higher expulsion rate of oxygen gas bubbles. (b) Schematic of the trajectory of a symmetric MTJEMS. Voltage at the transmitter coil is 12 V. (c) Schematic of a complex trajectory of an asymmetric MTJEMS for different voltages at the transmitter coil (indicated in circles). (Reprinted by permission from the Springer Nature Customer Service Centre GmbH: Springer Nature, Nature Electronics. A flexible microsystem capable of controlled motion and actuation by wireless power transfer, V. K. Bandari, Y. Nan, D. Karnaushenko, Y. Hong, B. Sun, F. Striggow, D. D. Karnaushenko, C. Becker, M. Faghih, M. Medina-Sánchez, F. Zhu, O. G. Schmidt © (2020) [Bandari20]).

(Fig. 5.2c). By integrating light emitting diodes and a thermoresponsive microarm in the platform, microrobotic grasp and release functions can be realized [Bandari20].

5.1 Theoretical models of propulsion of catalytic micromotors

In this section, theoretical ideas are overviewed concerning the self-propulsion mechanisms of the catalytic micromotors, which are prospective in robotics, biomedical engineering and environmental sustainability. We discuss the propulsion mechanisms of the catalytic microjet engines that are fabricated using rolled-up nanotech [Solovev12].

According to Newton's third law of motion and considering a steady motion at very low Reynolds numbers, the dynamics of the catalytic micromotor is governed by the mutual compensation of the driving force $\mathbf{F}_{\text{Driving}}$ and drag force $\mathbf{F}_{d,j}$ at any instant t:

$$\mathbf{F}_{\text{Driving}}(t) = -\mathbf{F}_{d,j}(t). \tag{5.1}$$

The drag force acting on the micromotor depends on its instantaneous speed $\mathbf{v}_j(t)$, the length L, the maximum radius $R_{\max}$, the semicone angle $\phi = \tan^{-1}\left(\frac{R_{\max} - R_{\min}}{L}\right)$ and the dynamic viscosity η of the fluid:

$$\mathbf{F}_{d,j}(t) = -\frac{2\pi\eta L \mathbf{v}_j(t)}{\ln\left(\frac{L}{b}\right) + c_1}, \tag{5.2}$$

where c_1 is defined by the geometry of the tube

$$c_1 = -\frac{1}{2} + \ln 2 - \frac{2-\xi\tan\phi}{2\xi\tan\phi}\left[\frac{2}{2-\xi\tan\phi}\ln\left(\frac{2}{2-\xi\tan\phi}\right) - \frac{2-2\xi\tan\phi}{2-\xi\tan\phi}\ln\left(\frac{2-2\xi\tan\phi}{2-\xi\tan\phi}\right)\right] \tag{5.3}$$

with $b = R_{\max} - \frac{L}{2}\tan\phi$ and $\xi = \frac{L}{R_{\max}}$ [Li15].

The nature of the driving force in eq. (5.1) is revealed within a few mechanisms of the self-propulsion that have been advanced in conjunction with available experimental evidence. In fact, they play different roles at different stages of the bubble dynamics (see Fig. 5.3). First, the geometric asymmetry of a tubular microjet leads to the development of a *capillary force*, which tends to propel a bubble toward the larger opening of the tube [Fomin14, Klingner17]. This *capillarity mechanism* leads to a force occurring when the oxygen bubble touches the inner wall of the tube, which gives rise to a movement of the bubble through its lumen. While the bubble continues growing by collecting oxygen, a fuel flow is induced [Sarkis15], which increases the pressure in the surrounding fluid near the larger opening of the tube and decreases it near the smaller opening. The resulting pressure difference leads to a propulsion of the micromotor with its smaller opening forward (i.e., against the direction of the bubble release). Second, due to the continuous production of oxygen the *bubble growth* process occurs at the larger opening of the tube, imposing a growth force governed by the Rayleigh–Plesset equation and displacing both the surrounding fluid and the micromotor [Manjare12, Manjare13]. Third, when the bubble detaches from the larger opening of the tube, the *bubble expulsion* mechanism emerges. A frequent release of bubbles from the tube causes a flow of the fluid opposite to the direction of the motion of bubbles. The propulsion of the micromotor is then caused by conservation of

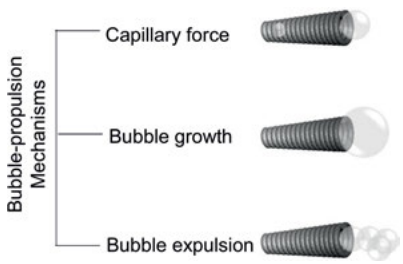

Fig. 5.3: Schemes of the bubble-driven propulsion mechanisms in a catalytic micromotor: capillarity, bubble growth and bubble expulsion, occurring at different stages of the bubble dynamics (after [Wrede20]).

momentum in the system that includes the motor, the bubbles and a surrounding fluid [Li11]. A numerical time-resolved model is presented for predicting the transition between unidirectional and overloaded motion of catalytic tubular micromotors (Ti/Fe/Pt self-rolled microtubes) in an aqueous solution of hydrogen peroxide [Klingner17]. A *combination* of three above-described propulsion mechanisms is shown to be needed for interpretation of the experimental evidence [Wrede20].

5.1.1 Capillarity mechanism

Real self-assembled tubular micromotors are as a rule asymmetric. The most common scenario is a geometric asymmetry of a micromotor: a deviation from an ideal cylindrical shape. In accordance with the typical experiment (Fig. 5.1), a micromotor is selected in shape of a conical tube (Fig. 5.4a). The dynamics of bubbles in the micromotor is schematically represented in Fig. 5.4. In a conical tube, the left R_l and right R_r radii of the spherical cups, which are constituents of the deformed bubble (Fig. 5.4c), are different. As a result, a capillary force occurs, which drives the bubble toward the larger opening of the tube, tending to decrease its surface

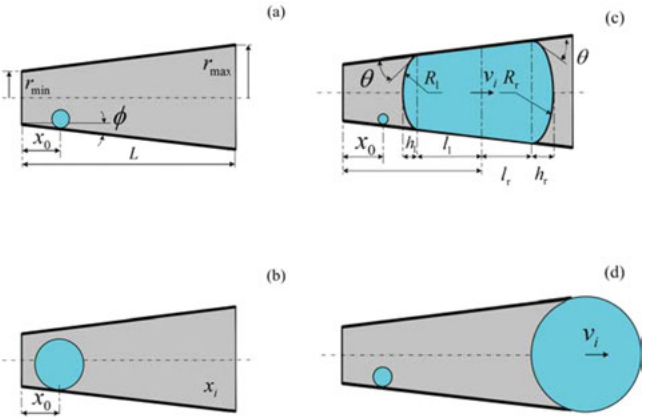

Fig. 5.4: Scheme of bubble dynamics in a conical micromotor. Gray (blue) area represents the fluid (the gas). (a) Geometric parameters of the tube are the length L, the radii of the smaller r_{min} and larger r_{max} openings, the semicone angle ϕ. The position of the bubble nucleation x_0 is eventually determined by an imperfection. (b) Growth of the bubble at the fixed position x_0. (c) Nucleation of the second bubble at x_0 and growth of the first bubble, which moves at speed v_i toward the larger opening. The bubble shape is geometrically described as two spherical caps (left and right) of radii R_l and R_r, and heights h_l and h_r and two cones of heights l_l and l_r. (d) Growth of the second bubble at the fixed position x_0. The first bubble has arrived at the larger opening and grows outward of the tube. Ejection of the first bubble (which is repeated for the second and subsequent bubbles with frequency f), when it possesses the radius r_e, initiates unidirectional micromotor motion with its smaller opening forward (after [Klingner17]).

and, hence, the surface tension energy [Fomin14]. The bubble of mass m_b (which depends on time as long as the catalytic production of the gas goes on) moves with respect to the tube of mass m_j with a relative velocity in the low Reynolds number regime [Clanet04]:

$$v_b(t) \approx 0.012 F_p(t) \frac{\pi R_j^2(x_b(t))}{\eta V_b(t)}. \tag{5.4}$$

It is determined by the capillary force, which plays the role of the driving force:

$$F_p(t) = \pi R_j^2(x_b(t)) \sigma \left(\frac{1}{R_l} - \frac{1}{R_r} \right), \tag{5.5}$$

where $R_j(x)$ is the micromotor radius in the cross section determined by the coordinate x, $x_b(t)$ and $V_b(t)$ are the instantaneous position and volume of the bubble, σ is the surface tension.

With respect to the vessel, the tube moves with a velocity $\mathbf{v}_j$, and the bubble moves with the velocity $\mathbf{v}_b + \mathbf{v}_j$, where $\mathbf{v}_b$ is the instantaneous speed of the bubble relative to the tube [Klingner17]. The equation of motion for the system tube + bubble in a viscous liquid reads:

$$m_j \frac{d\mathbf{v}_j}{dt} + \frac{d}{dt} \left[m_b \left(\mathbf{v}_b + \mathbf{v}_j \right) \right] = \mathbf{F}_{d,j} + \mathbf{F}_{d,b}, \tag{5.6}$$

where $\mathbf{F}_{d,j}$ and $\mathbf{F}_{d,b}$ are the drag forces acting on the tube and the bubble, respectively. The catalytic micromotors move in the regime of very low Reynolds numbers. In this regime, the inertial forces exerted on the microjet and on the bubble are significantly smaller than the drag forces:

$$\left| m_j \frac{d\mathbf{v}_j}{dt} \right| \ll \left| \mathbf{F}_{d,j} \right|, \left| \frac{d}{dt} \left[m_b \left(\mathbf{v}_b + \mathbf{v}_j \right) \right] \right| \ll \left| \mathbf{F}_{d,b} \right|, \tag{5.7}$$

in accordance with the neglect of all inertial forces in the low Reynolds number world.

For the capillarity mechanism [Fomin14, Klingner17], a driving force is a capillary force induced by the bubble motion through the tube. Accordingly, the driving force in eq. (5.1) as a function of time $\mathbf{F}_C(t)$ depends on the instantaneous bubble radius $R_b(t)$ and the absolute speed of the bubble with respect to the vessel $\mathbf{v}_b(t) + \mathbf{v}_j(t)$:

$$\mathbf{F}_C(t) = -6\pi\eta R_b(t) \left(\mathbf{v}_b(t) + \mathbf{v}_j(t) \right). \tag{5.8}$$

Starting from $m_b(t) = G_{O_2} t = \frac{4}{3}\rho_{O_2}\pi R_b(t)^3$, we find the maximal bubble radius $R_b(1/f) = \sqrt[3]{3G_{O_2}/\left(4f\pi\rho_{O_2}\right)}$, where f is the bubble release frequency, ρ_{O_2} is the mass density of oxygen and G_{O_2} is the mass rate of oxygen production. The instantaneous micromotor speed for this mechanism [Klingner17] is calculated according to eq. (5.1):

$$\mathbf{v}_j(t) = -\frac{3R_b(t)\mathbf{v}_b(t)}{3R_b(t) + \frac{L}{\ln\left(\frac{L}{b}\right) + c_1}}. \tag{5.9}$$

5.1.2 Bubble growth mechanism

Within the one-dimensional model of the bubble growth mechanism [Manjare13], the driving force $\mathbf{F}_G(t)$ depends on the size of the growing bubble [Zeng93]:

$$F_G(t) = \rho_w \pi R_b(t)^2 \left[\left(\frac{3}{2}\right) C_s \dot{R}_b(t)^2 + R_b(t)\,\ddot{R}_b(t)\right] \tag{5.10}$$

and is directed along the x-axis (see Fig. 5.4d). Here ρ_w is the mass density of the fluid and C_s is a sample-specific fitting constant taken from experiment [Manjare12]. As long as the growth of the bubble occurs as a cubic root of time: $R_b(t) = \gamma t^{1/3}$, where $\gamma = \sqrt[3]{3G_{O_2}/(4\pi\rho_{O_2})}$, the driving force obeys the power law with the decay exponent –2/3:

$$F_G(t) = m_j \beta t^{-2/3} \text{ with the coefficient } \beta = \gamma^4 \frac{\rho_w \pi}{9 m_j}\left(\frac{3}{2}C_s - 2\right). \tag{5.11}$$

For the micromotor characterized by a position $\boldsymbol{x}_j$, the second Newton's law of motion $m_j \ddot{x}_j = F_G + F_{d,j}$ reads

$$\dot{v}_j = \beta t^{-\frac{2}{3}} - k v_j, \;\; k = \frac{2\pi\eta L}{m_j\left[\ln\left(\frac{L}{b}\right) + c_1\right]}. \tag{5.12}$$

The instantaneous micromotor speed for the bubble growth mechanism results to be [Manjare13]:

$$v_G(t) = \beta \int_0^t \tau^{-\frac{2}{3}} e^{k\tau} d\tau e^{-kt}. \tag{5.13}$$

As mentioned in (5.11), it is proportional to the fourth power of the bubble growth parameter y. The time average micromotor speed is finally found as an integral over the period $1/f$ between two consecutive ejections:

$$\overline{v}_G = f \int_0^{1/f} v_G(t)dt. \tag{5.14}$$

5.1.3 Bubble expulsion mechanism

The driving force for the bubble expulsion mechanism [Li11] originates due to bubbles leaving the micromotor frequently, giving rise to a flow of the liquid against the directed motion of the bubbles. It is expressed by the following equation:

$$\mathbf{F}_E(t) = 6\pi\eta R_b(t)\mathbf{v}_b(t)\cos\theta, \tag{5.15}$$

where θ is the inclination angle of the direction from the center of the micromotor opening to the center of the bubble with respect to the axis of the tube, resulting from a buoyancy force during asymmetric growth of the bubble. The key assumption to calculate the displacement of the micromotor in one step is the integral of (5.1) during a specially selected time interval $[t_0,\ t_1]$ that corresponds to one step of the micromotor propulsion

$$\int_{t_0}^{t_1} \mathbf{F}_E(\tau)d\tau = -\int_{t_0}^{t_1} \mathbf{F}_{d,j}(\tau)d\tau, \tag{5.16}$$

supplemented with the *phenomenological* condition that after the expulsion, the bubble and the micromotor stop at the distance equal to the bubble diameter:

$$L_m + \int_{t_0}^{t_1} v_b(\tau)d\tau = 2R_b. \tag{5.17}$$

Here, $L_m = \int_{t_0}^{t_1} v_j(\tau)$ is the displacement of the micromotor during one propulsion step. The latter is found from (5.17) by substituting (5.2) and (5.15) into (5.16):

$$L_m = \frac{6R_b^2\cos\theta}{3R_b\cos\theta + L/\left(\ln\left(\frac{L}{b}\right) + c_1\right)}. \tag{5.18}$$

The bubble expulsion frequency is straightforwardly calculated (from the condition that the amount of generated oxygen during the period $1/f$ between two consecutive expulsions equals the volume of the bubble)

$$f = \frac{6nc_0L\left(R_{\max} - \frac{L}{2}\tan\phi\right)}{4{R_b}^3\cos\phi} \tag{5.19}$$

as a function of the concentration c_0 of H_2O_2, and the volume rate of oxygen production from a unit area n. For instance, the latter is estimated to be 9.8×10^{-4} m·s^{-1} from both flat and rolled-up surfaces in H_2O_2 with concentrations up to ~10% in the experiment of ref. [Li11]. Finally, the time average micromotor speed for this mechanism is found to be [Li14]

$$\bar{v}_E \equiv f\int_0^{1/f} v_E(t)dt = fL_m = \frac{9nc_0L\left(R_{\max} - \frac{L}{2}\tan\phi\right)\cos\theta}{3{R_b}^2\cos\phi\cos\theta + LR_b\cos\phi/\left(\ln\left(\frac{L}{b}\right) + c_1\right)}. \tag{5.20}$$

According to eqs. (5.15) and (5.20), the micromotor speed for the expulsion mechanism vanishes as soon as bubbles either do not move ($v_b = 0$) or are not expelled from the micromotor ($f = 0$). This phenomenological model is demonstrated to be useful to explain the average speed of a micromotor in certain cases [Li14].

5.1.4 Combination of propulsion mechanisms

The propulsion of micromotors fabricated by 3D laser lithography by polymerizing the photoresist and coating the structures with Cr (10 nm), Ni (130 nm), Ti (20 nm) and Pt (30 nm) by E-beam evaporation is experimentally investigated by immersing them in a water solution of H_2O_2, which undergoes catalytic decomposition into oxygen and water on the Pt surface, and surfactant SDS, which reduces the surface tension. The numerical modeling of propulsion is performed for catalytic micromotors with the length $L = 50$ μm, the radii of the lager and smaller openings $R_{\max} =$ 10 μm and $R_{\min} = 5.6$ μm, correspondingly, the semicone angle $\phi = 5°$ [Wrede20].

The speed of micromotors increases with increasing surfactant concentration from 1.25% to 10% SDS, where the bubble growth mechanism provides the largest contribution. When the concentration of SDS in the fuel liquid is further increased to 20% and to 30%, where the capillarity mechanism is most significant, a rapid decrease in the speed of micromotors occurs (see Fig. 5.3a). This behavior is associated with the fact that the bubbles diminish with increasing surfactant concentration from 1.25% to 10% SDS, and grow much larger when further increasing SDS concentration to 20% and 30%. At the same time, the average bubble expulsion frequency rises with increasing surfactant concentrations from 1.25% to 10% SDS, and dramatically decreases for concentrations of 20% and 30% SDS. The micromotors stop completely at SDS concentration of 30% by forming only one big bubble, which remains attached to the tube (this is a transition to the overloaded micromotor regime discussed in Section 5.2).

The observed increase in the micromotor speed with increasing concentration in the interval from 2.5% to 30% H_2O_2 shown in Fig. 5.3b is associated with a

decrease of bubble size and an increase of the average bubble expulsion frequency. The bubble growth mechanism is predominant at the concentration of peroxide <22%, yielding a dominant position to the bubble expulsion mechanism at the higher concentrations. However, as shown in Fig. 5.5b, at the highest concentration of 30% H_2O_2, the calculation solely for the bubble expulsion mechanism provides a good comparison with the observed data.

In Fig. 5.3c, the trend of lowering the speed due to higher viscosity is revealed in the observed micromotors by adding the methylcellulose in the liquid. It arises due to the increase of the bubble size and the decrease of the bubble expulsion frequency in fuels with higher viscosity. The graphs for the simulated speed of micromotors for the three considered propulsion mechanisms indicate that with increasing viscosity $\eta < 2$ mPa·s via 2 mPa·s $< \eta <$ 5.5 mPa·s to $\eta >$ 5.5 mPa·s, the bubble growth mechanism, the capillarity mechanism and the bubble expulsion mechanism are consecutively the most influential.

In summary, as follows from Fig. 5.5, none of the above propulsion mechanisms alone is sufficient to explain the measured micromotor speed. A solution to overcome this challenge is provided by considering a combination of the different propulsion mechanisms [Wrede20]. A switching of the propulsion mechanisms, each of which acts only over some time intervals within the combined regime model (Fig. 5.6a), allows for explanation of the experimentally observed behavior of the catalytic micromotors as a function of the fuel composition (Fig. 5.6b). The bubble expulsion regime is dominant for the H_2O_2 concentrations of about 20% and higher. At the surfactant SDS concentrations ≥20% as well as the dynamic viscosities ≥0.004 Pa·s, the bubble growth combined with the capillarity regime occurs dominant for the micromotor propulsion. All three propulsion regimes are in force in the remaining areas of the fuel parameters.

5.2 Transition between unidirectional motion and overloaded regime

The multiple bubble nucleation model (illustrated in Fig. 5.6a for the case of two bubbles) describes the micromotor movement due to the bubble expulsion, when there are a few bubbles in the tube at any time [Klingner17]. *Unidirectional* micromotor motion is attributed to bubble expulsion before micromotor blockage by additional bubbles. The multiple bubbles nucleation model provides stepwise micromotor motion (Fig. 5.7), which compares well to the experimental results [Fomin14]. Compared with that experiment, the multiple bubble nucleation model provides more accurate results for bubble expulsion frequency, than the bubble expulsion model and the bubble growth model, and agrees with experimentally detected micromotor speed within a factor of 2. The bubble position $x_b(t)$ and micromotor speed $v_j(t)$ are shown in Fig. 5.7 for three periods. In the first 50.9 ms of each period, the bubble

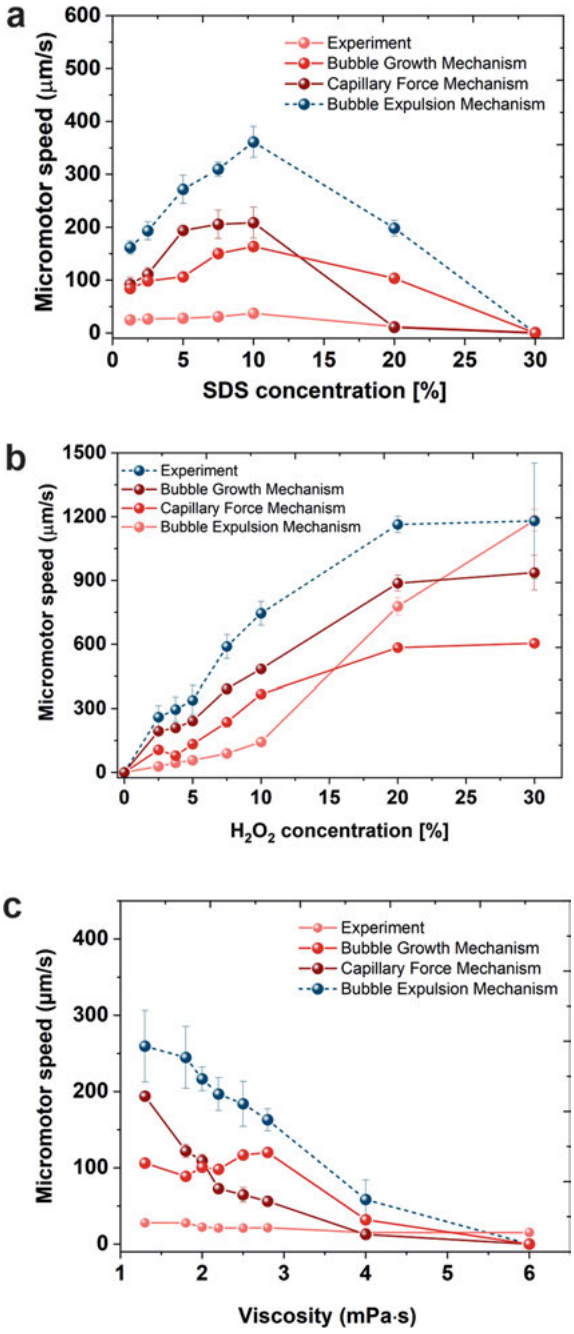

Fig. 5.5: Speed of micromotors as a function of the surfactant SDS concentration (a), peroxide concentration (b) and the dynamic viscosity of the fuel solution (c) for different propulsion mechanisms in comparison with experimental data (after [Wrede20]).

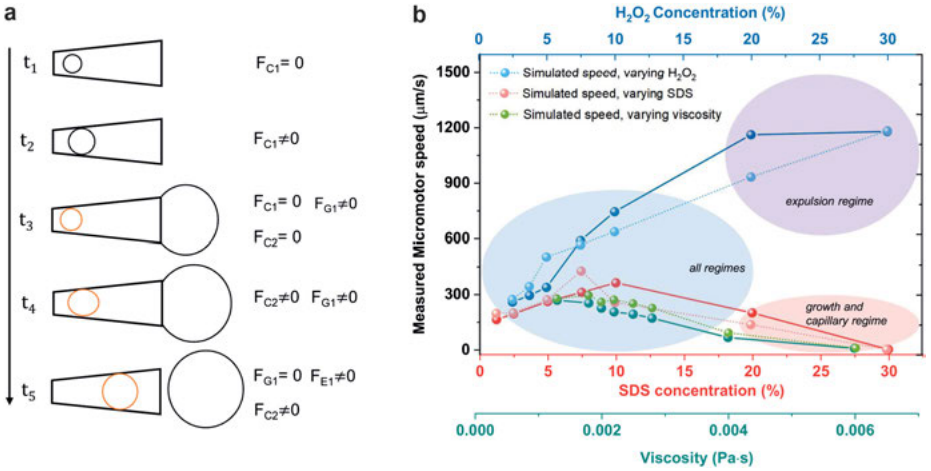

Fig. 5.6: (a) Scheme of the driving forces acting over different time intervals during the motion of a catalytic micromotor with two bubbles within the model of combined propulsion regimes. (b) Switching of the propulsion regimes of self-rolled micromotors as a function of the H_2O_2 concentration, the SDS concentration and the viscosity (a schematic) (after [Wrede20]).

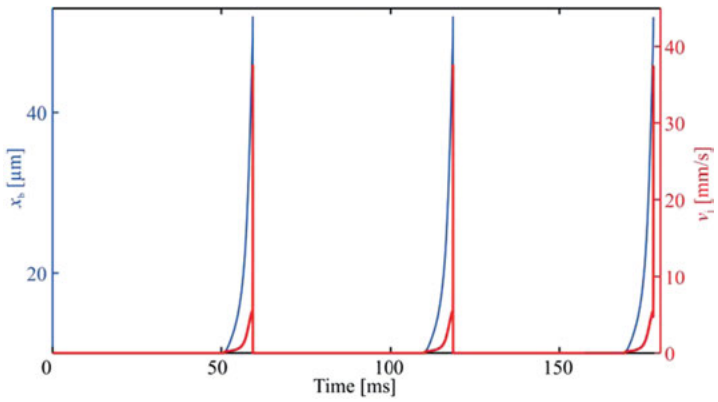

Fig. 5.7: Bubble position $x_b(t)$ and micromotor speed $v_j(t)$ as a function of time for $x_0 = 10$ μm, $\theta = 0°$, and hydrogen peroxide concentration $c_0 = 1\%$ (from [Klingner17]).

remains at its initial position and v_j is zero. Then the bubble moves toward the larger opening at speed of up to 60 μm/s and is expelled. As a result, the micromotor moves stepwise with average speed of 200 μm/s.

The multiple bubble nucleation model allows for a systematic analysis of the micromotor dynamic regimes as a function of the nucleation position (Fig. 5.8a),

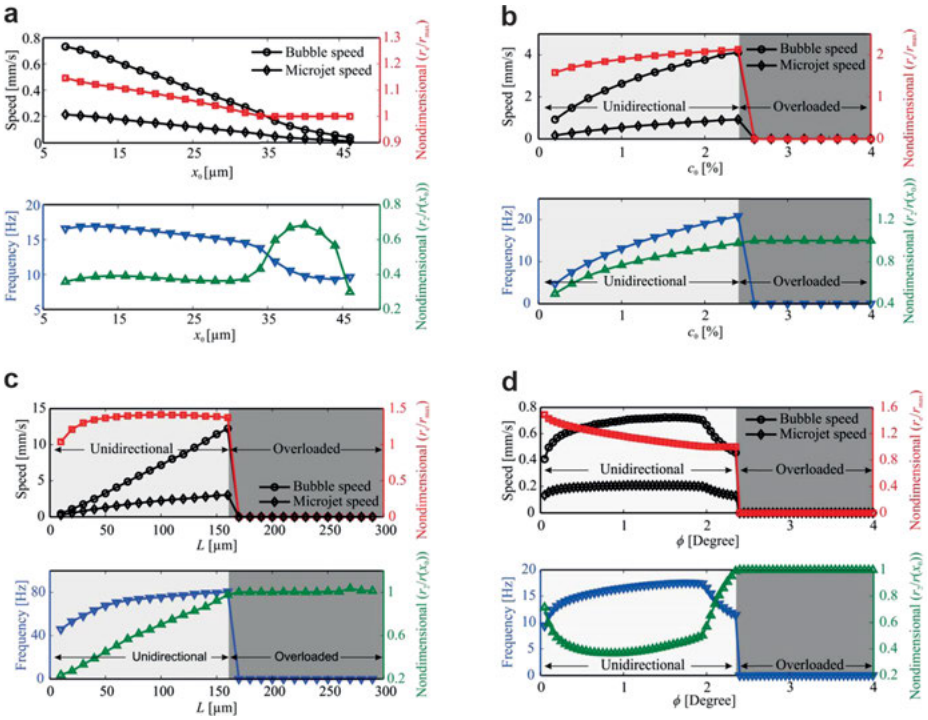

Fig. 5.8: Average bubble speed (v_b) and average micromotor speed (v_j), normalized ejected bubble size r_e/R_{max}, frequency f and normalized second bubble radius $r_2/R_i(x_0)$ as a function of (a) the nucleation position x_0 for $L = 50$ μm at $c_0 = 1\%$; (b) the hydrogen peroxide concentration for $L = 200$ μm, $x_0 = 10$ μm; (c) the length L for $x_0 = 0.1\,L$, the average tube radius $R = 3$ μm, $\phi = 1.14°$ at $c_0 = 7\%$; (d) the semicone angle ϕ for $L = 50$ μm, $x_0 = 0.1\,L$, $R = 3$ μm at $c_0 = 7\%$. In all cases, the contact angle $\theta = 0°$ (from [Klingner17]).

the hydrogen peroxide concentration (Fig. 5.8b), the micromotor length (Fig. 5.8c) and the contact angle (Fig. 5.8d) (after [Klingner17]).

Unidirectional micromotor motion is achieved for all nucleation positions in Fig. 5.8a. As the first bubble nucleates close to the smaller opening, it collects a large amount of oxygen, when it moves through the whole tube due to the capillary force. Therefore, the expelled bubble is relatively large and possesses high speed toward the larger opening. Consequently, the average speed and frequency of bubble expulsion are relatively high. The second bubble has a relatively small radius as it has a shorter time to grow and a smaller surrounding, from which it collects oxygen, as compared to the first bubble. If the first bubble nucleates close to the large opening, it reaches low speed, since the pressure difference is decreased. Therefore, the expulsion frequency is low, and the expelled bubble has the size of the large opening R_{max}. The second bubble is large, as it has a longer time to grow and a larger surrounding to collect oxygen. These results explain the statistical nature of micromotors'

behavior reported in [Mei08, Solovev09] by a random variation of the nucleation position.

All other physical and geometrical parameters of the model reveal a transition from the unidirectional to the overloaded regime. *Overloaded* micromotors are caused by multiple bubbles of the size of micromotor radius, which hinder further bubble ejection, and result in negligible displacement of the microjet. Quantitatively, overloaded microjets are found by the model for high contact angles (>9°), high hydrogen peroxide concentration (>2.5%) and relatively long microjets (>160 μm).

The micromotor has unidirectional motion up to the contact angle of 9°, the characteristics of that motion being independent of θ. The first bubble is expelled with radius slightly exceeding R_{max}, while the second bubble reaches the size of ~$0.4R_j(x_0)$. At contact angles above 9°, the size of the second bubble increases suddenly, establishing the overloaded regime, when the frequency, the bubble speed and the micromotor speed are reduced to zero. Overloaded micromotors at high contact angles $\theta > 9°$ explain the experimentally reported necessary addition of surfactants to reduce contact angles [Solovev09], because the contact angle of water on platinum surface equal to 40° lies within the overloaded regime.

As shown in Fig. 5.8b, below the critical hydrogen peroxide concentration of 2.5%, the microjet moves unidirectionally, and the bubble speed, the micromotor speed, the radius of the expelled bubble, the radius of the second bubble and the expulsion frequency increase with the concentration. The micromotor occurs overloaded above a critical concentration of 2.5%, when $r_2/R_j(x_0) = 1$.

The predicted critical length of 160 μm for a transition from the unidirectional to overloaded regime (Fig. 5.8c) is in agreement with the experimental value between 150 and 200 μm [Li11]. A transition from unidirectional to overloaded regime is observed at $\phi = 2.4°$ (Fig. 5.8d). In the unidirectional regime, the bubble speed, the micromotor speed and the expulsion frequency increase with the semicone angle and decrease for $\phi > 2°$. The angle does not have to be precisely implemented, because there is a broad maximum around the optimum semicone angle.

5.3 Theory of self-propelled micromotors for cleaning polluted water

The use of catalytically self-propelled micromotors for degrading organic pollutants in water via the Fenton oxidation process is described in [Soler13]. The tubular micromotors are composed of self-rolled functional nanomembranes consisting of Fe/Pt bilayers. Both the inner and outer layers of the micromotors actively interact with their environment, that is, the inner Pt for the self-propulsion and the outer Fe for the in situ generation of ferrous ions. Altogether, these micromotors are capable of boosting the degradation of organic pollutants and mixing the liquids where they swim. The degradation of organic pollutants takes place in the presence of hydrogen peroxide,

which acts as a reagent for the Fenton reaction and as main fuel to propel the micromotors. Factors influencing the efficiency of the Fenton oxidation process, including thickness of the Fe layer and concentration of hydrogen peroxide, are investigated. The ability of these catalytically self-propelled micromotors to improve intermixing in liquids results in the removal of organic pollutants approximately 12 times faster than when the Fenton oxidation process is carried out without catalytically active micromotors. The use of catalytic micromotors to boost Fenton oxidation processes holds considerable promise for the remediation of water contaminated with nonbiodegradable and dangerous organic pollutants.

Mixing of the peroxide solution in the reaction vessel due to the propulsion of microjets is modeled using the stationary continuity equation for fluid dynamics [eq. (2-1.1) in [Happel83]]

$$\mathrm{div}\mathbf{j}(\mathbf{r}) = 0, \tag{5.21}$$

where the mass flux density is defined as a product of the local concentration $c(r)$ and local fluid velocity $\mathbf{v}(r)$:

$$\mathbf{j}(\mathbf{r}) = c(\mathbf{r})\mathbf{v}(\mathbf{r}). \tag{5.22}$$

The process of mixing along the vertical z-axis can be modeled by assuming that the concentration is a function of the z-coordinate only, while the z-component of the velocity is an average over an ensemble of micromotors with different coordinates (x,y) in the horizontal plane over all area in the Petri dish, which is accessible to the moving micromotors:

$$v_z(z) = \int\limits_{\text{accessible area}} v_z(x,y,z)dxdy \Big/ \int\limits_{\text{accessible area}} dxdy. \tag{5.23}$$

Then the continuity equation [eq. (5.21)]

$$\frac{d}{dz}[c(z)v_z(z)] = 0 \tag{5.24}$$

after integration over the vertical coordinate from a point z to the top of the fluid in the Petri dish (L_{fluid}) gives

$$\frac{c(z)}{c(L_{\text{fluid}})} = \frac{v_z(L_{\text{fluid}})}{v_z(z)}. \tag{5.25}$$

With the diameter of the Petri dish $D = 30$ mm and the volume of the fluid $V = 1$ ml, the height of the fluid in the Petri dish is $L_{\text{fluid}} = 1.41$ mm.

Investigation of the velocity profile $\mathbf{v}(\mathbf{r})$ of a viscous fluid dragged by a moving micromotor constitutes a challenging hydrodynamic problem. Here we use a standard approximation: when analyzing motion in a viscous fluid, elongated orthotropic bodies can be represented by prolate ellipsoids of revolution ([Happel83], p. 222). The flow of a

viscous fluid dragged by an ellipsoid (in our calculation, the axes of the ellipsoid are equal to diameter $2R = 120$ μm and length $L = 500$ μm of the microjet) moving with velocity $\mathbf{v}_{jet}$ (according to the experimental data, $v_{jet} = 538\,\mu m/s$) is described by employing the Navier–Stokes equation ([Happel83], Chapter 4). The solutions represented in Fig. 5.9 are obtained using two assumptions: (i) low Reynolds number regime and (ii) no-slip boundary conditions at the surface of the body. These results provide a generalization of the well-known Stokes law of resistance onto a fluid flow past a nonspherical body [Happel83]. Because of a large diameter of the Petri dish compared to the sizes of a model micromotor, the effects of the walls on the fluid velocity field are negligible.

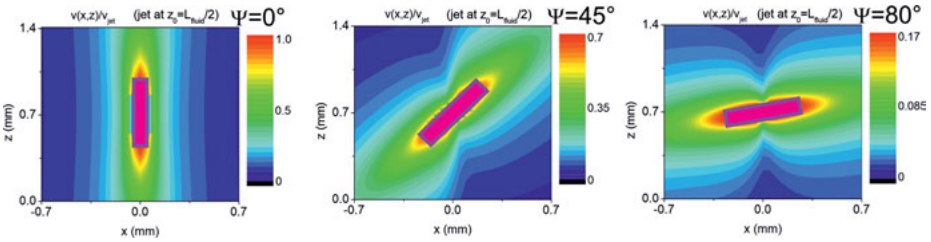

Fig. 5.9: The fluid velocity profile related to the micromotor velocity as a function of the vertical coordinate z and the horizontal coordinate for model micromotors centered at the half-height of the fluid in the vertical direction ($0.5L_{fluid}$). The values of the angle Ψ between the microjet velocity $\mathbf{v}_{jet}$ and the vertical z-axis are given in the panels. Calculation parameters are given in the text.

The average z-components of the fluid velocity are estimated for model micromotors centered at the half-height of the fluid in the vertical direction ($0.5L_{fluid}$) and moving at various values of the angle Ψ between the microjet velocity $\mathbf{v}_{jet}$ and the vertical z-axis. In Fig. 5.10a, they are plotted as a function of the coordinate z together with the average over an ensemble of micromotors with different values of the angle Ψ from 0 to 90°. The corresponding profiles of the hydrogen peroxide concentration calculated according to eq. (5.11) are represented in Fig. 5.10b.

The average z-component of the fluid velocity reaches its maximum values at the front and rear points of the moving micromotor, where the absolute value of the total fluid velocity is v_{jet} due to the nonslip boundary condition. These points are separated by a distance equal to the size of the projection of the micromotor onto the vertical axis. This is clearly shown in Fig. 5.10a: the distance between the local maxima of the average z-component of the fluid velocity is the largest for $\Psi = 0$ and monotonously decreases with increasing Ψ. Averaging over an ensemble of micromotors with different values of angle Ψ results in a significantly broadened profile of the z-component of the fluid velocity with its largest values at intermediate angles $\Psi \sim 45°$, because in this case contributions to the z-component of the fluid velocity are gathered optimally from the total surface of the micromotor, which propels inclined with respect to the vertical axis. However, averaging over an ensemble of micromotors with different values of

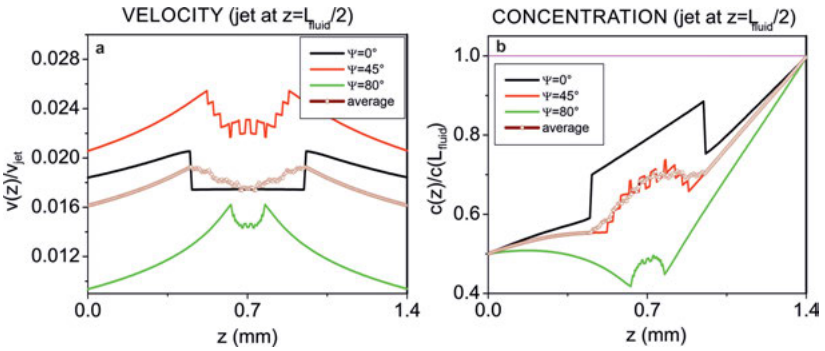

Fig. 5.10: The average z-component of the fluid velocity related to the microjet velocity (a) and the peroxide concentration related to its undisturbed value far away from the moving micromotor (b) calculated as a function of the vertical coordinate z for model micromotors centered at the half-height of the fluid in the vertical direction ($0.5L_{\text{fluid}}$). The values of the angle Ψ between the microjet velocity $\mathbf{v}_{\text{jet}}$ and the vertical z-axis are given in inset. The results averaged over an ensemble of micromotors with different values of the angle Ψ are represented with open circles. The pink thin line in panel (b) represents the undisturbed value of the hydrogen peroxide concentration far away from the moving micromotor (from [Soler13]).

angle Ψ provides the z-component of the fluid velocity of the same order of magnitude as that for vertically moving micromotors ($\Psi = 0$).

Within the present model, mixing of the hydrogen peroxide occurs due to the following physical reason: In order to keep the mass flux density along the vertical axis constant, the hydrogen peroxide concentration must be an inverse function of the average z-component of the velocity [see eq. (5.25)]. As shown in Fig. 5.10b, the hydrogen peroxide concentration profile has minima just in the regions at the front and rear points of the moving micromotor, where the average z-component of the fluid velocity reaches its maximal values. Accordingly, there occurs a redistribution of the hydrogen peroxide concentration in the vicinity of the micromotor, which decays far away from it. The highest modulation of the peroxide concentration ~20% is due to the vertical propulsion of microjets ($\Psi = 0$). Averaging over an ensemble of micromotors with different values of the angle Ψ smears the profile of the hydrogen peroxide concentration and provides the modulation of the order of 10%.

In conclusion, the region of rearrangement of the hydrogen peroxide concentration moves in space *together with propelling micromotors*. Therefore, the drag of the solution due to the propulsion of micromotors is an effective mechanism of mixing hydrogen peroxide in the reaction vessel. The combination of mixing and releasing iron ions in liquids results in a rate of removal of rhodamine about 12 times higher than when the Fenton oxidation process is carried out with nonpropelling Fe self-rolled tubes [Soler13]. The usefulness of the self-rolled micromotors lies thus in their combined capacity not only to propel, but to exploit their motion using their external surface to enhance useful catalytic reactions.

6 Topologic signatures of electromagnetic fields in rolled-up microcavities

Modern advances in nanofabrication have provided novel high-tech materials for nanophotonics with tailored optical properties. Thanks to the self-rolling nanotechnology, a variety of nanomembrane-based tubular sensors working on different principles have been developed [Wang19]. First, tubular electrodes have been developed as electric biosensors for detecting hybridization of complementary DNA strands [Medina16] by impedimetric measurements. Second, self-rolled microtubes have been integrated with silicon-based waveguides [Madani15] and developed as vertical whispering-gallery-mode (WGM) optical microcavities for optofluidic sensing [Madani17]. Strong evanescent fields occurring due to the microcavity walls of thickness ~100–200 nm have ensured efficient interactions between the WGMs and the objects inside the inner opening of the microtube acting as sensing channel [Wang18]. Third, because of a highly flexible integration with on-chip optical, magnetic, electrical devices as well as microfluidic circuits [Harazim12], self-rolled microtubes have been proposed as a key structural element for lab-on-a-chip biosensing systems. Fourth, silica-based microtubes as optical [Miao15, Yin19a] or optoplasmonic [Yin19b] cavities have been designed for probing the binding dynamics of molecules. In particular, graphene-integrated optoplasmonic microtubes have been applied for sensitive surface detection with resolution down to the single molecular layer [Yin19b]. Finally, a merger of all these individual biosensing nano-/microarchitectures by integration onto a silicon chip is a highly promising way to create chip-scale, low-cost, highly sensitive, multifunctional optoelectrofluidic bioanalytical systems [Wang20] for advancing medical diagnostic and personal healthcare.

A Möbius-ring resonator [Li13] and a self-rolled asymmetric microcavity [Ma16a] discussed in the present Chapter are representative nanostructured microarchitectures, which give rise to fascinating topological effects by virtue of Möbiosity, optical spin–orbit coupling and non-Abelianism.

6.1 Resonant modes of light in a Möbius-ring resonator

In-plane polarized light reveals a nontrivial topological evolution in the course of a resonant propagation in a Möbius-ring resonator made of a twisted dielectric strip with the refraction index n [Li13]. The strip thickness L_z is assumed to be much smaller than the light wavelength: $L_z < \lambda/n$, so that the electric field is assumed to be stringently confined within the strip in the course of propagation. The strip width is taken larger than the wavelength, and the strip length is selected in the micrometer range to support optical modes in the visible spectral range. Figure 6.1 shows amplitude profiles for resonant

https://doi.org/10.1515/9783110575576-006

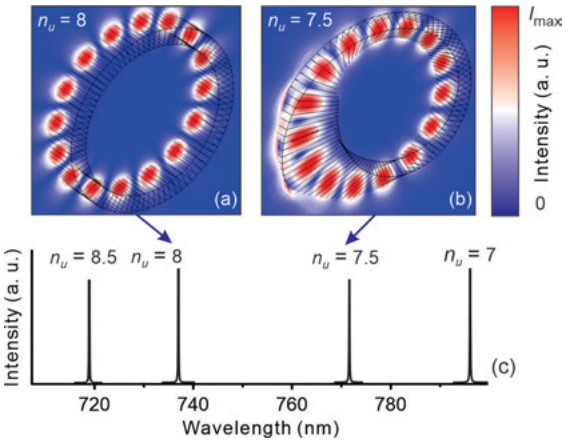

Fig. 6.1: Amplitude profiles for resonant modes with integer and noninteger number of wavelengths along the centerline for a cylindrical-ring resonator (a) at $n_u = 8$ and a Möbius-ring resonator (b) at $n_u = 7.5$. Both structures are formed of equivalent strips with $L_x = 2{,}510$ nm, $L_y = 320$ nm, $L_z = 80$ nm with a refractive index $n = 3.5$ and immersed in air. Numbers of antinodes along the centerline are $N = 16$ and $N = 15$, correspondingly. (c) Calculated resonant spectra of intensity for two resonant modes in the cylindrical-ring resonator ($n_u = 7,\ 8$) and two resonant modes in the Möbius-ring resonator ($n_u = 7.5,\ 8.5$) (after [Li13]).

modes of light in a cylindrical-ring resonator and a Möbius-ring resonator with the numbers of wavelengths along the centerline $n_u = 8$ and $n_u = 7.5$, respectively.

The integer linearly polarized resonance modes in a cylindrical ring are invariant under rotations by 2π around the z-axis, which is analogous to the rotational symmetry of a boson field:

$$\mathbf{E}(u + 2\pi) = \mathbf{E}(u). \tag{6.1}$$

In a cylindrical ring, a rotation of the electric field around the z-axis by 2π returns it to the original position (Fig. 6.2a). The half-integer linearly polarized resonance modes in a Möbius ring are invariant under rotations by a minimum of 4π rather than 2π around the z-axis, in analogy to the rotational symmetry of fermions [Ballon08]:

$$\mathbf{E}(u + 2\pi) = -\mathbf{E}(u),\ \ \mathbf{E}(u + 4\pi) = \mathbf{E}(u). \tag{6.2}$$

Due to the twist, a rotation of the electric field around the z-axis by 2π results in a vector reversal (Fig. 6.2b). Thus, Möbiosity introduces a key property of *fermions* to the *bosonic* electromagnetic field.

The structure of the amplitude profiles for resonance light modes reveals a remarkable similarity to the structure of the electronic wave function in a Möbius ring with a half-integer number of wavelengths along the centerline of the Möbius band n_u shown in Fig. 6.4 of [Fomin18b]. However, when a linearly polarized light enters

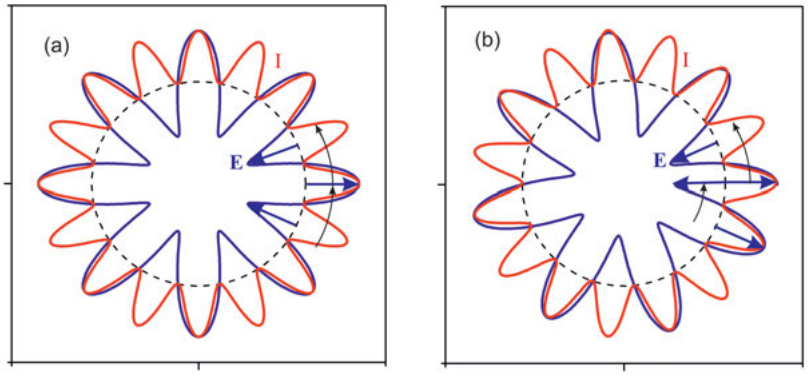

Fig. 6.2: Distributions of the electric field **E** (blue line) and intensity *I* (red line) for linearly polarized resonance modes around the centerline (dashed line) in the tangential plane for (a) a cylindrical-ring resonator ($n_u = 8$) and (b) a Möbius-ring resonator ($n_u = 7.5$) (after [Fomin18b]).

the Möbius-ring resonator with an appreciable contrast of refractive indices, the optical electric field is forced to remain parallel to the plane of the twisted strip, and consequently, the polarization orientation continuously varies along the twisted strip during propagation. This behavior represents an adiabatic parallel transport of linearly polarized light in a smoothly curved Möbius ring [Berry87] and allows for an interpretation [DeWitt79] in terms of a geometric phase introduced by the twist.

Similar numerical simulations reveal occurrence of half-integer plasmonic modes in metallic Möbius rings at the nanoscale [Yin17].

6.2 Evolution of light in self-rolled asymmetric microcavities

The cone-like microcavities are fabricated by self-rolling pre-strained circularly patterned SiO_x/SiO_2 bilayer nanomembranes on a silicon substrate [Bolanos12]. After roll-up, a 30-nm-thick hafnium oxide film is grown on the microtube surface by atomic-layer deposition. The wall thickness is about 100 nm. The tube length is 45 mm. The microtube has a mean diameter of 7 μm and a difference of ~1.5 μm between the diameters at the larger and smaller ends. Correspondingly, the conical angle of the asymmetric tube is estimated to be ~2°. The average refractive index of the asymmetric tube wall is anisotropic: it changes along the tube axis due to the variation of the number of windings [Ma16a].

In the asymmetric microtube cavity, optical WGM resonances are established via optical self-interferences along a closed trajectory guided by the cylindrical tube wall. To pump the WGM resonances, a linearly polarized laser light at 532 nm is focused on the larger end, where high-quality-factor resonant modes exist. The laser-excited luminescent defects in the amorphous silicon oxide emit light in the visible

spectral range at room temperature. Due to the subwavelength-thin tube wall of 100 nm, photons are supposed to be linearly polarized along the tube wall because of a high enough dielectric contrast between the silicon oxide and the air. The photons move along a closed trajectory within the microtube. Those photons, which eventually escape from the microcavity, are measured and analyzed [Ma16a]. The initial state of the resonant light is linearly polarized with the polarization oriented around the tube axis.

In such conical-shaped self-rolled asymmetric microcavities, the optical spin–orbit coupling is enabled and, as a consequence, a noncyclic optical geometric phase acquired in the course of a non-Abelian evolution is observed [Ma16a]. Namely, in a self-rolled asymmetric microcavity being pumped by a laser beam (532 nm), the incoming linearly polarized light is found to evolve as the elliptically polarized one, the major axis being tilted out of the tube axis by an angle φ (Fig. 6.3a).

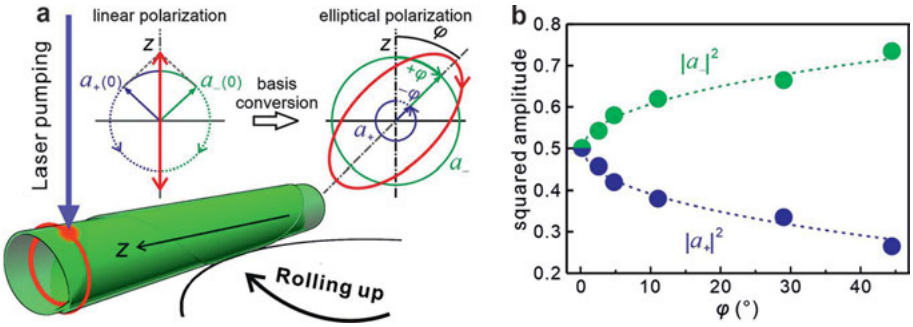

Fig. 6.3: (a) Self-rolled conical microtube cavity and the elliptical polarization state of light occurring due to the conversion of basis. (b) Conversion between the clockwise (green) and anticlockwise (violet) basis states. Lines represent the squared amplitudes of the circularly polarized waves as a function of the geometric phase calculated according to eq. (5.11). The experimental data are shown with circles of the respective colors (from [Ma16a]. This work is licensed under a Creative Commons Attribution 4.0 International License, http://creativecommons.org/licenses/by/4.0/).

Propagation of light in an inhomogeneous anisotropic dissipationless medium with dielectric permittivity tensor $\hat{\varepsilon}(\mathbf{r})$ is described by the wave equation [Bliokh07, Bliokh08]

$$\left[L^2\Delta - L^2\nabla\nabla + \hat{\varepsilon}(\mathbf{r})\right]\mathbf{E} = 0, \tag{6.3}$$

where $L = \frac{c}{\omega}$ is the vacuum wavelength divided by 2π. In a weakly anisotropic medium

$$\hat{\varepsilon}(\mathbf{r}) = \varepsilon_0(\mathbf{r})\hat{\mathrm{I}} + \hat{\Delta}(\mathbf{p}, \mathbf{r}),$$

where hats denote matrices; $\hat{\mathrm{I}}$ is a unit matrix. The wave equation (6.3) is solved in the first approximation in the parameters of the weak anisotropy ($\mu_A = ||\hat{\Delta}||/\varepsilon_0 \ll 1$) and geometric optic ($\mu_{\mathrm{GO}} = \lambda/L \ll 1$) [Bliokh08]. The evolution of the polarization along a ray from the initial polarization $\mathbf{a}(0)$ is approximately described by the path integral over the phase coordinates $(\tilde{\mathbf{p}}, \tilde{\mathbf{r}})$ of the zero-approximation light ray of length L [like in $\mathbf{a}(\mathrm{L})$ in eq. (6.4)]:

$$\mathbf{a}(L) = \int \exp\left[i\hat{\Phi}\right] D\tilde{\mathbf{p}} D\tilde{\mathbf{r}}\, \mathbf{a}(0) \tag{6.4}$$

with the phase

$$\hat{\Phi} = \frac{1}{L}\int_0^L \tilde{\mathbf{p}} \cdot \mathrm{d}\tilde{\mathbf{r}}\hat{\mathrm{I}} + \int_0^L \tilde{\mathbf{a}}(\tilde{\mathbf{p}}) \cdot \dot{\tilde{\mathbf{p}}}\hat{\sigma}_z \mathrm{d}\ell + \frac{1}{2L}\int_0^L \hat{\delta}(\tilde{\mathbf{p}}, \tilde{\mathbf{r}})\mathrm{d}\ell. \tag{6.5}$$

The first term in eq. (6.5) describes classical dynamics of the center of a wave packet in the circular basis; it is the same for both polarizations and does not change the polarization characteristics. In what follows, it will be disregarded without loss of generality. The second term in eq. (6.5) is analogous to the electron spin–orbit interaction, which gives rise to the geometric phase. The third term stands for the effect of the weak anisotropy of the medium; $\hat{\delta}(\tilde{\mathbf{p}}, \tilde{\mathbf{r}})$ is a transform of the tensor $\hat{\Delta}(\mathbf{p}, \mathbf{r})$. Unlike the spin–orbit interaction, the third term in eq. (6.5) contains all three Pauli matrices. The component proportional to $\hat{\sigma}_z$ renormalizes the spin–orbit interaction. The components proportional to $\hat{\sigma}_x$ and $\hat{\sigma}_y$ are anticommutative with each other and with the spin–orbit interaction [LeBellac06]. This implies the *non-Abelian* evolution of light represented by eq. (6.4).

An approximate description of the evolution of polarization in a non-Abelian system is introduced by eqs. (6.4) and (6.5). A parametrization of that evolution is performed in terms of two parameters along the ray, $\varphi = \varphi(L)$ and $C_A = C_A(L)$, describing the geometric phase and the magnitude of the anisotropy effect:

$$\mathbf{a} = \mathbf{a}(L) = \hat{\mathrm{M}}\mathbf{a}(0). \tag{6.6}$$

The mapping matrix

$$\hat{\mathrm{M}} = \exp[i(\varphi\hat{\sigma}_z + C_A\hat{\sigma}_x)] \tag{6.7}$$

is analytically calculated by expanding the exponential in a power series of its argument:

$$\hat{\mathrm{M}} = \hat{\mathrm{I}} + i(\varphi\hat{\sigma}_z + C_A\hat{\sigma}_x) - \frac{1}{2!}(\varphi\hat{\sigma}_z + C_A\hat{\sigma}_x)^2 - \frac{i}{2!}(\varphi\hat{\sigma}_z + C_A\hat{\sigma}_x)^3 + \cdots$$

Considering the basic properties of the Pauli matrices [Le Bellac06]:

$$\hat{\sigma}_x{}^2 = \hat{\sigma}_z{}^2 = \hat{\mathrm{I}},\ \ \hat{\sigma}_z\hat{\sigma}_x + \hat{\sigma}_x\hat{\sigma}_z = 0,$$

we arrive at

$$\hat{\mathrm{M}} = \hat{\mathrm{I}} + i(\varphi\hat{\sigma}_z + C_A\hat{\sigma}_x) - \frac{1}{2!}(\varphi^2 + C_A^2)\hat{\mathrm{I}} - \frac{i}{3!}(\varphi\hat{\sigma}_z + C_A\hat{\sigma}_x)(\varphi^2 + C_A^2) + \cdots$$

Arranging coefficients for each of the independent matrices, we find an analytic representation

$$\hat{\mathrm{M}} = \hat{\mathrm{I}}\cos\left(\sqrt{\varphi^2 + C_A^2}\right) + i(\varphi\hat{\sigma}_z + C_A\hat{\sigma}_x)\frac{\sin\left(\sqrt{\varphi^2 + C_A^2}\right)}{\sqrt{\varphi^2 + C_A^2}}, \tag{6.8}$$

or in the explicit form $\left(\chi = \sqrt{\varphi^2 + C_A^2}\right)$

$$\hat{\mathrm{M}} = \begin{vmatrix} \cos\chi + i\varphi\dfrac{\sin\chi}{\chi} & iC_A\dfrac{\sin\chi}{\chi} \\ iC_A\dfrac{\sin\chi}{\chi} & \cos\chi - i\varphi\dfrac{\sin\chi}{\chi} \end{vmatrix}. \tag{6.9}$$

It is noteworthy that the parameters responsible for the geometric phase φ and the magnitude of the anisotropy effect C_A are entangled in each matrix element due to the non-Abelian nature of the system.

According to eq. (6.9), the action of the mapping matrix on a linearly polarized initial basis $\mathbf{a}(0) = \frac{1}{\sqrt{2}}\begin{pmatrix}1\\1\end{pmatrix}$ results in

$$\begin{pmatrix} a_+ \\ a_- \end{pmatrix} = \hat{M}\frac{1}{\sqrt{2}}\begin{pmatrix}1\\1\end{pmatrix} = \frac{1}{\sqrt{2}}\begin{pmatrix} \cos\chi + i(C_A + \varphi)\dfrac{\sin\chi}{\chi} \\ \cos\chi + i(C_A - \varphi)\dfrac{\sin\chi}{\chi} \end{pmatrix}. \tag{6.10}$$

Due to the anisotropy effect, the squared amplitudes of the circularly polarized components

$$|a_+|^2 = \frac{1}{2}\left(1 + 2C_A\varphi\frac{\sin^2\chi}{\chi^2}\right),\ \ |a_-|^2 = \frac{1}{2}\left(1 - 2C_A\varphi\frac{\sin^2\chi}{\chi^2}\right) \tag{6.11}$$

become different, which implies an elliptical polarization of the electromagnetic wave. This is a manifestation of the *conversion of basis* occurring due to the non-Abelian dynamics of the system. According to eq. (6.11), the norm of the polarization vector is conserved: $|a_+|^2 + |a_-|^2 = 1$. The plots of the squared amplitudes of eq. (6.11) in Fig. 6.3b represent conversion of the circular basis.

A correspondence principle to the emergence of geometric phase in isotropic systems is demonstrated in the limit $C_A \to 0$, when the basis

$$\begin{pmatrix} a_+ \\ a_- \end{pmatrix} = \frac{1}{\sqrt{2}} \begin{pmatrix} \exp(i\varphi) \\ \exp(-i\varphi) \end{pmatrix} \tag{6.12}$$

describes the geometric phase φ for the clockwise and $-\varphi$ for the anticlockwise circular polarizations.

Introducing the inverse function to $\varphi = \varphi(L) \Rightarrow L = L(\varphi)$, the dependence of the anisotropy parameter on the ray length gives rise to the link between the parameters, which determines the mapping matrix: $C_A = C_A(L(\varphi)) \to C_A(\varphi)$. The resonant light experiences the non-Abelian evolution in the self-rolled asymmetric microcavity. The polarization state, as described by the eccentricity and the tilt angle, continuously changes during the resonant light propagation in the microcavity, as shown in Fig. 6.3a. It is experimentally detected when the light escapes from the microcavity. At that point, the final state of the evolution of light is reached. The ray length from the light pumping until the light escape is determined by the quality factor of the asymmetric microtube cavity. In the course of this process, the major axes of the evolving polarization state trace a helical spiral around the axis of the microtube. Matching eq. (6.11) to the experimentally detected squared amplitudes of the circularly polarized components for φ ranging from 0° to 44.5°, as shown in Fig. 6.4b, allows for the following numerical fitting [Fomin18b]:

$$C_A = 0.318 \times \varphi^{-0.433}. \tag{6.13}$$

Using the mapping matrix (6.10) and the numerical fitting (6.13), a plot of the non-Abelian evolution on the Poincaré sphere is obtained that is represented in Fig. 6.4. For the interval 0° to 44.5°, the calculated curve nicely matches the experimental data shown with circles [Ma16a]. In Fig. 6.4, the plot is continued until $\varphi = 720°$, beyond the experimentally achieved range. The curve encircles the z-axis, and at every next round, it steadily approaches the equator of the Poincaré sphere, which corresponds to the linear polarization of light.

In summary, in self-rolled asymmetric microtube resonators, the noncyclic geometric phase as well as the conversion of the photon basis occur during the non-Abelian evolution. The cone-like self-rolled asymmetric microcavities provide a platform to realize the spin–orbit interaction of light for the examination of nontrivial topological effects in the context of the non-Abelian evolution. Robustness of the topologically driven geometric phase implies promising applications by efficient manipulating photons in on-chip quantum devices.

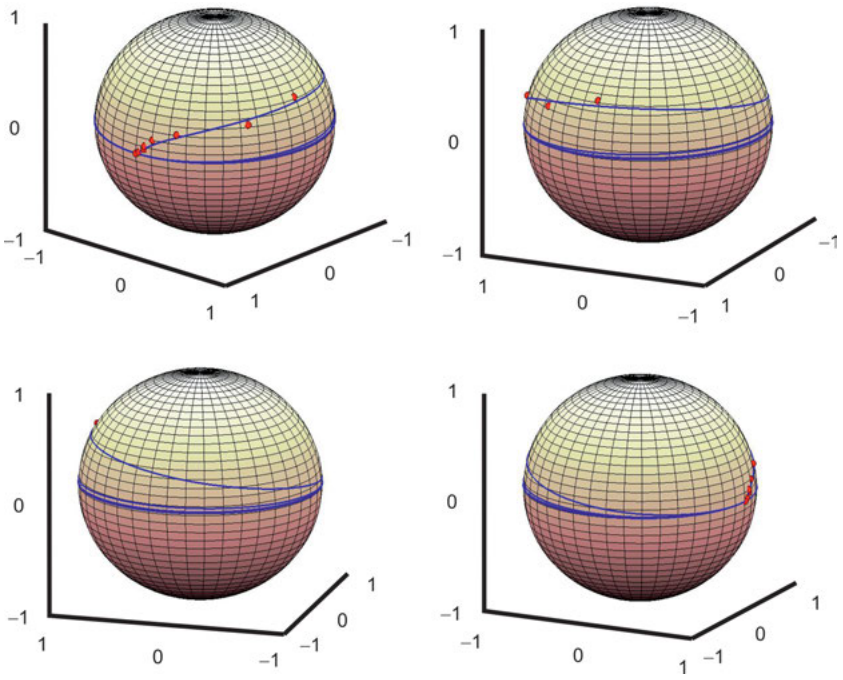

Fig. 6.4: Illustration of the non-Abelian evolution calculated using eqs. (6.10) and (6.13) as a curve on the Poincaré sphere. In order to facilitate perception, the Poincaré sphere is represented from different points of view. The experimental data of ref. [Ma16a] are shown with red circles (after [Fomin18b]).

7 Conclusions and outlook

Self-rolling high technology has been demonstrated to be one of the main avenues of fabricating diverse micro- and nanoarchitectures of complicated geometries and nontrivial topologies, which support a novel powerful trend in their functionalization in the field of nanotechnology. Therefore, analytical and numerical modeling of geometry- and topology-driven properties of self-rolled nanoarchitectures will be of paramount importance for future progress of nanophysics and nanotechnology. The key objective of this progress is to establish a large impulse for the novel topic in condensed matter: *tailoring topological order by virtue of complex geometric confinement*, which manifests unprecedentedly robust quantum properties of self-rolled nanoarchitectures and nanostructured metamaterials, and to develop their functionalization motivated by the industrial demand to replace the existing optoelectronic, biomedical and information technologies and circumvent their present limitations.

The basis for diverse prospective applications of superconducting nanodevices, in particular, as new types of detectors, sensors, qubits for quantum computing and bolometers, is in complex geometries and nontrivial topologies. Prominent signatures of vortex and phase-slip patterns due to the complex 3D geometries of the self-rolled *superconductor nanoarchitectures* have been theoretically described and experimentally found. This behavior is attributed to the specific order parameter and magnetic field distributions, which reveal nontrivial topologic properties and favor the formation of superconducting vortices and phase slips in certain regions. A nontrivial superconducting current topology induces the phase-slip dynamics, which determine the magnetic-field–voltage and current–voltage characteristics in nanoarchitectures with multiple loops of superconducting screening currents. The revealed topological transition between the vortex-chain dynamics and the phase-slip regime shows pathways of engineering the nonequilibrium properties of self-rolled superconductor nanoarchitectures for application in fluxon-based information technologies, as highly sensitive detectors and bolometers. The accumulated theoretical knowledge demonstrates that the roll-up technology provides an innovative, efficient and robust tool for fabrication of design-on-demand, better performing, energy-saving and more compact 3D nanoarchitectures.

Self-rolled *heterostructures of hybrid materials*, in particular, systems of inorganic/organic, semiconductor/metal or crystalline/amorphous heterostructures, possess promising potential in tailoring the thermoelectric properties on demand because of varying contributions of individual components to the electron and phonon transport. Therefore, the topological methods will be increasingly important for theoretical optimization of vibrational spectra and thermal transport properties in hybrid-material self-rolled systems. For this purpose, the Archimedean helical structures with standing waves along the self-rolled multilayers will be treated by generalizing the knowledge achieved for concentric cylindrical multishell models with running

https://doi.org/10.1515/9783110575576-007

waves in the azimuthal direction. The phonon dispersion and transport properties in self-rolled multishell tubular nanostructures with sizes of the order or 100 nm is a challenge for further analytical or numerical treatment, because they are in the transitional region between the realms of applicability of elastodynamics (for sizes larger than 1 μm) and the atomistic approaches (for sizes below 10 nm). The changes in the acoustic phonon spectrum and their effect on phonon transport have been experimentally detected in first thermal conductivity measurements in multishell tubular micro- and nanostructures. Realistic rolled-up spiral structures with contacting boundaries will be simulated as equivalent flat structures preserving the boundary conditions in geometrically nonlocal sense. Further studies are required to show that a reduction in the phonon group velocity and phonon thermal conductivity can be achieved without significant roughness scattering and degradation of electron transport in cross-section-modulated micro- and nanowires and arrays of self-rolled radial superlattices as promising candidates for advancement in *thermoelectric materials and devices*.

Self-rolled *magnetized microarchitectures* constitute a new playground to test unconventional topologically driven quantum-transport phenomena, like topological Hall effect, at the microscale. The magnetized microhelix coils open the unique possibility to investigate the rich variety of complex magnetic transitions, characteristic of helimagnetic bulk materials or magnetic toroidal moment in multiferroic materials, at the micrometer scale. Combination of magnetically driven propulsion and directional control of assemblies of self-rolled soft microrobots with multistimuli control over their shape using light-, pH-induced or thermal mechanism as a frontline approach to deliver and release cargos, represents a future endeavor toward biomedical applications. Since such self-rolled microrobots are being designed and created, appropriate simulation tools are of immense importance to investigate not only physical parameters, but also chemical and molecular changes, in order to predict their behavior under certain stimuli and to optimize their geometry and topology toward further functionalization.

The theoretical analysis and numerical simulation of the self-rolled bubble-propelled conical micromotors based on the interplay of the three propulsion mechanisms have provided fundamental understanding of the impact of various geometrical parameters (length, semicone angle, surface properties) and thus allowed for a quantitative interpretation of the available experimental data. This conceptual platform will be exploited to predict and optimize the performance of *catalytic micromotors* in different working environments, in particular, in biological media, toward designing and powering self-rolled robotic systems with a reproducible and reversible actuation at microscale down to nanoscale, opening up a whole cornucopia of applications in nanomedicine and nanomanufacturing. The revealed synergy between the internal and external functionalities of the self-rolled catalytic micromotors results in an enhanced degradation of dangerous organic pollutants at small-scale environments and holds a revolutionary impact on the remediation of contaminated water.

Development of the next generation of multifunctional optoelectrofluidic bioanalytical systems by integrating the individual biosensing nano-/microarchitectures onto a silicon chip poses a challenge of theoretical justification and numerical validation of strategies for elevating the sensitivities and optimizing the integration and packaging schemes for the involved microfluidic components and self-rolled *optoelectronic devices*: on-chip waveguide-based interferometers, microring resonators and photonic crystal-based cavities.

Realization of the existing ambitious goals for experiment supported by theory and modeling in the fascinating realm of self-rolled 3D micro- and nanoarchitectures will provide metamaterials and devices with tailored on-demand unprecedented characteristics, structural freedom in complex geometries and nontrivial topologies superior over conventional microelectronics, easier parallel fabrication procedures down to nanoscale, and thus advance the strategic application potential for nanoscience and nanotechnology.

Bibliography

A

[Abeles63] B. Abeles, Lattice Thermal Conductivity of Disordered Semiconductor Alloys at High Temperatures, Phys. Rev. 131, 1906–1911 (1963).

[Abramowitz72] M. Abramowitz, I. A. Stegun, *Handbook of Mathematical Functions with Formulas, Graphs and Mathematical Tables*, 10th ed., National Bureau of Standards, Washington, DC, 1972, 1046.

[Allen89] P. B. Allen, J. L. Feldman, Thermal Conductivity of Glasses: Theory and Application to Amorphous Si, Phys. Rev. Lett. 62, 645–648 (1989).

[Amelincx94] S. Amelinckx, X. B. Zhang, D. Bernaerts, X. F. Zhang, V. Ivanov, J. B. Nagy, A. Formation Mechanism for Catalytically Grown Helix-Shaped Graphite Nanotubes, Science 265, 635–639 (1994).

[Armenakas66] A. E. Armenàkas, Propagation of Harmonic Waves in Composite Circular Cylindrical Shells. I: Theoretical investigation, Am. Inst. Aeronaut. Astronautics (AIAA) J. 5, 740–744 (1966).

[Armenakas71] A. E. Armenàkas, Propagation of Harmonic Waves in Composite Circular Cylindrical Shells. Part II: Numerical Analysis, Am. Inst. Aeronaut. Astronautics (AIAA) J. 9, 599–605 (1971).

B

[Baert95] M. Baert, V. V. Metlushko, R. Jonckheere, V. V. Moshchalkov, Y. Bruynseraede, Composite Flux-Line Lattices Stabilized in Superconducting Films by a Regular Array of Artificial Defects, Phys. Rev. Lett. 74, 3269–3272 (1995).

[Balandin12] A. A. Balandin, D. L. Nika, Phononics in Low-Dimensional Materials, Mater. Today 15, 266–275 (2012).

[Balasubramanian11] S. Balasubramanian, D. Kagan, C. M. J. Hu, S. Campuzano, M. J. Lobo-Castanon, N. Lim, D. Y. Kang, M. Zimmerman, L. F. Zhang, J. Wang, Micromachine-Enabled Capture and Isolation of Cancer Cells in Complex Media, Angew. Chem. Int. Ed. 50, 4161–4164 (2011).

[Baldi08] G. Baldi, V. M. Giordano, G. Monaco, F. Sette, E. Fabiani, A. Fontana, G. Ruocco, Thermal Conductivity and Terahertz Vibrational Dynamics of Vitreous Silica, Phys. Rev. B 77, 214309, 1–14 (2008).

[Ballon08] D. J. Ballon, H. U. Voss, Classical Möbius-Ring Resonators Exhibit Fermion-Boson Rotational Symmetry, Phys. Rev. Lett. 101, 247701 1–4 (2008).

[Bandari2020] V. K. Bandari, Y. Nan, D. Karnaushenko, Y. Hong, B. Sun, F. Striggow, D. D. Karnaushenko, C. Becker, M. Faghih, M. Medina-Sánchez, F. Zhu, O. G. Schmidt, A Flexible Microsystem Capable of Controlled Motion and Actuation by Wireless Power Transfer, Nat. Electron. 3, 172–180 (2020).

[Balvin09] M. Balvin, E. Sohn, T. Iracki, G. Drazer, J. Frechette, Directional Locking and the Role of Irreversible Interactions in Deterministic Hydrodynamics Separations in Microfluidic Devices, Phys. Rev. Lett. 103, 078301, 1–4 (2009).

[Bean64] C. P. Bean, J. D. Livingston, Surface Barrier in Type-II Superconductors, Phys. Rev. Lett. 12, 14–16 (1964).

https://doi.org/10.1515/9783110575576-008

[Beechem07] T. Beechem, S. Graham, P. Hopkins, P. Norris, Role of Interface Disorder on Thermal Boundary Conductance Using a Virtual Crystal Approach, Appl. Phys. Lett. 90, 054104, 1–3 (2007).

[Beenakker16] C. Beenakker, L. Kouwenhoven, A Road to Reality with Topological Superconductors, Nat. Phys. 12, 618–621 (2016).

[Bell06] D. J. Bell, Y. Sun, L. Zhang, L. X. Dong, B. J. Nelson, D. Grützmacher, Three-dimensional nanosprings for electromechanical sensors, Sens. Actuators A 130–131, 54–61 (2006).

[Bendova16] M. Bendova, C. C. Bof Bufon, V. M. Fomin, S. Gorantla, M. H. Rümmeli, O. G. Schmidt, Electrical Properties of Hybrid Nanomembrane/Nanoparticle Heterojunctions: The Role of Inhomogeneous Arrays, J. Phys. Chem. C 120, 6891–6899 (2016).

[Berdiyorov09] G. R. Berdiyorov, M. V. Milošević, F. M. Peeters, Kinematic Vortex-Antivortex Lines in Strongly Driven Superconducting Stripes, Phys. Rev. B 79, 184506, 1–8 (2009).

[Berdiyorov10] G. R. Berdiyorov, M. V. Milošević, F. M. Peeters, Vortices Induced in a Superconducting Loop by Asymmetric Kinetic Inductance and their Detection in Transport Measurements, Phys. Rev. B 81, 144511, 1–5 (2010).

[Bermudez09] E. Bermúdez Ureña, Y. Mei, E. Coric, D. Makarov, M. Albrecht, O. G. Schmidt, Fabrication of Ferromagnetic Rolled-Up Microtubes for Magnetic Sensors on fluids, J. Phys. D: Appl. Phys. 42, 055001, 1–8 (2009).

[Berry87] M. V. Berry, Interpreting the Anholonomy of Coiled Light, Nature 326, 277–278 (1987).

[Bi12] K. Bi, J. Wang, Y. Wang, J. Sha, Z. Wang, M. Chen, Y. Chen, The Thermal Conductivity of SiGe Heterostructure Nanowires with Different Cores and Shells, Phys. Lett. A, 376, 2668–2671 (2012).

[Blakemore75] R. Blakemore, Magnetotactic Bacteria, Science 190, 377–379 (1975).

[Bliokh07] K. Y. Bliokh, D. Y. Frolov, Y. A. Kravtsov, Non-Abelian Evolution of Electromagnetic Waves in a Weakly Anisotropic Inhomogeneous Medium, Phys. Rev. A 75, 053821, 1–11 (2007).

[Bliokh08] K. Y. Bliokh, A. Niv, V. Kleiner, E. Hasman, Geometrodynamics of Spinning Light, Nat. Photonics 2, 748–753 (2008).

[Bogdanov89] A. N. Bogdanov, D. A. Yablonskii, Thermodynamically Stable “Vortices” in Magnetically Ordered Crystals. The Mixed State of Magnets, Sov. Phys. JETP 68, 101–103 (1989).

[Bogdanov01] A. N. Bogdanov, U. K. Rossler, Chiral Symmetry Breaking in Magnetic Thin Films and Multilayers, Phys. Rev. Lett. 87, 037203, 1–4 (2001).

[Bolanos12] V. A. Bolaños Quiñones, L. Ma, S. Li, M. Jorgensen, S. Kiravittaya, O. G. Schmidt, Enhanced Optical Axial Confinement in Asymmetric Microtube Cavities Rolled Up from Circular-Shaped Nanomembranes. Opt. Lett. 37, 4284–4286 (2012).

[Bondi10] R. J. Bondi, S. Lee, G. S. Hwang, First-principles Study of the Mechanical and Optical Properties of Amorphous Hydrogenated Silicon and Silicon-Rich Silicon Oxide, Phys. Rev. 81, 195207, 1–10 (2010).

[Burlachkov93] L. Burlachkov, Flux Creep Through the Surface Barrier and Columnar Defects in HTSC, Physica A 200, 403–412 (1993).

[Burlachkov94] L. Burlachkov, V. B. Geshkenbein, A. E. Koshelev, A. I. Larkin, V. M. Vinokur, Giant Flux Creep Through Surface Barriers and the Irreversibility Line in High-Temperature Superconductors, Phys. Rev. B 50, 16770–16773 (1994).

C

[Cahill87] D. G. Cahill, R. O. Pohl, Thermal Conductivity of Amorphous Solids Above the Plateau, Phys. Rev. 8 35, 4067–4073 (1987).

[Callaway59] J. Callaway, Model for Lattice Thermal Conductivity at Low Temperatures, Phys. Rev. 113, 1046–1051 (1959).

[Carcia85] P. F. Carcia, A. D. Meinhaldt, A. Suna, Perpendicular Magnetic Anisotropy in Pd/Co Thin Film Layered Structures, Appl. Phys. Lett. 47, 178–180 (1985).

[Carillo10] F. Carillo, G. Papari, D. Stornaiuolo, D. Born, D. Montemurro, P. Pingue, F. Beltram, F. Tafuri, Little-Parks Effect in Single Nanoscale, $YBa_2Cu_3O_{6+x}$ rings, Phys. Rev. B 81, 054505, 1–6 (2010).

[Castelvecchi17] D. Castelvecchi, The Strange Topology That Is Reshaping Physics, Nature 547, 272–274 (2017).

[Cebers06] A. Cēbers, M. Ozols, Dynamics of an Active Magnetic Particle in a Rotating Magnetic Field, Phys. Rev. E 73, 021505, 1–5 (2006).

[Chang13] C.-Z. Chang, J. Zhang, X. Feng, J. Shen, Z. Zhang, M. Guo, K. Li, Y. Ou, P. Wei, -L.-L. Wang, Z.-Q. Ji, Y. Feng, S. Ji, X. Chen, J. Jia, X. Dai, Z. Fang, S.-C. Zhang, K. He, Y. Wang, L. Lu, X.-C. Ma, Q.-K. Xue, Experimental Observation of the Quantum Anomalous Hall Effect in a Magnetic Topological Insulator, Science 340, 167–170 (2013).

[Chiliotte09] C. Chiliotte, D. Pérez Daroca, G. Pasquini, V. Bekeris, C.-P. Li, F. Casanova, J. E. Villegas, I. K. Schuller, Commensurability Effects in Magnetic Properties of Superconducting Nb Thin Films with Periodic Submicrometric Pores, Physica B 404, 2809–2811 (2009).

[Chumakov11] A. I. Chumakov, G. Monaco, A. Monaco, W. A. Crichton, A. Bosak, R. Rüffer, A. Meyer, F. Kargl, L. Comez, D. Fioretto, H. Giefers, S. Roitsch, G. Wortmann, M. H. Manghnani, A. Hushur, Q. Williams, J. Balogh, K. Parliński, P. Jochym, P. Piekarz, Equivalence of the Boson Peak in Glasses to the Transverse Acoustic van Hove Singularity in Crystals, Phys. Rev. Lett 106, 225501, 1–5 (2011).

[Clanet04] C. Clanet, P. Hèraud, G. Searby, On the Motion of Bubbles in Vertical Tubes of Arbitrary Cross-Sections: Some Complements to the Dumitrescu-Taylor Problem, J. Fluid Mech. 519, 359–376 (2004).

[Clark10] K. Clark, A. Hassanien, S. Khan, K.-F. Braun, H. Tanaka, S.-W. Hla, Superconductivity in just Four Pairs of $(BETS)_2GaCl_4$ Molecules, Nat. Nanotechnol. 5, 261–265 (2010).

[Clem10] J. R. Clem, A. P. Malozemoff, Theory of ac Loss in Power Transmission Cables with Second Generation High Temperature Superconductor Wires, Supercond. Sci. Technol. 23, 034014, 1–6 (2010).

[Cocemasov15] A. I. Cocemasov, D. L. Nika, V. M. Fomin, D. Grimm, O. G. Schmidt, Phonon-engineered Thermal Transport in Si Wires with Constant and Periodically Modulated Cross-Sections: A Crossover between Nano- And Microscale Regimes, Appl. Phys. Lett. 107, 011904, 1–5 (2015).

[Cole06] D. Cole, S. Bending, S. Savel'ev, A. Grigorenko, T. Tamegai, F. Nori, Ratchet without Spatial Asymmetry for Controlling the Motion of Magnetic Flux Quanta using Time-Asymmetric Drives, Nat. Mater. 5, 305–311 (2006).

[Cordoba13] R. Córdoba, T. I. Baturina, J. Sesé, A. Y. Mironov, J. M. De Teresa, M. R. Ibarra, D. A. Nasimov, A. K. Gutakovskii, A. V. Latyshev, I. Guillamón, H. Suderow, S. Vieira, M. R. Baklanov, J. J. Palacios, V. M. Vinokur, Magnetic field-Induced Dissipation-Free State in Superconducting Nanostructures. Nat. Commun. 4, 1437, 1–7 (2013).

[Cordoba19] R. Córdoba, D. Mailly, R. O. Rezaev, E. I. Smirnova, O. G. Schmidt, V. M. Fomin, U. Zeitler, I. Guillamón, H. Suderow, J. M. De Teresa, Three-dimensional Superconducting Nanohelices Grown by He^+-Focused-ion-beam Direct Writing, Nano Lett. 19, 8597–8604 (2019).

D

[DeGennes66] P. G. De Gennes, *Superconductivity of Metals and Alloys*, W. A. Benjamin, New York, 1966, 274.

[Deneke04] C. Deneke, N.-Y. Jin-Phillipp, I. Loa, O. G. Schmidt, Radial Superlattices and Single Nanoreactors. Appl. Phys. Lett. 84, 4475–4477 (2004).

[Deneke07] C. Deneke, W. Sigle, U. Eigenthaler, P. A. van Aken, G. Schütz, O. G. Schmidt, Interfaces in semiconductor/Metal Radial Superlattices, Appl. Phys. Lett. 90, 263107, 1–3 (2007).

[Deneke09] C. Deneke, R. Songmuang, N. Y. Jin-Phillipp, O. G. Schmidt, The Structure of Hybrid Radial Superlattices, J. Phys. D: Appl. Phys. 42, 103001, 1–16 (2009).

[DeWitt79] B. S. DeWitt, C. F. Hart, C. J. Isham, Topology and Quantum Field Theory, Physica 96A, 197–211 (1979).

[Dobrovolskiy12] O. V. Dobrovolskiy, M. Huth, Crossover from Dirty to Clean Superconducting Limit in dc Magnetron-Sputtered Thin Nb Films, Thin Solid Films 520, 5985–5990 (2012).

[Donadio09] D. Donadio, G. Galli, Atomistic Simulations of Heat Transport in Silicon Nanowires, Phys. Rev. Lett. 102, 195901, 1–4 (2009).

[Dong06] L. X. Dong, L. Zhang, D. J. Bell, B. J. Nelson, D. Grützmacher, Hybrid Nanorobotic Approaches for Fabricating NEMS from 3D Helical Nanostructures. Proceedings 2006 IEEE International Conference on Robotics and Automation (ICRA 2006), Orlando, Florida, 1396–1401 (2006).

[Dorenbos08] S. N. Dorenbos, E. M. Reiger, N. Akopian, U. Perinetti, V. Zwiller, T. Zijlstra, T. M. Klapwijk, Superconducting Single Photon Detectors with Minimized Polarization Dependence, Appl. Phys. Lett. 93, 161102, 1–3 (2008).

[Dresselhaus07] M. S. Dresselhaus, G. Chen, M. Y. Tang, R. G. Yang, H. Lee, D. Z. Wang, Z. F. Ren, J.-P. Fleurial, P. Gogna, New Directions for Low-Dimensional Thermoelectric Materials, Adv. Mater. 19, 1043–1053 (2007).

E

[Ederer07] C. Ederer, N. A. Spaldin, Towards a Microscopic Theory of Toroidal Moments in Bulk Periodic Crystals, Phys. Rev. B 76, 214404, 1–13 (2007).

[Embon15] L. Embon, Y. Anahory, A. Suhov, D. Halbertal, J. Cuppens, A. Yakovenko, A. Uri, Y. Myasoedov, M. L. Rappaport, M. E. Huber, A. Gurevich, E. Zeldov, Probing Dynamics and Pinning of Single Vortices in Superconductors At Nanometer Scales, Sci. Rep. 5, 7598, 1–9 (2015).

[Enachi16] M. Enachi, M. Guix, V. Postolache, V. Ciobanu, V. M. Fomin, O. G. Schmidt, I. Tiginyanu, Light-induced Motion of Microengines based on Microarrays of TiO_2 Nanotubes, Small 12, 5497–5505 (2016).

[Engel03] A. Engel, H. W. Müller, P. Reimann, A. Jung, Ferrofluids as Thermal Ratchets, Phys. Rev. Lett. 91, 060602, 1–4 (2003).

[Erglis07] K. Ērglis, Q. Wen, V. Ose, A. Zeltins, A. Sharipo, P. A. Janmey, A. Cēbers, Dynamics of Magnetotactic Bacteria in a Rotating Magnetic Field, J. Biophys. 93, 1402–1412 (2007).

[Eschrig11] H. Eschrig, *Topology and Geometry for Physics, Lecture Notes in Physics*, 822, Springer, Berlin–Heidelberg, 2011, 404.
[Esposito14] M. Esposito, V. Tasco, F. Todisco, A. Benedetti, D. Sanvitto, A. Passaseo, Three Dimensional Chiral Metamaterial Nanospirals in the Visible Range by Vertically Compensated Focused Ion Beam Induced-Deposition, Adv. Opt. Mater. 2, 154–161 (2014).

F

[Feynman63] R. P. Feynman, R. B. Leighton, M. Sands, *The Feynman Lectures on Physics*, II, Addison-Wesley, Reading, Massachusetts, 1963, 566 (Part 2, Section 41–4).
[Fomin09] V. M. Fomin, R. Wördenweber, Vortex Dynamics in high-Tc Superconducting Films with Arrays of Antidots, SPIE Nanotechnology IV 7364, 73640P, 1–9 (2009).
[Fomin11] V. M. Fomin, E. J. Smith, D. Makarov, S. Sanchez, O. G. Schmidt, Dynamics of Radial-Magnetized Microhelix Coils, Phys. Rev. B 84, 174303, 1–7 (2011).
[Fomin12a] V. M. Fomin, R. R. O. Rezaev, O. G. Schmidt, Tunable Generation of Correlated Vortices in Open Superconductor Tubes, Nano Lett. 12, 1282–1287 (2012).
[Fomin12b] V. M. Fomin, S. Kiravittaya, O. G. Schmidt, Electron Localization in Inhomogeneous Möbius Rings, Phys. Rev. B 86, 195421, 1–6 (2012).
[Fomin13] V. M. Fomin, E. J. Smith, D. D. Karnaushenko, D. Makarov, O. G. Schmidt, Asymmetric Drag in Oscillatory Motion: Ratchet Effect Without an Asymmetric Potential. Phys. Rev. E 87, 052122, 1–5 (2013).
[Fomin14] V. M. Fomin, M. Hippler, V. Magdanz, L. Soler, S. Sanchez, O. G. Schmidt, Propulsion Mechanism of Catalytic Microjet Engines, IEEE Trans. Rob. 30, 40–48 (2014).
[Fomin15] V. M. Fomin, A. A. Balandin, Phonon Spectrum Engineering in Rolled-up Micro- and Nano-Architectures, Appl. Sci. 5, 728–746 (2015).
[Fomin17] V. M. Fomin, R. O. Rezaev, E. A. Levchenko, D. Grimm, O. G. Schmidt, Superconducting Nanostructured Microhelices, J. Phys.: Condens. Matter. 29, 395301, 1–9, (2017).
[Fomin18a] V. M. Fomin (Editor), *Physics of Quantum Rings*, Springer, Berlin–Heidelberg, 2014, 487; *Physics of Quantum Rings*, 2nd Edition, Springer International Publishing, Cham, 2018, 586.
[Fomin18b] V. M. Fomin, Topology-driven effects in advanced nanoarchitectures, In: A. Sidorenko (Ed.), *Functional Nanostructures and Metamaterials*, Springer International Publishing, Cham, 2018, 195–220.
[Fomin18c] V. M. Fomin, Tailoring Electron and Phonon Energy Dispersion and Thermal Transport in Nano- and Microarchitectures, Moldavian J. Phys. Sci. 17, 121–131 (2018).

G

[Gao06] P. X. Gao, W. J. Mai, Z. L. Wang, Superelasticity and Nanofracture Mechanics of ZnO Nanohelices, Nano Lett. 6, 2536–2543 (2006).
[Gao11] P.-X. Gao, G. Liu, Helical Nanostructures: Synthesis and Potential Applications, In: W. Zhou, Z.L. Wang, (Eds.), *Three-Dimensional Nanoarchitectures: Designing Next-Generation Devices*, Springer, Berlin, 2011, 167–205.
[Gao12] W. Gao, S. Sattayasamitsathit, J. Wang, Catalytically Propelled Micro-/Nanomotors: How Fast can they Move? Chem. Rec. 12, 224–231 (2012).
[Garber76] M. Garber, J. F. Bussiere, G. H. Morgan, Design of Double Helix Conductors for Superconducting AC Power Transmission, AIP Conf. Proc. 34, 84–86 (1976).

[Ge15] J.-Y. Ge, J. Gutierrez, V. N. Gladilin, J. T. Devreese, V. V. Moshchalkov, Bound Vortex Dipoles Generated at Pinning Centres by Meissner Current, Nat. Commun. 6, 6573, 1–8 (2015).
[Ghamsari13] B. G. Ghamsari, J. Abrahams, S. Remillard, S. M. Anlage, High-Temperature Superconducting Spiral Resonator for Metamaterial Applications, IEEE Trans. Appl. Supercond. 23, 1500304, 1–4 (2013).
[Gladilin08] V. N. Gladilin, J. Tempere, I. F. Silvera, J. T. Devreese, V. V. Moshchalkov, Vortices on a Superconducting Nanoshell: Phase Diagram and Dynamics, Phys. Rev. B 77, 024512, 1–9 (2008).
[Gladilin12] V. N. Gladilin, J. Tempere, J. T. Devreese, V. V. Moshchalkov, Aharonov-Bohm Oscillations in the Vortex Dynamics in Superconducting Hollow Cylinders, Phys. Rev. B. 86, 104508, 1–5 (2012).
[Gol'tsman01] G. N. Gol'tsman, O. Okunev, G. Chulkova, A. Lipatov, A. Semenov, K. Smirnov, B. Voronov, A. Dzardanov, C. Williams, R. Sobolewski, Picosecond Superconducting Single-Photon Optical Detector, Appl. Phys. Lett. 79, 705–707 (2001).
[Graff91] K. F. Graff, *Wave Motion in Elastic Solids*, Dover, New York, 1991, 688.
[Grest84] G. S. Grest, S. R. Nagel, A. Rahman, Zone boundaries in glasses, Phys. Rev. B 29, 5968–5971 (1984).
[Grigorieva07] I. V. Grigorieva, W. Escoffier, V. R. Misko, B. J. Baelus, F. M. Peeters, L. Y. Vinnikov, S. V. Dubonos, Pinning-Induced Formation of Vortex Clusters and Giant Vortices in Mesoscopic Superconducting Disks, Phys. Rev. Lett. 99, 147003, 1–4 (2007).
[Grimm14] D. Grimm, R. B. Wilson, B. Teshome, S. Gorantla, M. H. Rümmeli, T. Bublat, E. Zallo, G. Li, D. G. Cahill, O. G. Schmidt, Thermal Conductivity of Mechanically Joined Semiconducting/Metal Nanomembrane Superlattices, Nano Lett. 14, 2387–2393 (2014).
[Gropp96] W. D. Gropp, H. G. Kaper, G. K. Leaf, D. M. Levine, M. Palumbo, V. M. Vinokur, Numerical Simulation of Vortex Dynamics in Type-II Superconductors, J. Comput. Phys. 123, 254–266 (1996).

H

[Happel83] J. Happel, H. Brenner, *Low Reynolds number hydrodynamics*, 2nd ed., Martinus Nijhoff Publishers, The Hague, 1983, 553.
[Harazim12] S. M. Harazim, V. A. B. Quiñones, S. Kiravittaya, S. Sanchez, O. G. Schmidt, Lab-in-a-tube: On-Chip Integration of Glass Optofluidic Ring Resonators for Label-Free Sensing Applications, Lab Chip 2, 2649, 1–7 (2013).
[Hashimoto89] S. Hashimoto, Y. Ochiai, K. Aso, Perpendicular Magnetic Anisotropy and Magnetostriction of Sputtered Co/Pd and Co/Pt Multilayered Films, J. Appl. Phys. 66, 4909–4916 (1989).
[He12] Y. He, G. Galli, Microscopic Origin of the Reduced Thermal Conductivity of Silicon Nanowires, Phys. Rev. Lett. 108, 215901, 1–5 (2012).
[Helgesen90] G. Helgesen, P. Pieranski, A. T. Skjeltorp, Nonlinear Phenomena in Systems of Magnetic Holes, Phys. Rev. Lett. 64, 1425–1428 (1990).
[Henrich12] D. Henrich, P. Reichensperger, M. Hofherr, J. M. Meckbach, K. Il'in, M. Siegel, A. Semenov, A. Zotova, D. Y. Vodolazov, Geometry-induced reduction of the critical current in superconducting nanowires, Phys. Rev. B 86, 144504, 1–5 (2012).
[Henrich13a] D. Henrich, *Influence of Material and Geometry on the Performance of Superconducting Nanowire Single-Photon Detectors*, KIT Scientific Publishing, Karlsruhe, 2013, 195.
[Henrich13b] D. Henrich, L. Rehm, S. Dörner, M. Hofherr, K. Il'in, A. Semenov, M. Siegel, Detection Efficiency of a Spiral-Nanowire Superconducting Single-Photon Detector, IEEE Trans. Appl. Supercond. 23, 2200405, 1–5 (2013).

[Hicks93] L. Hicks, M. Dresselhaus, Effect of Quantum-Well Structures on the Thermoelectric Figure of Merit, Phys. Rev. B 47, 12727–12731 (1993).
[Hilgenkamp03] H. Hilgenkamp, V. V. Moshchalkov, P. Kes, Flux Quanta on the Move, Science 302, 1159–1160 (2003).
[Hu11a] X.-H. Hu, A.-C. Ji, X.-G. Qiu, W.-M. Liu, Effects of Geometrical Symmetry on the Vortex in Mesoscopic Superconductors, Eur. Phys. J. B 79, 473–477 (2011).
[Hu11b] M. Hu, K. P. Giapis, J. V. Goicochea, X. Zhang, D. Poulikakos, Significant Reduction of Thermal Conductivity in Si/Ge core-shell Nanowires. Nano Lett. 11, 618–623 (2011).
[Huth18] M. Huth, F. Porrati, O. V. Dobrovolskiy, Focused Electron Beam Induced Deposition Meets Materials Science, Microelectron Eng. 185–186, 9–28 (2018).
[Hwang08] G. Hwang, C. Dockendorf, D. J. Bell, L. X. Dong, H. Hashimoto, D. Poulikakos, B. J. Nelson, 3-D InGaAs/GaAs Helical Nanobelts for Optoelectronic Devices, Int. J. Optomechatronics 2, 88–103 (2008).

I

[Intel08] Intel® Visual Fortran with Microsoft Visual Studio (2008). https://www.visualstudio.com/
[Ioffe98] Electronic archive New Semiconductor Materials. Characteristics and Properties © 1998–2001 by Ioffe Institute. http://www.ioffe.ru/SVA/NSM/Semicond/
[Ivlev84] B. I. Ivlev, N. B. Kopnin, Theory of Current States in Narrow Superconducting Channel, Sov. Phys. Usp. 27, 206–227 (1984).

K

[Kanyinda08] C. Kanyinda-Malu, F. J. Clares, R. M. de la Cruz, Axial Interface Optical Phonon Modes in a Double-Nanoshell System, Nanotechnology 19, 285713, 1–8 (2008).
[Kargar16] F. Kargar, B. Debnath, J.-P. Kakko, A. Säynätjoki, H. Lipsanen, D. L. Nika, R. K. Lake, A. A. Balandin, Direct Observation of Confined Acoustic Phonon Polarization Branches in Free-Standing Semiconductor Nanowires, Nat. Commun. 7, 13400, 1–7 (2016).
[Karnauschenko20] D. Karnaushenko, T. Kang, V. K. Bandari, F. Zhu, O. G. Schmidt, 3D Self-Assembled Microelectronic Devices: Concepts, Materials, Applications, Adv. Mater. 32, 1902994, 1–30 (2020).
[Kato93] R. Kato, Y. Enomoto, S. Maekawa, Effects of the Surface Boundary on the Magnetization Process in Type-II Superconductors, Phys. Rev. B 47, 8016–8024 (1993).
[Kern17] C. Kern, M. Kadic, M. Wegener, Experimental Evidence for Sign Reversal of the Hall Coefficient in Three-Dimensional Metamaterials, Phys. Rev. Lett. 118, 016601, 1–5 (2017).
[Ketterson99] J. B. Ketterson, S. N. Song, *Superconductivity*, Cambridge University Press, 1999, Cambridge, 497.
[Kirkpatrick73] S. Kirkpatrick, Percolation and Conduction, Rev. Mod. Phys. 45, 574–588 (1973).
[Klemens94] P. G. Klemens, D. F. Pedraza, Thermal Conductivity of Graphite in the Basal Plane, Carbon 32, 735–741 (1994).
[Klimin94] S. N. Klimin, E. P. Pokatilov, V. M. Fomin, Bulk and Interface Polarons in Quantum Wires and Dots, Phys. Stat. Sol. (b) 184, 373–383 (1994).
[Klingner17] A. Klingner, I. Khalil, V. Magdanz, V. M. Fomin, O. G. Schmidt, S. Misra, Modeling of Unidirectional-Overloaded Transition in Catalytic Tubular Microjets, J. Phys. Chem. C 121, 14854–14863 (2017).

[Klitzing80] K. von Klitzing, G. Dorda, M. Pepper, New Method for High-Accuracy Determination of the Fine-Structure Constant Based on Quantized Hall Resistance, Phys. Rev. Lett. 45, 494–497 (1980).
[Kogut79] J. B. Kogut, An Introduction to Lattice Gauge Theory and Spin Systems, Rev. Mod. Phys. 51, 659–713 (1979).
[König07] M. König, S. Wiedmann, C. Brüne, A. Roth, H. Buhmann, L. W. Molenkamp, X.-L. Qi, S.-C. Zhang, Quantum Spin Hall Insulator State in HgTe Quantum Wells, Science 318, 766–770 (2007).
[Kong04] X. Y. Kong, Y. Ding, R. Yang, Z. L. Wang, Single-Crystal Nanorings Formed by Epitaxial Self-Coiling of Polar Nanobelts, Science 303, 1348–1351 (2004).
[Krause06] B. Krause, C. Mocuta, T. H. Metzger, C. Deneke, O. G. Schmidt, Local Structure of a Rolled-Up Single Crystal: An X-ray Microdiffraction Study of Individual Semiconductor Nanotubes, Phys. Rev. Lett. 96, 165502, 1–4 (2006).
[Kravchuk16] V. P. Kravchuk, U. K. Rößler, O. M. Volkov, D. D. Sheka, J. van den Brink, D. Makarov, H. Fuchs, H. Fangohr, Y. Gaididei, Topologically Stable Magnetization States on a Spherical Shell: Curvature-Stabilized Skyrmions, Phys. Rev. B 94, 144402, 1–11 (2016).
[Kurter10] C. Kurter, J. Abrahams, S. M. Anlage, Miniaturized Superconducting Metamaterials for Radio Frequencies, Appl. Phys. Lett. 96, 253504, 1–3 (2010).

L

[Lara15] A. Lara, F. G. Aliev, A. V. Silhanek, V. V. Moshchalkov, Microwave-stimulated Superconductivity due to Presence of Vortices, Sci. Rep. 5, 9187, 1–5 (2015).
[Larkin13] J. M. Larkin, A. J. H. McGaughey, Predicting Alloy Vibrational Mode Properties Using Lattice Dynamics Calculations, Molecular Dynamics Simulations, and the Virtual Crystal Approximation, J. Appl. Phys. 114, 023507, 1–14 (2013).
[Le Bellac06] M. Le Bellac, *Quantum Physics*, Cambridge University Press, Cambridge, 2006, 585.
[Lee99] C.-S. Lee, B. Jankó, I. Derényi, A.-L. Barabási, Reducing Vortex Density in Superconductors using the 'Ratchet Effect', Nature 400, 337–340 (1999).
[Lee09] M. Lee, W. Kang, Y. Onose, Y. Tokura, N. P. Ong, Unusual Hall Effect Anomaly in MnSi under Pressure, Phys. Rev. Lett. 102, 186601, 1–4 (2009).
[Lemberger07] T. R. Lemberger, I. Hetel, J. W. Knepper, F. Y. Yang, Penetration depth study of very thin superconducting Nb films, Phys. Rev. B 76, 094515, 1–4 (2007).
[Li11] J. Li, G. Huang, M. Ye, M. Li, R. Liu, Y. Mei, Dynamics of Catalytic Tubular Microjet Engines: Dependence on Geometry and Chemical Environment, Nanoscale 3, 5083–5089 (2011).
[Li13] S. L. Li, L. B. Ma, V. M. Fomin, S. Böttner, M. R. Jorgensen, O. G. Schmidt, Non-integer Optical Modes in a Möbius-ring Resonator, arXiv: 1311.7158 [physics.optics], 1–9 (2013).
[Li14] L. Li, J. Wang, T. Li, W. Song, G. Zhang, Hydrodynamics and Propulsion Mechanism of Self-Propelled Catalytic Micromotors: Model and Experiment, Soft Matter 10, 7511–7518 (2014).
[Li15] L. Li, J. Wang, T. Li, W. Song, G. Zhang, A Unified Model of Drag Force for Bubble-Propelled Catalytic Micro/Nano-Motors with Different Geometries in Low Reynolds Number Flows, J. Appl. Phys. 117, 104308, 1–6 (2015).
[Li17] G. Li, M. Yarali, A. Cocemasov, S. Baunack, D. L. Nika, V. M. Fomin, S. Singh, T. Gemming, F. Zhu, A. Mavrokefalos, O. G. Schmidt, In-Plane Thermal Conductivity of Radial and Planar Si/SiO_x Hybrid Nanomembrane Superlattices, ACS Nano 11, 8215–8222 (2017).
[Little62] W. A. Little, R. D. Parks, Observation of Quantum Periodicity in the Transition Temperature of a Superconducting Cylinder, Phys. Rev. Lett. 9, 9–12 (1962).

[Lösch19] S. Lösch, A. Alfonsov, O. V. Dobrovolskiy, R. Keil, V. Engemaier, S. Baunack, G. Li, O. G. Schmidt, D. Bürger, Microwave Radiation Detection with an Ultrathin Free-Standing Superconducting Niobium Nanohelix, ACS Nano 13, 2948–2955 (2019).
[Loutherback09] K. Loutherback, J. Puchalla, R. H. Austin, J. C. Sturm, Deterministic Microfluidic Ratchet, Phys. Rev. Lett. 102, 045301, 1–4 (2009).
[Lu16] L. Lu, J. D. Joannopoulos, M. Soljačić, Topological States in Photonic Systems, Nat. Phys. 12, 626–629 (2016).

M

[Ma05] Y. Ma, J. S. Tse, T. Cui, D. D. Klug, L. Zhang, Y. Xie, Y. Niu, G. Zou, First-principles Study of Electron-Phonon Coupling in Hole- and Electron-Doped Diamonds in the Virtual Crystal Approximation, Phys. Rev. B 72, 014306, 1–9 (2005).
[Ma16a] L. B. Ma, S. L. Li, V. M. Fomin, M. Hentschel, J. B. Götte, Y. Yin, M. R. Jorgensen, O. G. Schmidt, Spin–orbit Coupling of Light in Asymmetric Microcavities, Nat. Commun. 7, 10983, 1–6 (2016).
[Ma16b] X. Ma, A. C. Hortelao, A. Miguel-López, S. Sánchez, Bubble-Free Propulsion of Ultrasmall Tubular Nanojets Powered by Biocatalytic Reactions, J. Am. Chem. Soc. 138, 13782–13785 (2016).
[Madani15] A. Madani, M. Kleinert, D. Stolarek, L. Zimmermann, L. Ma, O. G. Schmidt, Vertical Optical Ring Resonators Fully Integrated with Nanophotonic Waveguides on Silicon-On-Insulator Substrates, Opt. Lett. 40, 3826–3829 (2015).
[Madani17] A. Madani, S. M. Harazim, V. A. B. Quiñones, M. Kleinert, A. Finn, E. S. G. Naz, L. Ma, O. G. Schmidt, Optical Microtube Cavities Monolithically Integrated on Photonic Chips for Optofluidic Sensing, Opt. Lett. 42, 486–489 (2017).
[Mallouk09] T. E. Mallouk, A. Sen, Powering Nanorobots, Sci. Am. 300, 72–77 (2009).
[Manjare12] M. Manjare, B. Yang, Y. P. Zhao, Bubble Driven Quasioscillatory Translational Motion of Catalytic Micromotors, Phys. Rev. Lett. 109, 128305, 1–5 (2012).
[Manjare13] M. T. Manjare, B. Yang, Y. Zhao, Bubble Propelled Microjets: Model and Experiment, J. Phys. Chem. C 117, 4657–4665 (2013).
[Matsuo07] S. Matsuo, K. Furuta, T. Fujii, K. Nagai, N. Hatakenaka, Fluxon-based Gate Controls of Capacitively Coupled Flux-Based-Phase Qubits, Appl. Phys. Lett. 91, 093103, 1–3 (2007).
[Maxfield65] B. W. Maxfield, W. L. McLean, Superconducting Penetration Depth of Niobium, Phys. Rev. 139, A1515–A1522 (1965).
[Medina16] M. Medina-Sánchez, B. Ibarlucea, N. Pérez, D. D. Karnaushenko, S. M. Weiz, L. Baraban, G. Cuniberti, O. G. Schmidt, High-Performance Three-Dimensional Tubular Nanomembrane Sensor for DNA Detection, Nano Lett. 16, 4288–4296 (2016).
[Medina17] M. Medina-Sánchez, O. G. Schmidt, Medical Microbots Need Better Imaging and Control, Nature 545, 406–408 (2017).
[Medina18] M. Medina-Sánchez, V. Magdanz, M. Guix, V. M. Fomin, O. G. Schmidt, Swimming Microrobots: Soft, Reconfigurable and Smart, Adv. Funct. Mater. 28, 1707228, 1–27 (2018).
[Mei08] Y. Mei, G. Huang, A. A. Solovev, E. B. Ureña, I. Mönch, F. Ding, T. Reindl, R. K. Y. Fu, P. K. Chu, O. G. Schmidt, Versatile Approach for Integrative and Functionalized Tubes by Strain Engineering of Nanomembranes on Polymers, Adv. Mater. 20, 4085–4090 (2008).
[Mei11] Y. Mei, A. A. Solovev, S. Sanchez, O. G. Schmidt, Rolled-up Nanotech on Polymers: From Basic Perception to Self-Propelled Catalytic Microengines, Chem. Soc. Rev. 40, 2109–2119 (2011).
[Merriam-Webster20] https://www.merriam-webster.com/dictionary/self-rolled.

[Meservey72] R. Meservey, L. Meyers, Phase Transition of Thin-Film Superconducting Cylinders in a Magnetic Field. II. Angular Dependence, Phys. Rev. B 6, 2632–2642 (1972).
[Miao15] S. Miao, D. Chen, A. Madani, M. R. Jorgensen, V. A. Bolaños Quiñones, L. Ma, S. G. Hickey, A. Eychmüller, O. G. Schmidt, Optofluidic Sensor: Evaporation Kinetics Detection of Solvents Dissolved with Cd_3P_2 Colloidal Quantum Dots in a Rolled-Up Microtube, Adv. Opt. Mater. 3, 187–193 (2015).
[Migler91] K. B. Migler, R. B. Meyer, Solitons and Pattern Formation in Liquid Crystals in a Rotating Magnetic Field, Phys. Rev. Lett. 66, 1485–1488 (1991).
[Migler94] K. B. Migler, R. B. Meyer, Spirals in Liquid Crystals in a Rotating Magnetic Field, Physica D 71, 412–420 (1994).
[Midgley09] P. A. Midgley, R. E. Dunin-Borkowski, Electron Tomography and Holography in Materials Science, Nature Mater. 8, 271–280 (2009).
[Milosevic10] M. V. Milošević, F. M. Peeters, Vortex Manipulation in a Superconducting Matrix with View on Applications, Appl. Phys. Lett. 96, 192501, 1–3 (2010).
[Mingo03] N. Mingo, Calculation of Si Nanowire Thermal Conductivity Using Complete Phonon Dispersion Relations, Phys. Rev. B 68, 113308, 1–4 (2003).
[Mirkovic10] T. Mirkovic, N. S. Zacharia, G. D. Scholes, G. A. Ozin, Fuel for Thought: Chemically Powered Nanomotors Out-Swim Nature's Flagellated Bacteria, ACS Nano 4, 1782–1789 (2010).
[Misko09] V. R. Misko, H. J. Zhao, F. M. Peeters, V. Oboznov, S. V. Dubonos, I. V. Grigorieva, Formation of Vortex Shells in Mesoscopic Superconducting Squares, Supercond. Sci. Technol. 22, 034001, 1–8 (2009).
[Moshchalkov95] V. V. Moshchalkov, L. Gielen, C. Strunk, R. Jonckheere, X. Qiu, C. Van Haesendonck, Y. Bruynseraede, Effect of Sample Topology on the Critical Fields of Mesoscopic Superconductors, Nature 373, 319–322 (1995).
[Motojima90] S. Motojima, M. Kawaguchi, K. Nozaki, H. Iwanaga, Dynamics of Photoreflectance from Undoped GaAs, Appl. Phys. Lett. 56, 321–323 (1990).
[Mukoyama06] S. Mukoyama, M. Yagi, H. Hirano, Y. Yamada, T. Izumi, Y. Shiohara, Development of HTS Power Cable Using YBCO Coated Conductor, Physica C 445–448, 1050–1053 (2006).

N

[Natarajan12] C. M. Natarajan, M. G. Tanner, R. H. Hadfield, Superconducting Nanowire Single-Photon Detectors: Physics and Applications, Supercond. Sci. Technol. 25, 063001, 1–16 (2012).
[Neogi15] S. Neogi, J. S. Reparaz, L. F. C. Pereira, B. Graczykowski, M. R. Wagner, M. Sledzinska, A. Shchepetov, M. Prunnila, J. Ahopelto, C. M. Sotomayor-Torres, D. Donadio, Tuning Thermal Transport in Ultrathin Silicon Membranes by Surface Nanoscale Engineering, ACS Nano 9, 3820–3828 (2015).
[Neuman08] K. C. Neuman, A. Nagy, Single-Molecule Force Spectroscopy: Optical Tweezers, Magnetic Tweezers and Atomic Force Microscopy, Nat. Methods 5, 491–505 (2008).
[Nika09] D. L. Nika, N. D. Zincenco, E. P. Pokatilov, Engineering of Thermal Fluxes in Phonon Mismatched Heterostructures, J. Nanoelect. Optoelect. 4, 180–185 (2009).
[Nika12] D. L. Nika, A. I. Cocemasov, C. I. Isacova, A. A. Balandin, V. M. Fomin, O. G. Schmidt, Suppression of Phonon Heat Conduction in Cross-Section-Modulated Nanowires, Phys. Rev. B 85, 205439, 1–10 (2012).
[Nishio08] T. Nishio, T. An, A. Nomura, K. Miyachi, T. Eguchi, H. Sakata, S. Lin, N. Hayashi, N. Nakai, M. Machida, Y. Hasegawa, Superconducting Pb Island Nanostructures Studied by Scanning Tunneling Microscopy and Spectroscopy, Phys. Rev. Lett. 101, 167001, 1–4 (2008).

[Nobel16] The Nobel Prize in Physics 2016. https://www.nobelprize.org/prizes/physics/2016/summary/
[Noji07] H. Noji, Self-field Losses in 1 m HTS Conductor Consisted of YBCO Tapes, Cryogenics 47, 343–347 (2007).
[Nord19] M. Nord, A. Semisalova, A. Kákay, G. Hlawacek, I. MacLaren, V. Liersch, O. M. Volkov, D. Makarov, G. W. Paterson, K. Potzger, J. Lindner, J. Fassbender, D. McGrouther, R. Bali, Strain Anisotropy and Magnetic Domains in Embedded Nanomagnets, Small 15, 1904738, 1–6 (2019).

O

[Ozin05] G. A. Ozin, I. Manners, S. Fournier-Bidoz, A. Arsenault, Dream Nanomachines, Adv. Mater. 17, 3011–3018 (2005).

P

[Pawasche09] C. Pawasche, S. Floyd, M. Sitti, Modeling and Experimental Characterization of an Untethered Magnetic Micro-Robot, Int. J. Robot. Res. 28, 1077–1094 (2009).
[Pokatilov00] E. P. Pokatilov, V. M. Fomin, J. T. Devreese, S. N. Balaban, S. N. Klimin, Bipolaron Binding in Quantum Wires, Phys. Rev. B 61, 2721–2728 (2000).
[Poole95] C. P. Poole, Jr., H. A. Farach, R. J. Creswick, Superconductivity, Academic Press, San Diego, California, 1995, 620 pp.
[Prinz00] V. Y. Prinz, V. A. Seleznev, A. K. Gutakovsky, A. V. Chehovskiy, V. V. Preobrazhenskii, M. A. Putyato, T. A. Gavrilova, Free-standing and Overgrown InGaAs/GaAs Nanotubes, Nanohelices and Their Arrays. Physica E: Low-dimension. Syst. Nanostruct. 6, 828–831 (2000).
[Purcell77] E. M. Purcell, Life at Low Reynolds Number, Amer. J. Phys. 45, 3–11 (1977).
[Pumera11] M. Pumera, Nanomaterials Meet Microfluidics, Chem. Commun. 47, 5671–5680, (2011).
[Pylypovskyi15] O. V. Pylypovskyi, V. P. Kravchuk, D. D. Sheka, D. Makarov, O. G. Schmidt, Y. Gaididei, Coupling of Chiralities in Spin and Physical Spaces: The Möbius Ring as a Case Study, Phys. Rev. Lett. 114, 197204, 1–5 (2015).

R

[Ranzoni10] A. Ranzoni, X. J. A. Janssen, M. Ovsyanko, L. J. van IJzendoorn, M. W. J. Prins, Magnetically Controlled Rotation and Torque of Uniaxial Microactuators for lab-on-a-chip Applications, Lab. Chip. 10, 179–188 (2010).
[Ray13] D. Ray, C. J. O. Reichhardt, B. Jankó, C. Reichhardt, Strongly Enhanced Pinning of Magnetic Vortices in Type-II Superconductors by Conformal Crystal Arrays, Phys. Rev. Lett. 110, 267001, 1–5 (2013).
[Reichhardt97] C. Reichhardt, C. J. Olson, F. Nori, Dynamic Phases of Vortices in Superconductors with Periodic Pinning, Phys. Rev. Lett. 78, 2648–2651 (1997).
[Reichchardt05] C. Reichhardt, C. J. Olson Reichhardt, M. B. Hastings, Glassy Ratchets for Collectively Interacting Particles, Phys. Lett. A 342, 162–167 (2005).
[Reichhardt06] C. Reichhardt, C. J. Olson, M. B. Hastings, Rectification and Phase Locking for Particles on Symmetric Two-Dimensional Periodic Substrates, Phys. Rev. Lett. 89, 024101, 1–4 (2002).
[Rezaev14] R. O. Rezaev, V. M. Fomin, O. G. Schmidt, Vortex Dynamics Controlled by Pinning Centers on Nb Superconductor Open Microtubes, Physica C 497, 1–5 (2014).

[Rezaev15] R. O. Rezaev, E. A. Levchenko, O. G. Schmidt, V. M. Fomin, Dynamics of the Abrikosov Vortices on Cylindrical Microtubes, Russ. Phys. J. 58, 623–628 (2015).
[Rezaev16] R. O. Rezaev, E. A. Levchenko, V. M. Fomin, Branching of the Vortex Nucleation Period in Superconductor Nb Microtubes due to an Inhomogeneous Transport Current, Supercond. Sci. Tech. 29, 045014, 1–7 (2016).
[Rezaev19] R. O. Rezaev, E. A. Posenitskiy, E. I. Smirnova, E. A. Levchenko, O. G. Schmidt, V. M. Fomin, Voltage Induced by Superconducting Vortices in Open Nanostructured Microtubes, Phys. Stat. Sol. RRL 13, 1–12 (2019).
[Rezaev20] R. O. Rezaev, E. I. Smirnova, O. G. Schmidt, V. M. Fomin, Topological Transitions in Superconductor Nanomembranes Under a Strong Transport Current, Communications Physics 3, 144, 1–8 (2020).
[Riwar16] R.-P. Riwar, M. Houzet, J. S. Meyer, Y. V. Nazarov, Multi-terminal Josephson Junctions as Topological Matter, Nat. Commun. 7, 11167, 1–5 (2016).
[Romming13] N. Romming, C. Hanneken, M. Menzel, J. E. Bickel, B. Wolter, K. von Bergmann, A. Kubetzka, R. Wiesendanger, Writing and Deleting Single Magnetic Skyrmions, Science 343, 636–639 (2013).
[Royo17] M. Royo, M. De Luca, R. Rurali, I. Zardo, A Review on III–V core–multishell Nanowires: Growth, Properties, and Applications, J. Phys. D: Appl. Phys. 50, 143001, 1–34 (2017).

S

[Saad96] Y. Saad, *Iterative Methods for Sparse Linear Systems*, Second Edition, Society for Industrial and Applied Mathematics (SIAM), Philadelphia, 2003, 547.
[Sabatino11] P. Sabatino, G. Carapella, G. Costabile, Magneto-transport Properties of Curved Mesoscopic Superconducting Strips, Supercond. Sci. Technol. 24, 125007, 1–8 (2011).
[Sanchez09] S. Sanchez, M. Pumera, Nanorobots: The Ultimate Wireless Self-Propelled Sensing and Actuating, Chem. Asian J. Chem. 4, 1402–1410 (2009).
[Sanchez11] S. Sanchezб, A. A. Solovev, S. M. Harazim, C. Deneke, Y. F. Mei, O. G. Schmidt, The Smallest Man-Made Jet Engine, Chem. Rec. 11, 367–370 (2011).
[Sarkis15] B. Sarkis, D. Folio, A. Ferreira, Catalytic Tubular Microjet Propulsion Model for Endovascular Navigation, 2015 IEEE International Conference on Robotics and Automation (ICRA), Seattle, Washington, 2015, 3537–3542.
[Sarkis18] B. Sarkis, D. Folio, A. Ferreira, Catalytic Tubular Microjet Navigating in Confined Microfluidic Channels: Modeling and Optimization, J. Microelectromech. Syst. 27, 333–343 (2018).
[Savinov12] V. Savinov, V. A. Fedotov, S. M. Anlage, P. A. J. de Groot, N. I. Zheludev, Modulating Sub-THz Radiation with Current in Superconducting Metamaterial, Phys. Rev. Lett. 109, 243904, 1–5 (2012).
[Schmid66] A. Schmid, A Time Dependent Ginzburg-Landau Equation and its Application to the Problem of Resistivity in the Mixed State, Phys. kondens. Materie 5, 302–317 (1966).
[Schmidt01a]. O. G. Schmidt, K. Eberl, Nanotechnology – Thin Solid Films Roll Up into Nanotubes, Nature 410, 168 (2001).
[Schmidt01b] O. G. Schmidt, N. Schmarje, C. Deneke, C. Müller, N.-Y. Jin-Phillipp, Three-Dimensional Nano-objects Evolving from a Two-Dimensional Layer Technology, Adv. Mater. 13, 756–759 (2001).
[Schoelkopf08] R. J. Schoelkopf, S. M. Girvin, Wiring up Quantum Systems, Nature 451, 664–669 (2008).
[Scholar20] https://scholar.google.com.

[Schuster94] M. Th. Schuster, V. Indenbom, H. Kuhn, E. H. Brandt, M. Konczykowski, Flux Penetration and Overcritical Currents in Flat Superconductors with Irradiation-Enhanced Edge Pinning: Theory and Experiment, Phys. Rev. Lett. 73, 1424–1427 (1994).

[Shulaker17] M. M. Shulaker, G. Hills, R. S. Park, R. T. Howe, K. Saraswat, H.-S. P. Wong, S. Mitra, Three-Dimensional Integration of Nanotechnologies for Computing and Data Storage on a Single Chip, Nature 547, 74–78 (2017).

[Sengupta12] S. Sengupta, M. E. Ibele, A. Sen, Fantastic Voyage: Designing Self-Powered Nanorobots, Angew. Chem. Int. Ed. 51, 8434–8445 (2012).

[Silhanek10] A. V. Silhanek, J. Van de Vondel, V. V. Moshchalkov, Guided Vortex Motion and Vortex Ratchets in Nanostructured Superconductors, In: V. Moshchalkov, R. Wördenweber, W. Lang (Eds.), *Nanoscience and Engineering in Superconductivity*, Springer, Berlin–Heidelberg, 2010, 1–24.

[Smirnova20] E. I. Smirnova, R. O. Rezaev, V. M. Fomin, Simulation of Dynamics of the Order Parameter in Superconducting Nanostructured Materials: Effect of the Magnetic Field Renormalization, Low Temp. Phys. 46, 325–330 (2020).

[Smith11] E. J. Smith, D. Makarov, S. Sanchez, V. M. Fomin, O. G. Schmidt, Magnetic Micro-Helix Coil Structures, Phys. Rev. Lett. 107, 097204, 1–4 (2011).

[Sochnikov10] I. Sochnikov, A. Shaulov, Y. Yeshurun, G. Logvenov, I. Božović, Large Oscillations of the Magnetoresistance in Nanopatterned High-Temperature Superconducting Films, Nat. Nanotechnol. 5, 516–519 (2010).

[Soler13] L. Soler, V. Magdanz, V. M. Fomin, S. Sanchez, O. G. Schmidt, Self-Propelled Micromotors for Cleaning Polluted Water, ACS Nano 7, 9611–9620 (2013).

[Solovev09] A. A. Solovev, Y. F. Mei, E. B. Ureña, G. Huang, O. G. Schmidt, Catalytic Microtubular Jet Engines Self-Propelled by Accumulated Gas Bubbles, Small 5, 1688–1692 (2009).

[Solovev12] A. A. Solovev, W. Xi, D. H. Gracias, S. M. Harazim, C. Deneke, S. Sanchez, O. G. Schmidt, Self-propelled Nanotools, ACS Nano 6, 1751–1756 (2012).

[Stenvall13] A. Stenvall, M. Siahrang, F. Grilli, F. Sirois, Computation of Self-Field Hysteresis Losses in Conductors with Helicoidal Structure using a 2D Finite Element Method, Supercond. Sci. Technol. 26, 045011, 1–10 (2013).

[Streubel16] R. Streubel, P. Fischer, F. Kronast, V. P. Kravchuk, D. D. Sheka, Y. Gaididei, O. G. Schmidt, D. Makarov, Magnetism in Curved Geometries, J. Phys. D: Appl. Phys. 49, 363001, 1–45 (2016).

[Sudo06] S. Sudo, S. Segawa, T. Honda, Magnetic Swimming Mechanism in a Viscous Liquid, J. of Int. Mater. Sys. and Struct. 17, 729–736 (2006).

[Süsstrunk15] R. Süsstrunk, S. D. Huber, Observation of Phononic Helical Edge States in a Mechanical Topological Insulator, Science 349, 47–50 (2015).

T

[Tabor89] M. Tabor, *Chaos and Integrability in Nonlinear Dynamics: An Introduction*, Wiley, New York, 1989, 384.

[Tempere09] J. Tempere, V. N. Gladilin, I. F. Silvera, J. T. Devreese, V. V. Moshchalkov, Coexistence of the Meissner and Vortex States on a Nanoscale Superconducting Spherical Shell, Phys. Rev. B 79, 134516, 1–5 (2009).

[Thouless82] D. J. Thouless, M. Kohmoto, M. P. Nightingale, M. den Nijs, Quantized Hall Conductance in a Two-Dimensional Periodic Potential, Phys. Rev. Lett. 49, 405–408 (1982).

[Thurmer08] D. J. Thurmer, C. Deneke, O. G. Schmidt, In Situ Monitoring of the Complex Rolling Behaviour of InGaAs/GaAs/Nb Hybrid Microtubes, J. Phys. D: Appl. Phys. 41, 205419, 1–5 (2008).

[Thurmer10] D. J. Thurmer, C. C. Bof Bufon, C. Deneke, O. G. Schmidt, Nanomembrane-based Mesoscopic Superconducting Hybrid Junctions, Nano Lett. 10, 3704–3709 (2010).
[Tierno07] P. Tierno, T. H. Johansen, T. M. Fischer, Localized and Delocalized Motion of Colloidal Particles on a Magnetic Bubble Lattice, Phys. Rev. Lett. 99, 038303, 1–4 (2007).
[Tierno08] P. Tierno, R. Golestanian, I. Pagonabarraga, F. Sagues, Controlled Swimming in Confined Fluids of Magnetically Actuated Colloidal Rotors, Phys. Rev. Lett. 101, 218304, 1–4 (2008).
[Tierno10] P. Tierno, O. Guell, F. Sagues, R. Golestanian, I. Pagonabarraga, Controlled Propulsion in Viscous Fluids of Magnetically Actuated Colloidal Doublets, Phys. Rev. E 81, 011402, 1–9 (2010).
[Tinkham63] M. Tinkham, Effect of Fluxoid Quantization on Transitions of Superconducting Films, Phys. Rev. 129, 2413–2422 (1963).
[Tinkham96] M. Tinkham, *Introduction to Superconductivity*, McGraw-Hill, New York, 1996, 454.
[Tirado84] M. M. Tirado, C. L. Martínez, J. G. de la Torre, Comparison of Theories for the Translational and Rotational Diffusion Coefficients of rod-like Molecules. Application to Short DNA Fragments, J. Chem. Phys. 81, 2047–2052 (1984).

U

[Uchida06] M. Uchida, Y. Onose, Y. Matsui, Y. Tokura, Real-Space Observation of Helical Spin Order, Science 311, 359–361 (2006).

V

[VanAken07] B. B. Van Aken, J. P. Rivera, H. Schmid, M. Fiebig, Observation of Ferrotoroidic Domains, Nature 449, 702–705 (2007).
[Vlcek93] B. M. Vlcek, H. K. Viswanathan, M. C. Frischherz, S. Fleshler, K. Vandervoort, J. Downey, U. Welp, M. A. Kirk, G. W. Crabtree, Role of Point Defects and their Clusters for Flux Pinning as Determined from Irradiation and Annealing Experiments in $YBa_2Cu_3O_{7-\delta}$ single crystals, Phys. Rev. B 48, 4067–4073 (1993).
[Volkov19] O. M. Volkov, A. Kákay, F. Kronast, I. Mönch, M.-A. Mawass, J. Fassbender, D. Makarov, Experimental Observation of Exchange-Driven Chiral Effects in Curvilinear Magnetism, Phys. Rev. Lett. 123, 077201, 1–6 (2019).
[Volz99] S. G. Volz, G. Chen, Molecular Dynamics Simulation of Thermal Conductivity of Silicon Nanowires, Appl. Phys. Lett. 75, 2056–2058 (1999).

W

[Wang09] J. Wang, Can Man-Made Nanomachines Compete with Nature Biomotors? ACS Nano 3, 4–9 (2009).
[Wang12] J. Wang, W. Gao, Nano/Microscale Motors: Biomedical Opportunities and Challenges, ACS Nano 6, 5745–5751 (2012).
[Wang18] J. Wang, Y. Yin, Q. Hao, Y. Zhang, L. Ma, O. G. Schmidt, Strong Coupling in a Photonic Molecule Formed by Trapping a Microsphere in a Microtube Cavity, Adv. Opt. Mater. 6, 1700842, 1–8 (2018).
[Wang19] J. Wang, D. Karnaushenko, M. Medina-Sanchez, Y. Yin, L. Ma, O. G. Schmidt, Three-Dimensional Microtubular Devices for Lab-on-a-Chip Sensing Applications, ACS Sens. 4, 1476–1496 (2019).

[Wang20] J. Wang, M. Medina Sanchez, Y. Yin, R. Herzer, L. Ma, O. G. Schmidt, Silicon-Based Integrated Label-Free Optofluidic Biosensors: Latest Advances and Roadmap, Adv. Mater. Technol. 1901138, 1–24 (2020).
[Wrede20] P. Wrede, M. Medina-Sánchez, V. M. Fomin, O. G. Schmidt, Switching Propulsion Mechanisms of Catalytic Micromotors (in preparation) (2020).

X

[Xu14] Y. Xu, I. Miotkowski, C. Liu, J. Tian, H. Nam, N. Alidoust, J. Hu, C.-K. Shih, M. Z. Hasan, Y. P. Chen, Observation of Topological Surface State Quantum Hall Effect in an Intrinsic Three-Dimensional Topological Insulator, Nat. Phys. 10, 956–963 (2014).
[Xu15] S.-Y. Xu, I. Belopolski, N. Alidoust, M. Neupane, G. Bian, C. Zhang, R. Sankar, G. Chang, Z. Yuan, -C.-C. Lee, S.-M. Huang, H. Zheng, J. Ma, D. S. Sanchez, B. K. Wang, A. Bansil, F. Chou, P. P. Shibayev, H. Lin, S. Jia, M. Z. Hasan, Discovery of a Weyl Fermion Semimetal and Topological Fermi Arcs, Science 349, 613–617 (2015).

Y

[Yin17] Y. Yin, S. Li, V. Engemaier, E. S. G. Naz, S. Giudicatti, L. Ma, O. G. Schmidt, Topology Induced Anomalous Plasmon Modes in Metallic Möbius Nanorings, Laser Photonics Rev. 1600219, 1–5 (2017).
[Yin19a] Y. Yin, J. Wang, X. Wang, S. Li, M. R. Jorgensen, J. Ren, S. Meng, L. Ma, O. G. Schmidt, Water Nanostructure Formation on Oxide Probed in Situ by Optical Resonances, Sci. Adv. 5, eaax6973, 1–6 (2019).
[Yin19b] Y. Yin, J. Pang, J. Wang, X. Lu, Q. Hao, E. S. Ghareh Naz, X. Zhou, L. Ma, O. G. Schmidt, Graphene-Activated Optoplasmonic Nanomembrane Cavities for Photodegradation Detection, ACS Appl. Mater. Int. 11, 15891–15897 (2019).
[Yu10] X. Z. Yu, Y. Onose, N. Kanazawa, J. H. Park, J. H. Han, Y. Matsui, N. Nagaosa, Y. Tokura, Real-space Observation of a Two-Dimensional Skyrmion Crystal, Nature 465, 901–904 (2010).

Z

[Zeldov94] E. Zeldov, A. I. Larkin, V. B. Geshkenbein, M. Konczykowski, D. Majer, B. Khaykovich, V. M. Vinokur, H. Shtrikman, Geometrical Barriers in High-Temperature Superconductors, Phys. Rev. Lett. 73, 1428–1431 (1994).
[Zeng93] L. Z. Zeng, J. F. Klausner, R. Mei, A Unified Model for the Prediction of Bubble Detachment Diameters in Boiling Systems. I. Pool. Int. J. Heat Mass Transfer 36, 2261–2270 (1993).
[Zhang03] L. Zhang, H.-J. Xie, Fröhlich Electron-Interface and -Surface Optical Phonon Interaction Hamiltonian in Multilayer Coaxial Cylindrical $Al_xGa_{1-x}As$/GaAs Quantum Cables, J. Phys. Condens. Matter 15, 5871–5879 (2003).
[Zhang05] L. Zhang, E. Deckhardt, A. Weber, C. Schönenberger, D. Grützmacher, Controllable Fabrication of SiGe/Si and SiGe/Si/Cr Helical Nanobelts, Nanotechnology 16, 655–663 (2005).
[Zhang08] L. Zhang, J. J. Abbott, L. Dong, K. E. Peyer, B. E. Kratochvil, H. Zhang, C. Bergeles, B. J. Nelson, Characterizing the Swimming Properties of Artificial Bacterial Flagella, Nano Lett. 9, 3663–3662 (2009).
[Zhang09] L. Zhang, J. J. Abbott, L. Dong, B. E. Kratochvil, D. Bell, B. J. Nelson, Artificial Bacterial Flagella: Fabrication and Magnetic Control, Appl. Phys. Lett. 94, 064107, 1–3 (2009).

[Zhang13] W. Zhang, W. Miao, S. L. Li, K. M. Zhou, S. C. Shi, J. R. Gao, G. N. Goltsman, Measurement of the Spectral Response of Spiral-Antenna Coupled Superconducting Hot Electron Bolometers, IEEE Trans. Appl. Supercond. 23, 2300804, 1–4 (2013).

[Zhang14] L. Zhang, X. Wang, Atomistic Insights into the Nanohelix of Hydrogenated Graphene: Formation, Characterization and Application, Phys. Chem. 16, 2981–2988 (2014).

[Zhao03] H. Zhao, V. M. Fomin, J. T. Devreese, V. V. Moshchalkov, A New Vortex State with Non-Uniform Vorticity in Superconducting Mesoscopic Rings, Solid State Commun. 125, 59–63 (2003).

[Zhuravel12] A. P. Zhuravel, C. Kurter, A. V. Ustinov, S. M. Anlage, Unconventional rf Photoresponse from a Superconducting Spiral Resonator, Phys. Rev. B 85, 134535, 1–8 (2012).

Index

https://doi.org/10.1515/9783110575576-009